Monitoring Locally Induced Hyperthermia
with Magnetic Resonance Imaging

Mika Wynand Vogel

Monitoring Locally Induced Hyperthermia with Magnetic Resonance Imaging

Monitoring van lokaal geïnduceerde hyperthermie met behulp van magnetische kernspintomografie

PROEFSCHRIFT

ter verkrijging van de graad van doctor
aan de Erasmus Universiteit Rotterdam
op gezag van de Rector Magnificus

Prof.dr. S.W.J. Lamberts

volgens besluit van het College voor Promoties.

De openbare verdediging zal plaatsvinden op
woensdag 12 januari 2005 om 15:45 uur

door

Mika Wynand Vogel
geboren te Amsterdam

PROMOTIECOMMISSIE

Promotor:	Prof.dr. P.M.T. Pattynama
Overige leden:	Prof.dr. A.M. Vossepoel
	Prof.dr. G.P. Krestin
	Prof.dr. K. Nicolay

Voor Welmoed Silvis,
Wynand Vogel
en Kaarina Stén.

Contents

Contents

Magnetic Resonance Thermometry: a review

Chapter 1

ABSTRACT

Magnetic resonance thermometry is a relatively new and unique technology for non-invasive monitoring of (local) therapeutic temperature changes that is not yet in common use. Temperature measurements using magnetic resonance heat thermometry can be performed in several ways. Four common methods are described. Spin-lattice (T_1) relaxation thermometry seems robust and viable, but relatively inaccurate. Diffusion thermometry is slightly more accurate at the cost of increased scan time. Chemical shift thermometry is most accurate but inherently slow and therefore impracticable. Its derivative, phase shift thermometry seems most promising for monitoring mild temperature changes. Phase shift imaging is, however, difficult to implement due to motion artifacts and susceptibility effects. Apparently two fields for use of MR thermometry in practical therapeutic applications emerge: high temperature gradients for thermoablation that need not be quantified exactly, and low temperature gradients for heat related biological effects that must be controlled precisely.

Mika W. Vogel, MSc ♦
Peter M.T. Pattynama, PhD, MD ♦

From
♦ Department of Radiology, Erasmus MC, University Medical Center Rotterdam, The Netherlands.

Keywords
Thermometry
Temperature mapping
Magnetic resonance
Noninvasive
Review

INTRODUCTION

New treatment options become available with controlled locally induced hyperthermia for a variety of diseases. A large temperature rise can instantaneously inactivate cancerous tissue, as has been reported for some tumors in the brain,[1] head and neck,[2-5] breast, and liver metastases.[6-9] With small temperature elevations, it has been shown feasible to start and stop localized gene expression, when gene constructs with thermosensitive promoters are distributed as gene therapy,[10] induce local drug release (for a review see 11), or sensitize tissue to radio-[12] or chemo-therapy.

Monitoring of the actual induced temperature elevation is a key issue for proper application of thermal therapy. Invasive thermometers into the target region are of limited value, because the temperature distribution *in-vivo* can be very inhomogeneous.[13] To improve the spatial resolution of the temperature measurements, without extensive and possibly erroneous modeling of the target tissue, imaging of the heating process has been proposed.[14] Magnetic Resonance Imaging (MRI) has been favored over other imaging modalities, because it offers excellent intrinsic soft tissue contrast and several independent parameters to visualize temperature changes in biological tissues.

Consequently, different MR imaging strategies have been proposed in literature, to maximize the effect of temperature dependent change in these parameters on the acquired MR images. For optimal monitoring of temperature changes, one must take into account the merits and drawbacks of the several possible imaging strategies. Ideally, the MR temperature measurements should be accurate, precise and reproducible for all clinical targets. For treatment guidance, MR temperature maps should be available on-line.

In this review we will discuss the design of the different MR thermometry methods and focus on the underlying MR mechanisms. Also the feasibility, clinical applications and the areas for potential improvement of the various methods will be discussed. In preparation of this review we searched the MEDLINE (1966 through 2004), EMBASE (1988-1999), SCI-EXPANDED (1988-2004) and SSCI (1988-2004) electronic databases for English- and German-language peer reviewed papers. The index terms : *thermography, thermometry, temperature or heat* were combined with *mapping or measurement* and filtered with the term magnetic resonance. Relevant articles from the reference lists of the thus found articles were also included in the review as were recent abstracts on the subject from major scientific meetings.

Requirements for MR thermometry

Ideally MR thermometry yields very accurate absolute temperature measurements, with sub-second acquisition times and sub-millimeter spatial resolution over a large volume. Such demands require an exceptionally high signal to noise ratio (SNR), which is not available in current clinical MR imagers. Compromises to

spatial and temporal resolution are therefore inevitable. The spatial and temporal resolutions determine the minimal accuracy of the temperature measurements. In order to not become the dominant source of error, the temperature gradient in combined spatial and temporal resolutions should be within the confidence interval of the thermal accuracy.

The estimated temperature over time is the primary parameter to predict induced cell death, the goal of monitoring local thermal ablation. For this purpose, the concept of a thermal dose has been introduced.[15] The thermal dose relates to a critical heat exposure over time of the target tissue. For an accurate thermal dose calculation it is necessary to have short image acquisition times. This ensures that induced thermal changes are lower than the temperature measurement accuracy in the tissue. Care must be taken when using the thermal dose calculation as proposed by Sapareto and Dewey,[15] because errors in the temperature measurement lead to overestimation of the treatment effect. This error is readily corrected when the standard deviation for the temperature measurements is known.[16]

Local thermal ablation aims for destruction of the target tissue with a relatively small margin between "dead" and viable tissue. Therefore it is proposed that high temperature ablation benefits more from higher spatial and temporal resolution than from increased thermal accuracy. This is especially true when using focal techniques such as focused ultrasound. In contrast low temperature changes that are sustained for long periods of time, for example adjuvant hyperthermic treatment, benefit more from increased thermal accuracy.[17]

Effect of heat on the MR signal
Temperature dependence of the MR signal is primarily based on its effect on pure water. It is well known that water viscosity η and density change with temperature. The viscosity of water at 37°C is $0.695 \cdot 10^{-3}$ Ns/m^2, and decreases with increasing temperature.[18] Changes in density and viscosity are due to changes in the crystalline structure of water, and relates to the strength of the hydrogen bonds between water molecules.
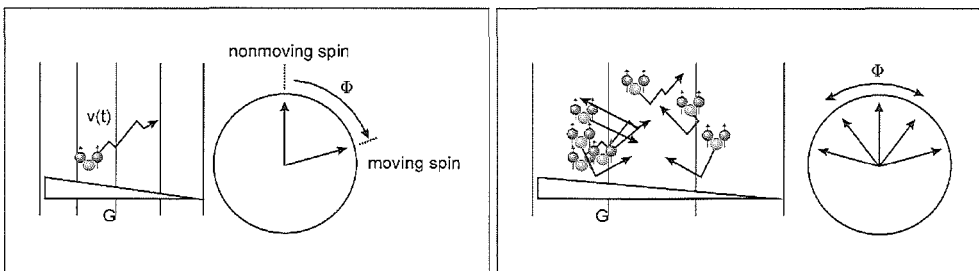
Figure 1. Movement of the ^1H nuclei of free water causes them to wander over the applied gradients, causing, at the time of the echo, incomplete refocusing and signal loss. As temperature increases, more signal is lost. The effect is magnified by application of the diffusion gradients.

Due to reduced viscosity at higher temperature (T), the water diffusion constant (D) increases (see also Figure 1):

$$D = \frac{kT}{6\pi\eta R_H}$$ [1]

where k is Boltzmann's constant and R_H is the hydrodynamic radius. At the same time, spin-lattice relaxation (T_1) is affected through viscosity changes. When the product $\varpi^2 t_c^2$ is much smaller than 1 (the resonance frequency ϖ is in the range of 8.5 to 127.7 MHz for typical clinical scanners, and spin correlation times τ_c for free water is near $5 \cdot 10^{-11}$ s at body temperature, Figure 2), T_1 relaxation is proportional to :

$$T_1 \propto \tau_c^{-1} \propto \frac{\eta}{T}$$ [2]
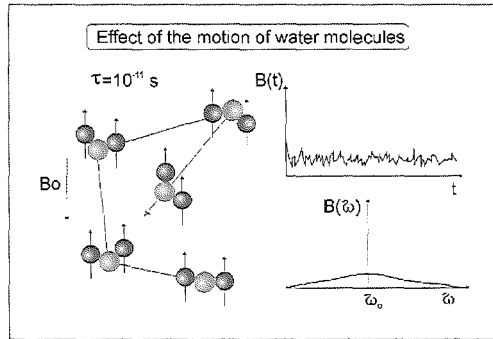
Figure 2. Movements of the ^{1}H nuclei of free water with a certain correlation time (τ) yield small perturbations of the magnetic field. Only those spins that precess at ω_0 can loose their energy by stimulated emission. The spread of frequencies gets larger at higher temperature, thereby prolonging T_1

Increase of water temperature causes stretching of the hydrogen bonds between water molecules (see Figure 3). The temperature-dependent change in hydrogen bonds in free water leads to a change in the electron screening (σ) of the proton spin in the hydrogen atom.[19,20] The local opposing magnetic field due to the moving electrons increases with temperature, so that water becomes more diamagnetic. This effect is seen as a chemical shift or proton resonance frequency (PRF) shift.
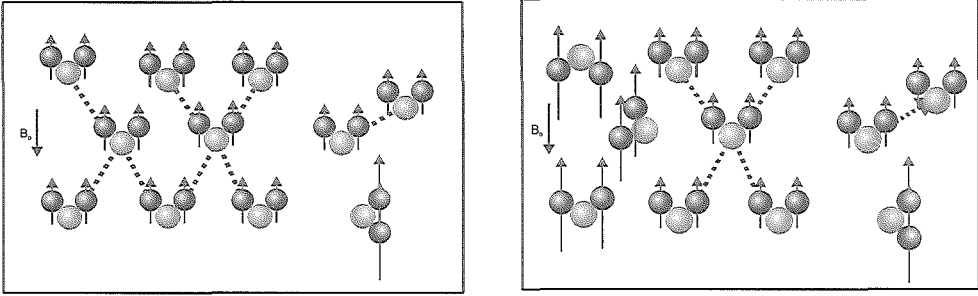
Figure 3. Water has an 'ice-like' structure, that is formed by H-bonding. Through this mechanism an polarized field is formed that opposes the main magnetic field (left). At higher temperature H-bonds are bent and broken. Thereby the nett opposing magnetic field at the water proton grows (right), causing the local precession frequency, through the Larmor equation, to decrease. This change in field is detectable as the proton resonance frequency shift.

The equilibrium magnetization (M_0) is proportional to the resultant spins from the individual spin states (n_1 and n_2), and is temperature dependent :

$$M_0 \propto \frac{|n_1 - n_2|}{n_2} = e^{-\frac{\Delta E}{kT}}$$ [3]

In addition other intrinsic parameters have been investigated[21] but have not been found to have general applicability to temperature measurements.

Next, we will discuss in more detail the commonly used MR thermometry methods: the T_1- and diffusion-weighted techniques and thermometry based on the chemical shift. It was noted that proton density, M_0, and T_2 of tissue also change with temperature. Proton density has attracted little attention, possibly through its limited sensitivity. The relation between temperature and T_2 is supposedly linear, although other factors may mask this relationship[22,23] and reports on *in-vivo* temperature effects are inconsistent.[24] In practice T_2-measurements are seldomly used for MR-thermometry, although it offers visualization of heat-induced edema. T_2^* weighted imaging has been reported useful for measuring temperature during cryosurgery,[25] but this technique is considered beyond the scope of this paper, and will not be discussed further.

MR Thermometry based on T_1-measurements
Heating of biological tissue results in a rise of its T_1 value, with a magnitude of approximately 5-12 ms/°C.[26-28] In a T_1-weighted image, a temperature rise thus corresponds with a lower signal intensity (SI). In sequential T_1-weighted MR images the relative temperature changes can be calculated from the measured changes in SI to that voxel's baseline SI. Different tissues have different T_1 values

Table 1. Typical tissue parameters

Tissue		T_1 (ms)	Diffusion (10^{-3} mm^2/sec)
Muscle (skeletal)		600✦, 732✧	1.42✳
Kidney		589✧	1.38✛
Brain	-Grey matter	813✧	0.66✳
	-White matter	683✧	0.43✳
Pancreas		455✧	0.76✛
Liver		270✦, 423✧	0.72✛
Spleen		480✦, 683✧	0.80✛

Data taken from ✦ Freimarck,[157] ✧Nitz,[158] ✳ Morvan et al,[65] ✛ Yamada et al,[159] ✳ Turner.[160] Temperature in-vivo. T_1 values at 1.0 Tesla.

(at body temperature, see Table 1). The relative change in T_1 values varies for different tissues.[28] Short TR fast spin echo sequences outperform simple fast spoiled gradient echo sequences.[24] Although any T_1-weighted sequence can be used for MR thermometry, inversion recovery spoiled gradient-echo sequences are generally preferred because of their high temporal resolution (3-6 seconds) and increased sensitivity to temperature changes.[29] The voxel size is typically less than 0.1 cm^3. It is anticipated that T_1-based thermography has slightly better sensitivity

Table 2. T_1 temperature accuracies

Author	Scantime (s)	Technique	B_0 (T)	Accuracy (°C)	Range (°C)	FOV (mm)	Voxelsize (mm^3)	TE/TR/θ	Tissue (N)
Wlodarczyk[32]	15	SPGR	1.5	1.7	35-45	500	64	6/230/75°	Phantom(1)
Wlodarczyk[31]	240	TOMROP	1.5	0.93	N/A	N/A	N/A	NA/1200/17°	Phantom(1)
Schwarzbauer[43]	2	Snapshot FLASH	4.7	0.7	7-45	51*	6,4	1.1/2.1/5° 16-point	Phantom(1)
Bohris[33]	3	Snapshot FLASH	1.5	0.6	22-45	200-300	608*,1369*	4/10.2/12°	Muscle(4), Gland(2), Fat(3)
Kahn[162]	5	Snapshot FLASH	1.5	3*	25-62	230	16	3/6/5° 6-point	Muscle(5), Brain(5), Liver(5)
Mietzsch[137]	311	Spin-Echo	1.5	0.5	14-31	150-180	348*, 490*	10/1200/90	Muscle(2)
Steiner[29]	2,5	Gradient	0.5	N/A	22-75	180	980*	10/20/50°	Liver(1)
Vogl[5]	6	Snapshot FLASH	1.5	2-3*	36-50	350	60*	3/7/50°	Liver(10)
Binzoni[35]	50	Spin-Echo	1.5	0.5	34-37	N/A	17	10/500/90°	Leg(6)
Bertsch[164]	120	Snapshot FLASH	1.5	2,0	20-50	154	14.4	4.2/11/15° 9-point	Muscle (1)

*Estimation based on data presented in the mentioned article

at higher field strengths.[28] Increased SNR of the measurements is expected due to increased equilibrium magnetization, which is offset by extended T_1-values of tissue.

Various investigators have shown moderate accuracy for T_1 calibrations (Table 2). In the temperature range up to 40°C, T_1 is assumed to vary linearly with temperature.[30] The experimentally determined relation between T_1 and temperature is approximately linear,[27,31-35] although non-linear effects of T_1 in the higher temperature range have been described.[14,23,30] Ex-vivo storage,[36] or viscosity changes[14,22] have been demonstrated to cause deviations.
In ex-vivo biological tissues, the T_1 increase with temperature varied from approximately 1.0-1.8 %/°C[30] in the in-vivo measurements this was approximately 1.3 %/°C.[27] Higher values were found when the T_1-enhancing contrast agent Gd-DTPA was administered in-situ.[5] Typically the T_1 values show hysteresis, and therefore exclude multiple treatments.

Real-time temperature mapping of T_1-based MR thermometry has been shown possible[37,38] but relatively inaccurate, mainly due to calibration issues and hysteresis. Accuracies of up to 2.0°C have been reported in-vivo.[5] It seems that especially small temperature changes (as with mild hyperthermia) are difficult to monitor.[31,39] As an alternative to temperature mapping, one specific temperature may be monitored, by preselecting a cut-off value for T_1 with a corresponding inversion time.[40,41] This method allows one to follow a selected isotherm as an expanding zero intensity (dark) rim in real-time in the inversion recovery MR image.[42] Alternatively, acquisition of multiple images after a single inversion pulse,[43] offers both desired image contrast and allows T_1 quantification. Such an approach is however limited in spatial resolution.

Validation studies have shown good correlations between the lesion size as seen on MR images of T_1-weighted thermometry and the actual ex-vivo lesion size after thermoablation.[41,44-46] Lesion size deferred from signal intensity changes during ablation tend to overestimate the lesion size.[47]

T_1-weighted thermometry has been used to monitor laser induced thermotherapy for brain tumours,[1] head and neck tumours,[2-5] liver metastases,[6-9] and laser disc decompression.[48-50] Preliminary clinical results are also reported on prostatic[51] and uterine[52] tissue, kidney,[53-55] uterine fibroids[56] and vascular lesions.[57]

Diffusion-based MR Thermometry
Heating of biological tissue results in increased diffusion of free water (see *Effect of heat on the MR signal*) with signal (SI) attenuation in the resultant MR image. The SI loss is approximately linear with increasing temperature, of approximately 2.1 to 2.5%/°C.[17,31,32,58,59] Temperature values with diffusion-based MR thermometry are calculated from the diffusion coefficient (D, see equation >4), which is approximated by measuring signal intensities in the MR image. The value of D differs between tissues[60] (Table 1). Quantification of D requires a relatively long T_2 in the tissue under consideration and the method is therefore less suited for

tissues with a short T_2.[24] An additional problem in the high temperature range (greater than 60°C) is that tissue damage will also alter diffusion, resulting in less accurate temperature maps. Theoretically, diffusion based thermometry offers the additional possibility of calculating microcirculatory perfusion, but in practice, this has been fraught with difficulties.[61]

Table 3. Diffusion temperature accuracies

Author	Scantime (s)	Technique	B0 (T)	Accuracy (°C)	Range (°C)	FOV (mm)	Voxelsize (mm^3)	TE/TR/B_0/B_1	Tissue (N)
Le Bihan[17]	205	N/A	1	0.5	35-44	256	40	N/A	Phantom(1)
Wlodarczyk[32]	15	PGSE	1.5	1.7	35-45	500	64	40/230/0/343	Phantom(1)
Wlodarczyk[31]	240	Spin-Echo	1.5	0.9	N/A	N/A	N/A	94/120/?/?	Phantom(1)
Delannoy[69]	420	Gradient*	1	1	20-33*	256	80	N/A	Phantom(1)
Delannoy[165]	90*	Gradient	1.5	0.2	15-32*	128x256	20	N/A	Phantom(1)
Samulski[70]	255	DW-SE	1.5	0.5	20-45	240	16	140/900/0.15/654.2	Phantom(1)
Bleier[166]	2	DW-EPI	1.5	N/A	N/A	384	27	N/A	Brain(2*)
Macfall[62]	10	DW-EPI	1.5	0,,9	32-40	200	68	60/2000/23.0/777.1	Brain(1)
Il'yasov[58]	60	SS-FSE	2.0	2	20-60*	256	32	?/3000/6/750	Muscle(1)
Morvan[59]	6.4*	DW-STE	0.5	1.9	36-42*	250	1100	48/800/100/560	Muscle(1)
Morvan[65]	51	DW-STE	0.5	2	14-40	250	1.95x1.95	48/1000*/0/560	Muscle(5)

* Estimation based on data presented in the mentioned article

Diffusion based thermometry is a relatively slow method due to low SNR, that is improved at the cost of temporal or spatial resolution. The MR sequences used to employ pulsed gradient spin echo sequences with acquisition times in the order of minutes (see Table 3). Single shot methods vastly reduce acquisition time and increase temperature accuracy.[58,62] Voxel size is usually less than 0.5 cm^3.

Diffusion imaging is virtually insensitive to artifacts related to RF inhomogeneities[63] and, theoretically, directly reflects absolute temperature.[64] In practice, however, only relative diffusion changes are used to measure relative temperature changes.[32,65] Ideally, estimations of D are made by combining multiple repetitive acquisitions with different diffusion-sensitizations, but in practice estimations of D are usually based on a two point fit using two acquisitions only. The latter approach yields satisfactory results, provided that diffusion effects dominate the signal.[66] True diffusion, the trace of the diffusion tensor, is typically not determined. Alternatively, for thermometry, a derivative, the apparent diffusion coefficient D* is used as an approximation. The apparent diffusion coefficient is calculated from signal intensity in the image (S) and gradient parameters (b): [61,67,68]

$$D \cong D^* = \frac{\log\left(\frac{S_1}{S_0}\right)}{b_0 - b_1} \qquad [4]$$

Temperature changes (ΔT) are then calculated from the diffusion coefficient D, as approximated by D^* according to:[17]

$$\Delta T = \frac{c T_0^2 \Delta D}{D_0} \qquad [5]$$

where D_0 is the diffusion coefficient at the baseline temperature T_0 and c is a tissue specific constant.

Validation
The temperature accuracy of diffusion-based MR thermometry is slightly better than that of T_1-weighted thermometry, but the used methods were much slower. The uncertainties for temperature measurements of diffusion-based thermometry are less than 1°C in phantoms,[17,31,69,70] and approximately 2.0°C[58,59] in muscle tissue. To our knowledge, it has not yet been proved possible to obtain real-time temperature maps using this technique.

Diffusion-weighted imaging requires fast scanning sequences, necessary for high temporal resolution, and avoidance of ghosting artifacts that render a diffusion-weighted image useless. When diffusion gradients are added to the normal imaging gradients setup, gradient cross-terms may occur, resulting in erroneous temperature calculation.[67] Correction algorithms have been proposed for image distortion due to eddy currents[71] and rigid body motion.[72]

Lesion determination
Diffusion weighted MR imaging of thermally inflicted damage shows irreversible increased self diffusion in sarcoma,[73] brain, kidney and muscle tissue[74] after hyperthermia treatment.

Classical Chemical Shift
The chemical shift of a nucleus denotes the difference between the resonance frequency of that nucleus relative to a standard, expressed in parts per million (ppm, 10^{-6}):[75]

$$\delta = \frac{\omega_L - \omega_{ref}}{\omega_{ref}} 10^{-6} \qquad [6]$$

where ω_L and ω_{ref} are the frequencies of the nucleus (generally ^{1}H of water) and the standard (fat or metabolites for example) respectively. Usually, the water-fat

chemical shift is considered, which is approximately 3.35 ppm at body temperature.[76] Heating of biological tissue results in a smaller chemical shift, which may serve as a direct measure of absolute temperature T, according to:

$$T = \frac{\delta_t - \delta_{ref}}{\alpha} \quad\quad [7]$$

where α is the temperature sensitivity (ppm / °C), δ_t is the temperature related chemical shift and Δ_{ref} is the reference chemical shift distance at a predetermined temperature. The accuracy of chemical-shift thermometry markedly improves with higher magnet field strength because the chemical shift increases linearly with field strength, as does SNR.

Of the various MR methods, chemical-shift thermometry seems the most accurate one (see Table 4). Its sensitivity is approximately -.0108 ppm/°C(see also Table 5).[19] When using the chemical shifts of naturally present spectra such as fat[77,78] or metabolites,[79-81] the error in temperature measurements is less than 1°C. Even better accuracy can be achieved by using the spectral peaks of intravenously administered custom-made molecules, e.g. lanthanide-complexes.[82-85] The *in-vitro* accuracy of the molecular probes has been reported to be on in the order of 0.02°C,[82] and the *in-vivo* accuracy as approximately 0.9°C. The molecular probes also allow best temporal resolution of chemical shift thermometry. Uncertainty exists, however, with regard to pharmacokinetic properties of the molecular probes, such as the acceptable dose and the possible inhomogeneous distribution *in-vivo*.

Drawbacks of chemical-shift thermometry include the typically low signal, and thus coarse resolution and/or long acquisition time. Line scan spectroscopic measurements using the chemical shift for absolute temperature estimation in the breast showed unacceptable thermal accuracy.[86]

Table 4. Chemical Shift temperature accuracies

Author	Scantime (s)	B_0 (T)	Accuracy (°C)	Range (°C)	FOV (mm)	Voxelsize (mm^3)	TR/BW/S	Tissue (N)
Wlodarczyk[31]	240	1.5	1	N/A	N/A	N/A	275/1000/256	Phantom(1)
Corbett[80]	N/A	4.7	1*	20-40	N/A	1000	1000*/5000/2048	Brain(8)
Corbett[81]	60-90	1.5	0.6	28-40	20	4000	2700/750/1024	Brain(3)
Kuroda[78]	64*	4.7	N/A	20-45	96	27	260/2000/16526	Muscle (1)
Kuroda[89]	45	1.5	1.6	37-47	20	N/A	350/767/128	Liver(1)
Young[167]	420	1.5	0.6	5-37	N/A	8000	1500/645*/1024	Muscle(1)
Mulkern[77]	42	1.5	1.6	37-60	N/A	5	1000/16/125*	Muscle(6)
Aime[168]	160-240*	1.5	1	25-35	N/A	N/A	N/A/N/A/N/A	Liver(8)
Zuo[83]	30	4.7	0.5	25-32	N/A	N/A	30/10000/1024	Abdomen(5)

*Estimation based on data presented in the mentioned article

Usually CSI sequences with long (greater than 60 seconds) acquisition times are required to sample a usable proton spectrum. The method, in addition, is rather sensitive to motion artifacts. Single-shot spectroscopic imaging is reported to greatly reduce scan time while preserving temperature accuracy.[87-89] The demands on the MR hardware are considerable, especially with regard to stability and homogeneity of the magnetic field. A more fundamental problem is that thermal damage to cells may cause a fall in metabolite level or structural decomposition of the natural or artificial molecular probes, which may complicate the measurements with chemical shift thermometry.

Phase shift

Heating of biological tissue results in decrease of the local magnetic field (via a temperature dependent increase of the screening constants as described in *Effect of heat on the MR signal*). Distribution of heat thus causes a change in the magnetic field distribution of the heated object. This causes local phases difference or phase shifts (angle rotation, $\Delta\varphi$), which can be used for calculating differences in temperature ΔT, according to:

$$\Delta T = \frac{\Delta\varphi}{\gamma\alpha B_0\tau}$$ [8]

where γ is the gyromagnetic ratio, and α is the temperature sensitivity (ppm / °C) that, like T_1, varies with the (susceptibility of the) tissue type (Table 6).

Table 5. Phase shift temperature accuracies

Author	Scantime (s)	Technique	B_0 (T)	Accuracy (°C)	Range (°C)	FOV (mm)	Voxelsize (mm³)	TE/TR/θ	Tissue (N)
De Zwart[96]	0.14	PRESTO	4.7	0.3	14,35	36	1.6*	18/12/13°	Phantom(1)
Wlodarczyk[32]	15	SPGR	1.5	0.34	35-45	50	640	45/230/75°	Phantom(1)
Chung[92]	3-5	ES-FLASH	0.2	1.0	37-90	128	44	9.5/19.4/30°	Liver(1)
Sinha[161]	13	SPGR	0.2	1.44	27-45	200	61	30/60/40°	Liver(1)
De Zwart[98]	0.5	ES-FLASH	4.7	0.4	35-42*	80	8.5	10/15/15°	Muscle(1)
Kuroda[91]	3.3	SPGR	1.5	4	32-84	160	2.3	12.8/26/15°	Muscle(16)
Macfall[118]	10	Gradient	1.5	0.6	32-43	160	16	20/34/NA	Brain(2), Muscle(2)
Moriarty[169]	10*	SPGR	1.5	1.9	37-53	80	0.5*	10.8/38.9/30°	Brain(7)
Stollberger[105]	12	Gradient	1.5	1.0	20-55	180-230	3.2-4.0	18/30/18°	Brain(10)
Carter[106]	16	Gradient	1.5	1.0	37-44	240	8.8	20/34/NA	Sarcoma(4)
Ishihara[94]	14*	Gradient	4.7	1.0	35-45*	77*	1*	13/115/NA	Body(1) Brain(1)
Bertsch[164]	17	Snapshot FLASH	1.5	1.6	23-44	154	4.8	50/67/35°	Muscle (1)
Kahn[162]	5	SPGR	1.5	1.8*	25-45	230	16*	16/40/40°	Brain(5), Muscle(5), Liver(5)

* Estimation based on data presented in the mentioned article

The variability of α in different tissues, though, is much less than the T_1.[90-92] The factor τ in the equation denotes a time difference: for gradient echo pulse sequences τ equals the echo time, for spin-echo and fast spin echo sequences[93] τ represents the timing asymmetry between the 90° and first 180° degree RF pulses and between 180° degree RF pulse and echo time (see also chapter 5).

Phase shift images are generally acquired using fast spoiled gradient echo sequences, to reduce motion artifacts related to respiratory motion. Gradient echo sequences that measures the free induction decay have good inherent sensitivity for phase shift imaging.[94,95] Some investigators have experimented with ultrashort scan times of less than 1 second.[93,96-101] Potential benefits of short acquisition times lie primarily in reduction of motion, increased volume coverage and a less steep intra-acquisition intra-voxel heat gradient. The voxel size is generally small (less than 0.05 cm³).

Table 6. Chemical shift temperature sensitivities

Tissue	In-vivo / ex-vivo	α (ppm/°C)	uncertainty (ppm/°C)
Skeletal muscle	In-vivo	-0.00876✧, -0.0114✗, -0.00825✛♥	0.00069, 0.0006, 0.0004♥
	Ex-vivo	-0.0109❖, -0.00772✓	0.0002, 0.0001
Liver	Ex-vivo	-0.0086✦, -0.007✳, -0.0093❖, -0.00739✓, -0.00879ᵴ	0.0003, 0.0002
Brain	In-vivo	-0.00739✛♥	0.0004♥
	Ex-vivo	-0.00951 ✳✦, -0.00855 ✳♠, -0.0098❖, -0.00724✓	0.0005, 0.0004, 0.0002
Sarcoma (leg)	In-vivo	-0.0120 ✳♠	0.0004♥
Kidney	Ex-vivo	-000917✓	0,0001

Data taken from ✧Kuroda,[91] ✓Kuroda,[75] ✦Chung,[92] ✳Sinha,[161] ✛MacFall,[118] and ✗Ishihara,[94] ✳Stollberger,[105] ✳Carter,[106] ❖Kahn,[162] and ᵴChung.[163]
♥ Estimation based on data presented in article.
✦Heat-source perpendicular to antenna
♠ Heat-source parallel to imaging plane

Validation

Temperature accuracy of the phase shift method is typically around 0.5°C in phantoms[32,94,96,102] and less than 2.0°C *in-vivo*.[90,94,103] The temperature accuracy and coefficient of determination for phase-shift calibrations are sufficient according to proposed monitoring parameters[104] (Table 6, Table 7). Online changes of *in-vivo* temperature can be shown with an accuracy of ±1°C.[105-107]

The time needed for build-up of the phase shift is inversely linear with the field strength (Equation 8), and techniques that permit a longer TE than the TR can be beneficial at lower field strengths.[92] Control of heating by means of feedback to the heat-delivery apparatus has been shown feasible.[97,108-110]

Table 7. Calibration measurements

Technique/ r^2	Phantom	*Ex-vivo* tissue	*In-vivo* tissue
T_1	0.743 ♦, 0.915 ♥, 0.98 ▼	0.92 ✂, 0.96 ▼	0.85-0.90 ◉
Diffusion	0.971♦, 0.981♥	N/A	0.986 ❖⁋
Chemical shift	0.999 ♦, 0.999 ☆	N/A	0.82 ✓, 0.86 ◎, 0.96 ▲
Phase shift	0.989 ♦, 0.995 ♥	0.96 ♠, 0.98 ▼	0,84 ✛

♥ Wlodarczyk et al,[31] ♦ Wlodarczyk et al,[32] ✂ Bohris et al,[33] ♠ MacFall et al,[118] ◎ Corbett,[81] ✓ Mulkern,[77] ▲ Corbett,[80] ▼ Kahn,[162] ☆ Zuo,[82] ❖ Hasegawa,[170] ● Mueller-Lisse,[41] ✛ Carter.[106]
⁋ No direct temperature measurement, indicative figure only.
It is noted that r^2 derived from two different (inexact) temperature measurements may be inappropriate, so in vivo results may be questioned.[171]

The main problem with this method is motion, which causes phase changes that are confused with temperature changes. It has been shown feasible to compensate motion along the readout gradient using a standard gradient moment nulling technique.[101] Effects due to dislocation are worse, because a total mismatch with the reference phase map occurs. Strategies to compensate problems with regard to dislocation are respiratory gating,[111,112] possibly in combination with appropriate baseline selection. Alternatively, the position of a laser catheter may be tracked using MR active tracking, to allow for appropriate baseline selection.[113] Also, it has been suggested that temperature changes may be estimated from the phase map itself.[114] Geometrical conformational changes (i.e. dislocation), if not corrected for, reduce accuracy of the temperature measurements.[115] Coagulation itself, surprisingly, does not seem to invalidate temperature measurements.[116,117]

Other problems of phase shift thermometry relate to mass volume susceptibility effects. These are naturally abundant[118] and related to heat

geometry,[119] temperature distributions within the tissue,[117,120,121] and presence of paramagnetic contrast agents.[102] The effect of such errors is typically on the order of 10%.[117,122] An even more significant confounding effect is due to the interaction of the temperature independent signal of fat with the temperature dependent phase shift within the same voxel.[122] It has been shown that fat-suppression improves the reproducibility of phase-shift thermometry in fatty tissue.[98]

Lesion determination
The 60-65°C isotherm is indicative of induced lesions (e.g. in the brain).[123] Small lesions could be mathematically distinguished using advanced image processing in *ex-vivo* kidney and liver (N=36) with a (high) spatial resolution of about 0.6 mm.[124] It is generally felt that lesion size can not be deferred from temperature maps alone, but must take into account the effective heat deposition over time as well.[125-127] Accurate prediction of ablation volumes after focused ultrasound treatment has been shown feasible.[128,129] Care must be taken that tissue swelling due to extended tissue heating does not invalidate PRF-based thermometry.[130]

Clinical use
Initial experience indicates that phase shift thermometry may be used to monitor ablation of prostate cancer.[131] Preliminary research has shown potential for monitoring temperature during thermoablative procedures in brain tumor,[123] liver[112] and kidney,[132] and tumor of the lower leg.[106] It is anticipated that gated PRF-thermometry in human liver is feasible when temperature estimates need not be better than 2.5 degrees Celsius standard deviation.[133]

CONCLUSION
T_1-weighted thermometry seems a viable technique,[5,49,51,134-136] but a relatively inaccurate one when compared with alternative techniques.[31,32,66,123,135] It has improved the control of laser therapy,[7] but seems inappropriate for measuring small temperature changes, typical for mild hyperthermia, due to the inherent problematic calibration.[34] There appears to be little room for improvement, although such claims are recently made.[33,53,137] T_1 is, however, a method that has potential to monitor temperature within fat tissue. Lesion size on T_1 thermometry images generally does not agree with actual lesion size and additional scanning remains necessary. Recently, the use of contrast agent-filled thermosensitive liposomes has attracted attention for monitoring a particular threshold temperature.[138,139] In parallel, development of state dependent contrast agents seems promising.[140]

Diffusion weighted thermometry is more accurate than T_1-weighted thermometry,[31,32,66] but has the major drawback that it is very sensitive to motion, thereby requiring very short scan times. It may find application for measurement of small temperature elevations in areas where minimal motion occurs (for

example in the brain). An advantage of the technique is that it should be able, at least in theory, to measure perfusion, which could be useful for estimating the effective delivered heat to tissue.[141] Fatty tissue has a low diffusion coefficient as well as a short T_2^*, yielding a less favorable SNR. Lesions cannot be visualized, thereby requiring additional scanning. It is suggested that irreversible tissue damage changes the diffusion coefficient, so that accuracy is compromised.[142]

Classical chemical-shift imaging suffers from very long scan times, making the technique unsuitable for real-time applications. However ongoing work that focuses on single-shot acquisition methods addresses this limitation.[87,88,143] If this limitation is resolved, the technique may have high potential. However, lesions need be visualized using additional scanning, and both temperature range and spatial resolution seem limited.

Proton frequency shift is limited to non-fatty tissue or requires a fat-suppression technique. Due to its good sensitivity and accuracy it seems the current method of choice for accurate MR thermometry. Dislocation invalidates the technique, thereby requiring stringent absence of motion or compensation techniques. Susceptibility effects are always present from different sources,[119,120,122,144] and must be corrected for.[145]

Ablation of tissue, as in laser thermoablation, places no absolute demands on thermometric accuracy. T_1-weighted thermometry is therefore probably suitable for monitoring of clinical ablative procedures. Hyperthermia, however, requires a suggested accuracy of 1°C at an voxel size of 2.8 mm^3 with an temporal resolution of one second.[104] At this time phase shift imaging seems the most promising thermometry technique to meet these demands.

Recent research efforts have mainly focused on improving phase imaging, resulting in proposals for improved elimination of phase-wraparound and improved immunity to motion.[146] The feasibility of mixing the chemical shift potential with phase mapping, to increase the accuracy of temperature measurements, has been addressed.[143,146] In signal processing the use of a complex difference image has shown a potential of 40% increased sensitivity over standard phase imaging,[147] which is probably most beneficial in low-field MRI, typical for interventional MRI. New thermometry sequences (principles of echo-shifting with a train of observations[148] and interleaved spiral gradient echo[149]) yield very fast and accurate temperature measurements and may signify a major step forward in phase mapping.[96,98,100] Isotherms in the range from 60-65°C are reported to be indicative of laser-induced lesion, e.g. in *ex-vivo* pig brains (N=6).[103] However for individual lesions, the T_1-weighted thermosensitive MR images have been shown to be inaccurate.[29,135,150-155]

REFERENCES

1. Reimer P, Bremer C, Horch C, Morgenroth C, Allkemper T, Schuierer G. MR-monitored LITT as a palliative concept in patients with high grade gliomas: preliminary clinical experience. J Magn Reson Imaging 1998;8(1):240-244.
2. Vogl TJ, Mack MG, Muller P, Phillip C, Bottcher H, Roggan A, Juergens M, Deimling M, Knobber D, Wust P, et al. Recurrent nasopharyngeal tumors: preliminary clinical results with interventional MR imaging--controlled laser-induced thermotherapy. Radiology 1995;196(3):725-733.
3. Kahn T, Bettag M, Harth T, Schwabe B, Schwarzmaier HJ, Modder U. Laser-induced interstitial induced hyperthermia of cerebral tumors with nuclear magnetic resonance tomography control.Radiologe 1996;36(9):713-721.
4. Jager L, Muller-Lisse GU, Gutmann R, Feyh J, Thoma M, Reiser M. Initial results with MRI-controlled laser-induced interstitial thermotherapy of head and neck tumors. Radiologe 1996;36(3):236-244.
5. Vogl TJ, Weinhold N, Mack MG, Muller PK, Scholz WR, Straub R, Roggan A, Felix R. Verification of MR thermometry by means of an in vivo intralesional, fluoroptic temperature measurement for laser-induced thermotherapy ov liver metastases. Rofo Fortschr Geb Rontgenstr Neuen Bildgeb Verfahr 1998;169(2):182-188.
6. Vogl TJ, Mack MG, Straub R, Roggan A, Felix R. Magnetic resonance imaging--guided abdominal interventional radiology: laser-induced thermotherapy of liver metastases. Endoscopy 1997;29(6):577-583.
7. Mack MG, Straub R, Eichler KC, Engelman K, Roggan A, Vogl TJ. MR-guided laser-induced thermotherapy (LITT) of liver metastaes: indications, complications, imaging criteria and local tumor control rate: experience after 2138 laser applications in 822 metastases. 1999 22-28 May 1999; Philadelphia, pennsylvania. ISMRM. p 1944.
8. Reither K, Wacker F, Ritz J, Germer CT, Roggan A, Wolf K-J. MR-guided interstitial laser-induced thermotherapy of focal liver lesions in a low-field MR system: first clinical results. 1999 16-19 september 1999; Sevilla. p 101.
9. Hosten N, Puls R, Kreißig R, Wlodarczyk W, Stoszczynski C, Hentschel M, Felix R. In vivo temperature measurements in comparison with MR-thermometry during laser-induced interstitial thermotherapy (LITT) of liver metastasis. Proceedings of International Society for Magnetic Resonance in Medicine 2000.
10. Madio DP, van Gelderen P, DesPres D, Olson AW, de Zwart JA, Fawcett TW, Holbrook NJ, Mandel M, Moonen CT. On the feasibility of MRI-guided focused ultrasound for local induction of gene expression. J Magn Reson Imaging 1998;8(1):101-104.
11. Kim S. Liposomes as carriers of cancer chemotherapy. Current status and future prospects. Drugs 1993;46(4):618-638.
12. van der Zee J, Gonzalez GD. The Dutch Deep Hyperthermia Trial: results in cervical cancer. Int J Hyperthermia 2002;18(1):1-12.
13. Lagendijk JJ. Hyperthermia treatment planning. Phys Med Biol 2000;45(5):R61-76.
14. Jolesz FA, Bleier AR, Jakab P, Ruenzel PW, Huttl K, Jako GJ. MR imaging of laser-tissue interactions. Radiology 1988;168(1):249-253.
15. Sapareto SA, Dewey WC. Thermal dose determination in cancer therapy. Int J Radiat Oncol Biol Phys 1984;10(6):787-800.
16. de Zwart JA. Fast magnetic resonance temperature imaging for control of localized hyperthermia in medicine. Bordeaux: Université Victor Segalen Bordeaux 2; 2000. 187 p.
17. Le Bihan D, Delannoy J, Levin RL. Temperature mapping with MR imaging of molecular diffusion: application to hyperthermia. Radiology 1989;171(3):853-857.
18. Weast RC. CRC Handbook of Chemistry and Physics: CRCPress, Cleveland, Ohio; 1975.
19. Hindman JC. Proton resonance shift of water in gas and liquid states. J Chem Phys 1966;44:4582-4592.

20. Schneider WG, Bernstein HJ, Pople JA. Proton magnetic resonance chemical shift of free (gaseous) and associated (liquid) hydride molecules. J Chem Phys 1985;28(4):601-607.
21. Graham SJ, Stanisz GJ, Kecojevic A, Bronskill MJ, Henkelman RM. Analysis of changes in MR properties of tissues after heat treatment. Magn Reson Med 1999;42(6):1061-1071.
22. Nelson TR, Tung SM. Temperature dependence of proton relaxation times in vitro. Magn Reson Imaging 1987;5(3):189-199.
23. Graham SJ, Bronskill MJ, Henkelman RM. Time and temperature dependence of MR parameters during thermal coagulation of ex vivo rabbit muscle. Magn Reson Med 1998;39(2):198-203.
24. Matsumoto R, Mulkern RV, Hushek SG, Jolesz FA. Tissue temperature monitoring for thermal interventional therapy: comparison of T_1-weighted MR sequences. J Magn Reson Imaging 1994;4(1):65-70.
25. Butts K, Sinclair J, Daniel BL, Wansapura J, Pauly JM. Temperature quantitation and mapping of frozen tissue. J Magn Reson Imaging 2001;13(1):99-104.
26. Beuthan J, Gewiese B, Fobbe F, Germer C, Albrecht D, Boese-Landgraf J, Roggan A, Müller G. Investigations of MRI-controlled laser-induced interstitial thermo-therapy (LITT). Minimal Invasive Medizin - MedTech 1993;4(4):27-30.
27. Dickinson RJ, Hall AS, Hind AJ, Young IR. Measurement of changes in tissue temperature using MR imaging. J Comput Assist Tomogr 1986;10(3):468-472.
28. Bottomley PA, Foster TH, Argersinger RE, Pfeifer LM. A review of normal tissue hydrogen NMR relaxation times and relaxation mechanisms from 1-100 MHz: dependence on tissue type, NMR frequency, temperature, species, excision, and age. Med Phys 1984;11(4):425-448.
29. Steiner P, Schoenenberger AW, Erhart P, Penner E, von Schulthess GK, Debatin JF. Imaging temperature changes in an interventional 0.5 T magnet: in-vitro results. Lasers Surg Med 1997;21(5):464-473.
30. Lewa CJ, Majewska Z. Temperature relationships of proton spin-lattice relaxation time T_1 in biological tissues. Bull Cancer 1980;67(5):525-530.
31. Wlodarczyk W, Hentschel M, Wust P, Noeske R, Hosten N, Rinneberg H, Felix R. Comparison of four magnetic resonance methods for mapping small temperature changes. Phys Med Biol 1999;44(2):607-624.
32. Wlodarczyk W, Boroschewski R, Hentschel M, Wust P, Mönich G, Felix R. Three-dimensional monitoring of small temperature changes for therapeutic hyperthermia using MR. J Magn Reson Imaging 1998;8(1):165-174.
33. Bohris C, Schreiber WG, Jenne J, Simiantonakis I, Rastert R, Zabel HJ, Huber P, Bader R, Brix G. Quantitative MR temperature monitoring of high-intensity focused ultrasound therapy. Magn Reson Imaging 1999;17(4):603-610.
34. Young IR, Hand JW, Oatridge A, Prior MV, Forse GR. Further observations on the measurement of tissue T_1 to monitor temperature in vivo by MRI. Magn Reson Med 1994;31(3):342-345.
35. Binzoni T, Hiltbrand E, Kayser B, Ferretti G, Terrier F. Human intramuscular temperature and heat flow transients at rest. J Appl Physiol 1995;79(5):1736-1743.
36. Lewa CJ, de Certaines JD. Measurements of the effect of storage at various temperatures on the T_1 of ex vivo tissues. Med Phys 1995;22(6):831-834.
37. Dick EA, Joarder R, de Jode M, Taylor-Robinson SD, Thomas HC, Foster GR, Gedroyc WM. MR-guided laser thermal ablation of primary and secondary liver tumours. Clin Radiol 2003;58(2):112-120.
38. Dick EA, Wragg P, Joarder R, de Jode M, Lamb G, Gould S, Gedroyc WM. Feasibility of abdomino-pelvic T_1-weighted real-time thermal mapping of laser ablation. J Magn Reson Imaging 2003;17(2):197-205.
39. Pignoli E, Marchesini R, Curti L, Sichirollo AE, Tomatis S, Musumeci R. Potential and limitations of magnetic resonance imaging for real-time monitoring of interstitial laser phototherapy. Acad Radiol 1995;2(9):741-747.

40. Fan M, Ascher PW, Schrottner O, Ebner F, Germann RH, Kleinert R. Interstitial 1.06 Nd:YAG laser thermotherapy for brain tumors under real-time monitoring of MRI: experimental study and phase I clinical trial. J Clin Laser Med Surg 1992;10(5):355-361.

41. Mueller-Lisse UG, Heuck AF, Thoma M, Muschter R, Schneede P, Weninger E, Faber S, Hofstetter A, Reiser MF. Predictability of the size of laser-induced lesions in T_1-Weighted MR images obtained during interstitial laser-induced thermotherapy of benign prostatic hyperplasia. J Magn Reson Imaging 1998;8(1):31-39.

42. Gewiese B, Beuthan J, Fobbe F, Stiller D, Müller G, Böse Landgraf J, Wolf KJ, Deimling M. Magnetic resonance imaging-controlled laser-induced interstitial thermotherapy. Invest Radiol 1994;29(3):345-351.

43. Schwarzbauer C, Zange J, Adolf H, Deichmann R, Noth U, Haase A. Fast measurement of temperature distributions by rapid T-1 mapping. J Magn Reson B 1995;106(2):178-180.

44. Anzai Y, Lufkin RB, Saxton RE, Fetterman H, Farahani K, Layfield LJ, Jolesz FC, Hanafee WH, Castro DJ. Nd: YAG interstitial laser phototherapy guided by magnetic resonance imaging in an ex vivo model: dosimetry of laser-MR-tissue interaction. Laryngoscope 1991;101(7 Pt 1):755-760.

45. Roberts HS, Paley M, Sams VR, Wilkinson ID, Lees WR, Hall-Craggs MA, Bown SG. Magnetic resonance imaging of interstitial laser photocoagulation of normal rat liver: imaging-histopathological correlation. Min Invas Ther & Allied Technol 1997(6):41-52.

46. Roberts HS, Paley M, Sams VR, Wilkinson ID, Lees WR, Hall-Craggs MA, Bown SG. Magnetic resonance imaging control of laser destruction of hepatic metastases: correlation with post-operative dynamical helical CT. Min Invas Ther & Allied Technol 1997(6):53-64.

47. Bremer C, Kreft G, Filler T, Reimer P. Accuracy of non-enhanced MRI to monitor histological lesion size during laser-induced interstitial thermotherapy. Eur Radiol 2002;12(1):237-244.

48. Schoenenberger AW, Steiner P, Debatin JF, Zweifel K, Erhart P, von Schulthess GK, Hodler J. Real-time monitoring of laser diskectomies with a superconducting, open- configuration MR system. AJR Am J Roentgenol 1997;169(3):863-867.

49. Steiner P, Zweifel K, Botnar R, Schoenenberger AW, Debatin JF, von Schulthess GK, Hodler J. MR guidance of laser disc decompression: preliminary in vivo experience. Eur Radiol 1998;8(4):592-597.

50. Melzer A, Tonmsenn F, Seibel R. MRI controlled percutaneous laser nucleotomy of lumbar intervertebral disk herniation MRPLNT. 1999 16-19 september 1999; Sevilla. p 101-102.

51. Mueller-Lisse UG, Thoma M, Faber S, Heuck AF, Muschter R, Schneede P, Weninger E, Hofstetter AG, Reiser MF. Coagulative interstitial laser-induced thermotherapy of benign prostatic hyperplasia: online imaging with a T_2-weighted fast spin-echo MR sequence--experience in six patients. Radiology 1999;210(2):373-379.

52. Law P, Gedroyc W, Regan L. Magnetic resonance guided laser ablation of uterine fibroids. ESMRB 1999 16-19 september 1999; Sevilla. p 101.

53. Hynynen K, McDannold N, Mulkern RV, Jolesz FA. Temperature monitoring in fat with MRI. Magn Reson Med 2000;43(6):901-904.

54. de Jode MG, Vale JA, Gedroyc WM. MR-guided laser thermoablation of inoperable renal tumors in an open- configuration interventional MR scanner: preliminary clinical experience in three cases. J Magn Reson Imaging 1999;10(4):545-549.

55. Dick EA, Joarder R, De Jode MG, Wragg P, Vale JA, Gedroyc WM. Magnetic resonance imaging-guided laser thermal ablation of renal tumours. BJU Int 2002;90(9):814-822.

56. Hindley JT, Law PA, Hickey M, Smith SC, Lamping DL, Gedroyc WM, Regan L. Clinical outcomes following percutaneous magnetic resonance image guided laser ablation of symptomatic uterine fibroids. Hum Reprod 2002;17(10):2737-2741.

57. Wacker FK, Cholewa D, Roggan A, Schilling A, Waldschmidt J, Wolf KJ. Vascular lesions in children: percutaneous MR imaging-guided interstitial Nd:YAG laser therapy--preliminary experience. Radiology 1998;208(3):789-794.

58. Il'yasov KA, Hennig J. Single-shot diffusion-weighted RARE sequence: application for temperature monitoring during hyperthermia session. J Magn Reson Imaging 1998;8(6):1296-1305.
59. Morvan D, Leroy-Willig A, Jehenson P, Cuenod CA, Syrota A. Temperature changes induced in human muscle by radio-frequency H-1 decoupling: measurement with an MR imaging diffusion technique. Work in progress. Radiology 1992;185(3):871-874.
60. Le Bihan D, Turner R, Douek P, Patronas N. Diffusion MR imaging: clinical applications. AJR Am J Roentgenol 1992;159(3):591-599.
61. Conturo TE, McKinstry RC, Aronovitz JA, Neil JJ. Diffusion MRI: precision, accuracy and flow effects. NMR Biomed 1995;8(7-8):307-332.
62. MacFall J, Prescott DM, Fullar E, Samulski TV. Temperature dependence of canine brain tissue diffusion coefficient measured in vivo with magnetic resonance echo-planar imaging. Int J Hyperthermia 1995;11(1):73-86.
63. Le Bihan D, Breton E, Lallemand D, Aubin ML, Vignaud J, Laval-Jeantet M. Separation of diffusion and perfusion in intravoxel incoherent motion MR imaging. Radiology 1988;168(2):497-505.
64. Simpson JH, Carr HY. Diffusion and nuclear spin relaxation in water. Phys Rev 1958;111:1201-1202.
65. Morvan D, Leroy-Willig A, Malgouyres A, Cuenod CA, Jehenson P, Syrota A. Simultaneous temperature and regional blood volume measurements in human muscle using an MRI fast diffusion technique. Magn Reson Med 1993;29(3):371-377.
66. Hall AS, Prior MV, Hand JW, Young IR, Dickinson RJ. Observation by MR imaging of in vivo temperature changes induced by radio frequency hyperthermia. J Comput Assist Tomogr 1990;14(3):430-436.
67. Le Bihan D, Turner R. Intravoxel incoherent motion imaging using spin echoes. Magn Reson Med 1991;19(2):221-227.
68. Stejskal EO, Tanner JO. Spin diffusion measurements: spin echoes in the presence of a time-dependent field gradient. J Chem Phys 1965;42:228-292.
69. Delannoy J, LeBihan D, Hoult DI, Levin RL. Hyperthermia system combined with a magnetic resonance imaging unit. Med Phys 1990;17(5):855-860.
70. Samulski TV, MacFall J, Zhang Y, Grant W, Charles C. Non-invasive thermometry using magnetic resonance diffusion imaging: potential for application in hyperthermic oncology. Int J Hyperthermia 1992;8(6):819-829.
71. Haselgrove JC, Moore JR. Correction for distortion of echo-planar images used to calculate the apparent diffusion coefficient. Magn Reson Med 1996;36(6):960-964.
72. Latta P, Jellus V, Budinsky L, Mlynarik V, Tkac I, Luypaert R. Motion artifacts reduction in DWI using navigator echoes: a robust and simple correction scheme. Magma 1998;7(1):21-27.
73. Bredella MA, Lang P, Gindele A, Wendland MF, Saeed M, Stauffer PR, Diderich CJ, Rosenau W, Gooding CA, Genant HK. Early Monitoring of Response to Hyperthermia in Rat Osteogenic Sarcoma Using Diffusion Weighted MR Imaging. 1998 18-24 April 1998; Sydney, Australia. ISMRM. p 69.
74. Cheng KH, Hernandez M. Magnetic resonance diffusion imaging detects structural damage in biological tissues upon hyperthermia. Cancer Res 1992;52(21):6066-6073.
75. Kuroda K, Abe K, Tsutsumi S, Ishihara Y, Suzuki Y, Sato K. Water proton magnetic resonance spectroscopic imaging. In: Mabuchi K, Mizushina S, Harrison B, editors. Advanced Techniques and Clinical Applications in Biomedical Thermology: Harwood academic publishers. p 43-62.
76. Haacke EM, Brown RW, Thompson MR, Venkatesan R. Magnetic Resonance Imaging, physical priciples and sequence design: John Wiley & Sons, Inc.; 1999. 914 p.
77. Mulkern RV, Chung AH, Jolesz FA, Hynynen K. Temperature monitoring of ultrasonically heated muscle with RARE chemical shift imaging. Med Phys 1997;24(12):1899-1906.

78. Kuroda K, Suzuki Y, Ishihara Y, Okamoto K. Temperature mapping using water proton chemical shift obtained with 3D- MRSI: feasibility in vivo. Magn Reson Med 1996;35(1):20-29.

79. Cady EB, D'Souza PC, Penrice J, Lorek A. The estimation of local brain temperature by in vivo 1H magnetic resonance spectroscopy. Magn Reson Med 1995;33(6):862-867.

80. Corbett RJ, Laptook AR, Tollefsbol G, Kim B. Validation of a noninvasive method to measure brain temperature in vivo using 1H NMR spectroscopy. J Neurochem 1995;64(3):1224-1230.

81. Corbett R, Laptook A, Weatherall P. Noninvasive measurements of human brain temperature using volume-localized proton magnetic resonance spectroscopy. J Cereb Blood Flow Metab 1997;17(4):363-369.

82. Zuo CS, Metz KR, Sun Y, Sherry AD. NMR temperature measurements using a paramagnetic lanthanide complex. J Magn Reson 1998;133(1):53-60.

83. Zuo CS, Bowers JL, Metz KR, Nosaka T, Sherry AD, Clouse ME. TmDOTP5-: a substance for NMR temperature measurements in vivo. Magn Reson Med 1996;36(6):955-959.

84. Frenzel T, Roth K, Kossler S, Raduchel B, Bauer H, Platzek J, Weinmann HJ. Noninvasive temperature measurement in vivo using a temperature- sensitive lanthanide complex and 1H magnetic resonance spectroscopy. Magn Reson Med 1996;35(3):364-369.

85. Hentschel M, Findeisen M, Schmidt W, Frenzel T, Wlodarczyk W, Wust P, Felix R. Is absolute noninvasive temperature measurement by the complex feasible. Magma 2000;10(1):52-59.

86. McDannold N, Hynynen K, Oshio K, Mulkern RV. Temperature monitoring with line scan echo planar spectroscopic imaging. Med Phys 2001;28(3):346-355.

87. Noeske R, Seifert F, Hentschel M, Felix R, Rinneberg H. Echo Planar Spectroscopic Imaging (EPSI) at 3 Tesla for Non-Invasive Temperature Measurements Using the Lanthanide Complex Pr-ME-DO3A. 1998 18-24 April 1998; Sydney, Australia. ISMRM. p 1873.

88. Kuroda K, Oshio K, Panych LP, Mulkern RV, Nakai T, Moriya T, Hynynen K, Jolesz FA. Temperature Mapping Using Water Proton Thermal Shift: Self-Referenced Method with EPSI. 1998 18-24 April 1998; Sydney, Australia. ISMRM. p 1990.

89. Kuroda K, Mulkern RV, Oshio K, Panych LP, Nakai T, Moriya T, Okuda S, Hynynen K, Joles FA. Temperature mapping using the water proton chemical shift: self- referenced method with echo-planar spectroscopic imaging. Magn Reson Med 2000;43(2):220-225.

90. Harth T, Kahn T, Rassek M, Schwabe B, Schwarzmaier HJ, Lewin JS, Mödder U. Determination of laser-induced temperature distributions using echo-shifted TurboFLASH. Magn Reson Med 1997;38(2):238-245.

91. Kuroda K, Chung AH, Hynynen K, Jolesz FA. Calibration of water proton chemical shift with temperature for noninvasive temperature imaging during focused ultrasound surgery. J Magn Reson Imaging 1998;8(1):175-181.

92. Chung YC, Duerk JL, Shankaranarayanan A, Hampke M, Merkle EM, Lewin JS. Temperature measurement using echo-shifted FLASH at low field for interventional MRI. J Magn Reson Imaging 1999;9(1):138-145.

93. Vogel MW, Pattynama PM, Lethimonnier FL, Le Roux P. Use of fast spin echo for phase shift magnetic resonance thermometry. J Magn Reson Imaging 2003;18(4):507-512.

94. Ishihara Y, Calderon A, Watanabe H, Okamoto K, Suzuki Y, Kuroda K. A precise and fast temperature mapping using water proton chemical shift. Magn Reson Med 1995;34(6):814-823.

95. Chung YC, Duerk JL. Signal formation in echo-shifted sequences. Magn Reson Med 1999;42(5):864-875.

96. de Zwart JA, van Gelderen P, Kelly DJ, Moonen CT. Fast magnetic-resonance temperature imaging. J Magn Reson B 1996;112(1):86-90.

97. de Zwart JA, Vimeux FC, Palussiere J, Delalande C, Moonen CT. Rapid MR temperature imaging for real-time visulization and control of focused ultrasound tissue heating. 1999 22-28 May 1999; Philadelphia, pennsylvania. ISMRM. p 401.
98. de Zwart JA, Vimeux FC, Delalande C, Canioni P, Moonen CT. Fast lipid-suppressed MR temperature mapping with echo-shifted gradient- echo imaging and spectral-spatial excitation. Magn Reson Med 1999;42(1):53-59.
99. Hillenbrand C, Löffler R, Deichmann R, Jakob PM, Reiser M, Hahn D, Haase A. Temperature Monitoring on a Clinical Scanner Using a Fast Hybrid Imaging Technique. 1998 18-24 April 1998; Sydney, Australia. ISMRM. p 700.
100. Stafford RJ, Hazle JD, Glover GH. Monitoring of high-intensity focused ultrasound-induced temperature changes in vitro using an interleaved spiral acquisition. Magn Reson Med 2000;43(6):909-912.
101. Vogel MW, Suprijanto, Pattynama PMT. Phase-shift based magnetic resonance thermometry during motion. 2004; Kyoto, Japan. pp 2702.
102. De Poorter J, De Wagter C, De Deene Y, Thomsen C, Ståhlberg F, Achten E. Noninvasive MRI thermometry with the proton resonance frequency (PRF) method: in vivo results in human muscle. Magn Reson Med 1995;33(1):74-81.
103. Schulze CP, Kahn T, Harth T, Schwurzmaier HJ, Schober R. Correlation of neuropathologic findings and phase-based MRI temperature maps in experimental laser-induced interstitial thermotherapy. J Magn Reson Imaging 1998;8(1):115-120.
104. Cetas TC. Will thermometric tomography become practical for hyperthermia treatment monitoring? Cancer Res 1984;44(10 Suppl):4805s-4808s.
105. Stollberger R, Ascher PW, Huber D, Renhart W, Radner H, Ebner F. Temperature monitoring of interstitial thermal tissue coagulation using MR phase images. J Magn Reson Imaging 1998;8(1):188-196.
106. Carter DL, MacFall JR, Clegg ST, Wan X, Prescott DM, Charles HC, Samulski TV. Magnetic resonance thermometry during hyperthermia for human high-grade sarcoma. Int J Radiat Oncol Biol Phys 1998;40(4):815-822.
107. Hynynen K, Vykhodtseva NI, Chung AH, Sorrentino V, Colucci V, Jolesz FA. Thermal effects of focused ultrasound on the brain: determination with MR imaging. Radiology 1997;204(1):247-253.
108. Vimeux FC, De Zwart JA, Palussiere J, Fawaz R, Delalande C, Canioni P, Grenier N, Moonen CT. Real-time control of focused ultrasound heating based on rapid MR thermometry. Invest Radiol 1999;34(3):190-193.
109. Salomir R, de Zwart JA, Vimeux FC, Moonen CT. Automatic temperature control in MRI guided FUS hyperthermia based on a physical model. 1999 16-19 september 1999; Sevilla. p 100-101.
110. McNichols RJ, Gowda A, Wright SM. MR-Guided Feedback Control of Laser Thermal Therapy. Proceedings of International Society for Magnetic Resonance in Medicine 1999:1345.
111. Vigen KK, Daniel BL, Pauly JM, Butts K. Triggered, navigated, multi-baseline method for proton resonance frequency temperature mapping with respiratory motion. Magn Reson Med 2003;50(5):1003-1010.
112. Weidensteiner C, Quesson B, Caire-Gana B, Kerioui N, Rullier A, Trillaud H, Moonen CT. Real-time MR temperature mapping of rabbit liver in vivo during thermal ablation. Magn Reson Med 2003;50(2):322-330.
113. Vogel MW, Suprijanto, Tived M, Pattynama PMT. Correction for positional errors in PRF based MR thermal maps by active tracking. 2003 10-16 July; Toronto, ON, CA. p 1204.
114. Rieke V, Vigen KK, Sommer G, Daniel BL, Pauly JM, Butts K. Referenceless PRF shift thermometry. Magn Reson Med 2004;51(6):1223-1231.
115. Hynynen K, McDannold NJ, Jolesz F. The feasibility of mri control of ultrasound surgery of large tumors. 1999; Philadelphia, Pennsylvania. ISMRM. p 1943.

116. Olsrud J, Wirestam R, Brockstedt S, Nilsson AM, Tranberg KG, StÅhlberg F, Persson BR. MRI thermometry in phantoms by use of the proton resonance frequency shift method: application to interstitial laser thermotherapy. Phys Med Biol 1998;43(9):2597-2613.

117. Stollberger R, Ascher PW, Leber K, Ebner F, Fuchs G, Baumgartner A, Litscher G, Hubmer M. Assessment of the influence of in vivo thermal response to interstitial laser coagulation on MR-temperature quantification using the phase method. 1999 22-28 May 1999; Philadelphia, Pennsylvania. ISMRM. p 400.

118. MacFall JR, Prescott DM, Charles HC, Samulski TV. 1H MRI phase thermometry in vivo in canine brain, muscle, and tumor tissue. Med Phys 1996;23(10):1775-1782.

119. Peters RD, Hinks RS, Henkelman RM. Heat-source orientation and geometry dependence in proton-resonance frequency shift magnetic resonance thermometry. Magn Reson Med 1999;41(5):909-918.

120. Peters RD, Henkelman RM. Proton-resonance frequency shift MR thermometry is affected by changes in the electrical conductivity of tissue. Magn Reson Med 2000;43(1):62-71.

121. Jakob PM, Hendrich C, Breitling T, Schafer A, Berden A, Haase A. Real time monitoring of laser-induced thermal changes in cartilage in vitro by using snapshot FLASH. Magn Reson Med 1997;37(5):805-808.

122. De Poorter J. Noninvasive MRI thermometry with the proton resonance frequency method: study of susceptibility effects. Magn Reson Med 1995;34(3):359-367.

123. Kahn T, Harth T, Kiwit JC, Schwarzmaier HJ, Wald C, Modder U. In vivo MRI thermometry using a phase-sensitive sequence: preliminary experience during MRI-guided laser-induced interstitial thermotherapy of brain tumors. J Magn Reson Imaging 1998;8(1):160-164.

124. Graham SJ, Chen L, Leitch M, Peters RD, Bronskill MJ, Foster FS, Henkelman RM, Plewes DB. Quantifying tissue damage due to focused ultrasound heating observed by MRI. Magn Reson Med 1999;41(2):321-328.

125. Sinha S, Oshiro T, Ong K, Sinha U, Daniell AL, Lu DS, Lufkin R. In-vivo laser ablation of a porcine model: real-time monitoring and tissue damage modeling. 1999 22-28 May 1999; Philadelphia, pennsylvania. ISMRM. p 1940.

126. Chung AH, Jolesz FA, Hynynen K. Thermal dosimetry of a focused ultrasound beam in vivo by magnetic resonance imaging. Med Phys 1999;26(9):2017-2026.

127. Peters RD, Trachtenberg J, Kucharczyk W, Henkelman RM. MR Thermometry for Predicting Thermal Damage: Interstitial Laser Coagulation in an In Vivo Canine Prostate. Proceedings of International Society for Magnetic Resonance in Medicine 1999;45.

128. McDannold NJ, King RL, Jolesz FA, Hynynen KH. Usefulness of MR imaging-derived thermometry and dosimetry in determining the threshold for tissue damage induced by thermal surgery in rabbits [In Process Citation]. Radiology 2000;216(2):517-523.

129. Hazle JD, Stafford RJ, Price RE. Magnetic resonance imaging-guided focused ultrasound thermal therapy in experimental animal models: correlation of ablation volumes with pathology in rabbit muscle and VX2 tumors. J Magn Reson Imaging 2002;15(2):185-194.

130. McDannold N, Hynynen K, Jolesz F. MRI monitoring of the thermal ablation of tissue: Effects of long exposure times. J Magn Reson Imaging 2001;13(3):421-427.

131. Chen JC, Moriarty JA, Derbyshire JA, Peters RD, Trachtenberg J, Bell SD, Doyle J, Arrelano R, Wright GA, Henkelman RM, Hinks RS, Lok SY, Toi A, Kucharczyk W. Prostate cancer: MR imaging and thermometry during microwave thermal ablation-initial experience. Radiology 2000;214(1):290-297.

132. Daum DR, Smith NB, King R, Hynynen K. In vivo demonstration of noninvasive thermal surgery of the liver and kidney using an ultrasonic phased array. Ultrasound Med Biol 1999;25(7):1087-1098.

133. Weidensteiner C, Kerioui N, Quesson B, de Senneville BD, Trillaud H, Moonen CT. Stability of real-time MR temperature mapping in healthy and diseased human liver. J Magn Reson Imaging 2004;19(4):438-446.

134. Vogl TJ, Mack MG, Roggan A, Straub R, Eichler KC, Muller PK, Knappe V, Felix R. Internally cooled power laser for MR-guided interstitial laser-induced thermotherapy of liver lesions: initial clinical results. Radiology 1998;209(2):381-385.

135. Steiner P, Botnar R, Dubno B, Zimmermann GG, Gazelle GS, Debatin JF. Radio-frequency-induced thermoablation: monitoring with T_1-weighted and proton-frequency-shift MR imaging in an interventional 0.5-T environment. Radiology 1998;206(3):803-810.

136. de Jode MG, Lamb GM, Thomas HC, Taylor-Robinson SD, Gedroyc WM. MRI guidance of infra-red laser liver tumour ablations, utilising an open MRI configuration system: technique and early progress. J Hepatol 1999;31(2):347-353.

137. Mietzsch E, Koch M, Schaldach M, Werner J, Bellenberg B, Wentz KU. Non-invasive temperature imaging of muscles with magnetic resonance imaging using spin-echo sequences. Med Biol Eng Comput 1998;36(6):673-678.

138. Fossheim SL, Il'yasov KA, Hennig J, Bjornerud A. Thermosensitive paramagnetic liposomes for temperature control during MR imaging-guided hyperthermia: in vitro feasibility studies. Acad Radiol 2000;7(12):1107-1115.

139. McDannold N, Fossheim SL, Rasmussen H, Martin H, Vykhodtseva N, Hynynen K. Heat-activated Liposomal MR Contrast Agent: Initial in Vivo Results in Rabbit Liver and Kidney. Radiology 2004;230(3):743-752.

140. Vogel MW, Entius C, Pattynama PMT. Monitoring tissue coagulation during thermo-ablative treatment by using a novel MRI contrast agent. Invest Radiol 2004, 39(11): 661-665.

141. Cline HE, Schenck JF, Watkins RD, Hynynen K, Jolesz FA. Magnetic resonance-guided thermal surgery. Magn Reson Med 1993;30(1):98-106.

142. Mueller-Lisse UG, Heuck AF. Control and monitoring of focal thermotherapy with magnetic resonance tomography. An overview. Radiologe 1998;38(3):200-209.

143. Kuroda K, Oshio K, Mulkern RV, Panych LP, Nakai T, Moriya T, Matsumura A, Okuda S, Hynynen K, Jolesz FA. Internally-referenced temperature mapping using echo planar spectroscopic imaging method for high water content tissues. 1999 22-28 May 1999; Philadelphia, pennsylvania. ISMRM. p 1930.

144. Young IR, Hajnal JV, Roberts IG, Ling JX, Hill-Cottingham RJ, Oatridge A, Wilson JA. An evaluation of the effects of susceptibility changes on the water chemical shift method of temperature measurement in human peripheral muscle. Magn Reson Med 1996;36(3):366-374.

145. Salomir R, de Zwart JA, Vimeux FC, Quesson B, Moonen CTW. Temperature-induced Changes in Magnetic Susceptibility in Local Hyperthermia: Correction of MR Thermometry. 2000 3-7 April 2000; Denver, Colorado. p 1349.

146. Mulkern RV, Panych LP, McDannold NJ, Jolesz FA, Hynynen K. Tissue temperature monitoring with multiple gradient-echo imaging sequences. J Magn Reson Imaging 1998;8(2):493-502.

147. Cline HE, Hynynen K, Schneider E, Hardy CJ, Maier SE, Watkins RD, Jolesz FA. Simultaneous magnetic resonance phase and magnitude temperature maps in muscle. Magn Reson Med 1996;35(3):309-315.

148. Liu G, Sobering G, Duyn J, Moonen CT. A functional MRI technique combining principles of echo-shifting with a train of observations (PRESTO). Magn Reson Med 1993;30(6):764-768.

149. Spielman DM, Pauly JM, Meyer CH. Magnetic resonance fluoroscopy using spirals with variable sampling densities. Magn Reson Med 1995;34(3):388-394.

150. Steiner P, Botnar R, Goldberg SN, Gazelle GS, Debatin JF. Monitoring of radio frequency tissue ablation in an interventional magnetic resonance environment. Preliminary ex vivo and in vivo results. Invest Radiol 1997;32(11):671-678.

151. Pushek T, Farahani K, Saxton RE, Soudant J, Lufkin R, Paiva M, Jongewaard N, Castro DJ. Dynamic MRI-guided interstitial laser therapy: a new technique for minimally invasive surgery. Laryngoscope 1995;105(11):1245-1252.

152. Mueller-Lisse GU, Heuck A, Stehling MK, Frimberger M, Thoma M, Schneede P, Muschter R, Hofstetter A, Reiser M. MRI monitoring before, during and after interstitial laser-induced hyperthermia of benign prostatic hyperplasia. Initial clinical experiences. Radiologe 1996;36(9):722-731.

153. Fried MP, Morrison PR, Hushek SG, Kernahan GA, Jolesz FA. Dynamic T_1-weighted magnetic resonance imaging of interstitial laser photocoagulation in the liver: observations on in vivo temperature sensitivity. Lasers Surg Med 1996;18(4):410-419.

154. Kahn T, Bettag M, Ulrich F, Schwarzmaier HJ, Schober R, Furst G, Modder U. MRI-guided laser-induced interstitial thermotherapy of cerebral neoplasms. J Comput Assist Tomogr 1994;18(4):519-532.

155. Morrison PR, Jolesz FA, Charous D, Mulkern RV, Hushek SG, Margolis R, Fried MP. MRI of laser-induced interstitial thermal injury in an in vivo animal liver model with histologic correlation. J Magn Reson Imaging 1998;8(1):57-63.

156. Germain D, Chevallier P, Laurent A, Saint-Jalmes H. MR monitoring of tumour thermal therapy. Magma 2001;13(1):47-59.

157. Freimarck RD. Magnetic Resonance Tissue Contrast Characteristics: Proton (Spin) Density, T_1 and T_2. In: Woodward P, Freimarck RD, editors. MRI for technologists. Volume 3. New York: McGraw-Hill, Inc; 1995. p 27-36.

158. Nitz WR, Reimer P. Contrast mechanisms in MR imaging. Eur Radiol 1999;9(6):1032-1046.

159. Yamada I, Aung W, Himeno Y, Nakagawa T, Shibuya H. Diffusion coefficients in abdominal organs and hepatic lesions: evaluation with intravoxel incoherent motion echo-planar MR imaging. Radiology 1999;210(3):617-623.

160. Turner R, Le Bihan D, Maier J, Vavrek R, Hedges LK, Pekar J. Echo-planar imaging of intravoxel incoherent motion. Radiology 1990;177(2):407-414.

161. Sinha S, Oshiro T, Sinha U, Lufkin R. Phase imaging on a.2-T MR scanner: application to temperature monitoring during ablation procedures. J Magn Reson Imaging 1997;7(5):918-928.

162. Kahn T, Harth T, Schwabe B, Schwarzmaier HJ, Modder U. MR tomographic temperature quantification at 1.5 T in vitro: a comparison of fast T_1 maps and a phase-sensitive sequence. Rofo Fortschr Geb Rontgenstr Neuen Bildgeb Verfahr 1997;167(2):187- 193.

163. Chung YC, Duerk JL, Shankaranarayanan A, Hampke M, Merkle EM, Clouse ME, Lewin JS. Temperature Imaging in a 0.2T Open Magnet Using Echo-Shifted Turbo-Flash. 1998 18-24 April 1998; Sydney, Australia. ISMRM. p 1996.

164. Bertsch F, Mattner J, Stehling MK, Muller-Lisse U, Peller M, Loeffler R, Weber J, Messmer K, Wilmanns W, Issels R, Reiser M. Non-invasive temperature mapping using MRI: comparison of two methods based on chemical shift and T_1-relaxation. Magn Reson Imaging 1998;16(4):393-404.

165. Delannoy J, Chen CN, Turner R, Levin RL, Le Bihan D. Noninvasive temperature imaging using diffusion MRI. Magn Reson Med 1991;19(2):333-339.

166. Bleier AR, Jolesz FA, Cohen MS, Weisskoff RM, Dalcanton JJ, Higuchi N, Feinberg DA, Rosen BR, McKinstry RC, Hushek SG. Real-time magnetic resonance imaging of laser heat deposition in tissue. Magn Reson Med 1991;21(1):132-137.

167. Young IR, Bell JD, Hajnal JV, Jenkinson G, Ling J. Evaluation of the stability of the proton chemical shifts of some metabolites other than water during thermal cycling of normal human muscle tissue. J Magn Reson Imaging 1998;8(5):1114-1118.

168. Aime S, Botta M, Fasano M, Terreno E, Kinchesh P, Calabi L, Paleari L. A new ytterbium chelate as contrast agent in chemical shift imaging and temperature sensitive probe for MR spectroscopy. Magn Reson Med 1996;35(5):648-651.

169. Moriarty JA, Chen JC, Purcell CM, Ang LC, Hinks RS, Peters RD, Henkelman RM, Plewes DB, Bronskill MJ, Kucharczyk W. MRI monitoring of interstitial microwave-induced heating and thermal lesions in rabbit brain in vivo. J Magn Reson Imaging 1998;8(1):128-135.

170. Hasegawa Y, Latour LL, Sotak CH, Dardzinski BJ, Fisher M. Temperature dependent change of apparent diffusion coefficient of water in normal and ischemic brain of rats. J Cereb Blood Flow Metab 1994;14(3):383-390.
171. Bland JM, Altman DG. Statistical methods for assessing agreement between two methods of clinical measurement. Lancet 1986;1(8476):307-310.

Comparison of Temperature Sensitivity of T₁-based and Proton Resonance Frequency Shift-based MR Thermometry at 1.5 and 3.0 T Clinical Scanners

Chapter 2

Mika W. Vogel, MSc ◆
Suprijanto, MSc ✳
Peter M.T. Pattynama, PhD, MD ◆

ABSTRACT

The temperature sensitivity of both spin-lattice relaxation time (T_1) and proton resonance frequency shift (PRF) allows monitoring of thermal coagulation therapy. With the advent of high field scanners, thermal precision and sensitivity may increase, and advocate MR-guided thermal ablation at higher field strengths. We assessed thermal sensitivity and precision in gel and *ex-vivo* muscle, kidney and liver for both methods at 1.5 and 3.0 T clinical scanners. For the PRF method we found an increase in temperature sensitivity with increasing field strength. In contrast we found consistent lower thermal sensitivities in T_1 at 3.0T compared to 1.5T. Thermal accuracy did not improve for the T_1 methods at 3.0 T.

From
◆ Department of Radiology, Erasmus MC, University Medical Center Rotterdam, The Netherlands.
✳ Department of Applied Physics, Delft University of Technology, The Netherlands.

INTRODUCTION

Percutaneous thermal ablation of tumor tissue is gaining increasing acceptance and popularity as a patient-friendly, minimally invasive alternative to open surgical tumor resection. However, adequate control over the extent of coagulation, is required for precise targeted tissue destruction. The ability to monitor the progression of treatment in real time - to decide when the treatment is complete and should be stopped to avoid destruction of too much healthy surrounding tissue - is therefore of critical importance.

A particularly attractive method to monitor thermo-ablative treatment is by real-time imaging of the tissue's temperature with magnetic resonance (MR) thermometry. Methods based on changes in diffusion, proton resonance frequency (PRF), chemical shift, and spin-lattice relaxation (T_1) time have been explored. Of these, the T_1-based and PRF-based MR thermometry are the most commonly used methods in pre-clinical settings.

From previous literature reports it is known that the PRF method outperforms the T_1 method at field strengths of 0.5 T[1] and 1.5 T.[2-4] The PRF-based method can provide more accurate temperature estimates that, other than T_1-based MR thermometry, are independent of the specific tissue type under consideration. Currently we are witnessing a general trend towards the use of more high-field MR scanners. Theoretically, one could expect that both methods should improve by this, given the larger signal-to-noise ratio and larger chemical shift at higher field strengths. However, the true effect of increased field strength on the accuracy of T_1- and PRF-based MR thermometry has not been studied. Therefore, it was our aim to assess precision of temperature calculation comparing the T_1 and PRF methods at 1.5 and 3T field strengths.

MATERIALS AND METHODS

MR thermometry methods

The intrinsic T_1-values of tissue depend primarily on the distribution of free and bound water, and the presence of macromolecules, such as proteins. The T_1-relaxation of free water (T_{1f}) is thought to be independent of field strength. Encountered changes in T_1 with increasing field strength are therefore attributed to the bound fraction. The common assumption that the bound fraction has no temperature dependence leads to the following model for T_1 at temperature T [5]:

$$T_{1_T} \approx T_{1f}\, e^{\frac{-Ea}{kT}} \tag{1}$$

The temperature sensitivity of T_1 (expressed as ms/°C) increases with increasing magnetic field strength (from 0.1 to 1.4 T) in muscle and liver tissue.[5] Consequently it was hypothesized that T_1 sensitivity increases,[5] just like T_1 of tissue, as

$$\frac{\partial T_1}{\partial T} \approx (\gamma B_0)^{\frac{1}{3}}$$

(2)

If this model is valid, this would potentially improve the thermal precision because increased changes in T_1 are easier to detect. A three-fold increase in sensitivity would then, theoretically, be expected when going from a 0.02 T to 0.5 T MR scanner; going from 0.5 to 3.0 T would result in an 80% increase in sensitivity.

The PRF shift is a shift in resonance frequency of water protons that is caused by a change in the efficiency of the shielding electrons of the water proton under the influence of temperature.[6] With increasing temperature, water protons become more diamagnetic with a temperature sensitivity a of -0.01 ppm/°C. This small change can be detected as a phase change ($\Delta\phi$) in the complex image. A temperature difference ΔT is then calculated using [7]:

$$\Delta T = \frac{\Delta \varphi}{\gamma \cdot \alpha \cdot B_0 \cdot \tau}$$

(3)

where γ is the gyromagnetic ration, B_0 is the main magnetic field, and τ is the sensitization time, which allows for the build up of the PRF. Theoretically, the temperature sensitivity (expressed as radians /°C) will change linearly with changes in main magnetic field strength. The temperature sensitivity a is presumed independent of tissue type.[8] The presence of fat ($-CH_2-$ chains) introduces a non-temperature dependent term in the phase measurements, that may bias the estimate of the temperature change. Fat suppression will negate this effect.[9]

In the present study, we assessed the sensitivity and precision of PRF-based and T_1-based MR thermometry in gel phantoms and in various tissues at 1.5T and 3.0T, using fiberoptic thermometry as the reference method. MR thermometry was performed on a 1.5T (CV/i, General Electric, Milwaukee, WI, with LX9.1 software, 40mTm⁻¹ gradients and 268 µs slew rate) and a 3.0T MR scanner (VH3, General Electric, Milwaukee, Wisconsin, USA, with M3 software, 40mTm⁻¹ gradients and 268 µs slew rate) and by using a standard head coil in both scanners.

MR thermometry in heated gels

Gels (5% agar, Sigma; 95% distilled water, $T_2{*}=45.4\pm0.8$ ms) were uniformly heated up to 65°C and positioned it in a Styrofoam box in the two MR scanners. During the slow cooling down of the gel we acquired images using a multi-point turboFLASH[10] for T_1-based MR thermometry and an echo-shifted gradient recalled echo sequence[11] for PRF-based thermometry. A fiberoptic temperature sensor (Luxtron 790, Luxtron Corporation, Santa Clara), placed in the gel, served

as the reference method for thermometry. The imaging sequences were adapted to obtain one measurement during a 2 sec acquisition period. In each measurement, the turboFLASH (θ/TI/TE/TR=5/21ms/1.2ms/ 3.9ms at 1.5T and θ/TI/TE/TR=5/24ms/1.4ms/4.3ms at 3.0T) acquired 5 images with a resolution of 2 mm in-plane, with 5 mm slice thickness. The echo-shifted sequence (θ/TE/TR=10°/20ms/15ms at both field strengths) had a spatial resolution of 1x1 mm with 5 mm slice thickness. The resolution of the snapshot FLASH techniques was reduced with regard to the echo-shifted sequence in order to acquire sufficient samples for T_1 relaxation quantification.

MR thermometry in heated tissues

Next, we quantified PRF- and T_1- changes with increasing temperatures in various tissue types at 1.5 and 3.0T field strengths versus fiberoptic thermometry as the gold standard. The resulting precision of MR thermometry based on these PRF- and T_1-changes was then determined. Samples of excised porcine muscle, whole liver and kidney tissue were positioned in saline in histology containers and placed in a water reservoir. The tissue samples were slowly and homogeneously heated by using continuously circulating water at a controlled temperature as described before.[8] The temperature in the water bath was raised from ambient temperature (18 °C) to 55 °C over a 3-hours-period, or a mean rate of temperature rise of 0.2 °C/min. During heating, continuous MR imaging was performed.

We quantified PRF changes by using a dedicated RF-spoiled, single-polarity, eight echo, flow compensated, fast spoiled gradient echo sequence (θ/TR/BW=10°/60ms/62.5 KHz) with 0.6 mm in-plane resolution and a slice thickness of 5 mm. From each echo a full image was reconstructed with echo times of 6.2 ms + 5.3 ms increment per echo. For quantification of T_1, we used a flow compensated, inversion recovery, unipolar even-echo EPI sequence (θ/TE/TR/BW=90°/60ms/10000ms/62.5 KHz) with 5 mm isotropic resolution. Ten acquisitions were made with inversion times of 50 ms + 150 ms per acquisition. To suppress the signal from fat, the fast spoiled gradient echo sequence used a chemically selective inversion pulse for each TR; the EPI sequence employed a spectral-spatial water selective excitation pulse.

Data analysis

All MR imaging data were transferred off-line to a workstation running IDL 5.4 for Windows (RSI, Boulder, CO). T_1–changes and PRF shifts were calculated and plotted versus the fiberoptic temperature measurements as the gold standard. Linear regression established the temperature sensitivities, and forward stepwise regression with field strength was employed to assess differences in temperature sensitivities for the two field strengths. Absolute residuals from the regression analysis per field strength were compared using ANOVA. Differences were

deemed significant at p = 0.05. Thermal precision was defined as the standard deviation of the residuals. Differences were deemed significant at p = 0.05.

Gel experiment

T_1-values of the gel were calculated by a least squares fit (Levenberg-Marquardt) of the mean magnitude in a large region of interest to the following function [12]:

$$S_{TI} = \left| A - Be^{-\frac{TI}{T_1^*}} \right| \tag{4}$$

Where A denotes apparent magnetization M_0^* and B the magnetization $M_0 + A$. T1 is then calculated as described before[12] :

$$T_1 = T_1^* \frac{B - A}{A} \tag{5}$$

For quantification of PRF, we performed complex subtraction between subsequent images to avoid phase wraps, and accumulated the mean phase value in the region of interest. This phase value was converted to temperature using equation 3.

Tissue experiment

On a pixel by pixel basis, we calculated T_1 by least squares (Levenberg-Marquardt) fitting the following standard inversion recovery function [13]:

$$S_{TI} = \left| M_0 (1 - 2e^{-\frac{TI}{T_1}}) \right| + err \tag{6}$$

were S_{TI} is the acquired signal for each TI value, M_0 is the available magnetization and err is an error term to compensate for receiver bias. From a small region of interest near the fiberoptic sensor, we calculated the temperature sensitivity by fitting the found T_1 values to temperature according to exponential model from equation 1.

The PRF shift was calculated for each TE independently. The phase images were corrected for potential wrap using Flynn's minimum discontinuity method.[14] The phase values from a region of interest near the fiberoptic thermometer were averaged for each image. Then, we performed a robust linear fit[15] to the phase values against the used echo times for each temperature independently. Temperature sensitivity was calculated by linear fit from the calculated frequency values to the recorded temperatures.

RESULTS

MR thermometry in heated gels

Contrary to what theory predicted, the temperature sensitivity of T_1-based MR thermometry did not improve, but decreased significantly when going from 1.5 to

3.0T (6.7 ± 0.1 ms / °C versus 4.8 ± 0.1 ms / °C, respectively) (p < 0.001), with standard deviation of the residuals of 68.6 and 56.8 ms. This corresponds to a thermal precision of 10.2 °C at 1.5T and 11.8 °C at 3.0T respectively. In addition, we found that T_1 at 1.5 T was on average 109 ± 4 ms longer (p < 0.001). Thus, both the thermal sensitivity and the precision of T_1-based MR thermometry method did not improve when the main magnetic field strength increased from 1.5 to 3.0T .

For PRF-based MR thermometry, the temperature sensitivities more than double when going from1.5 T to 3.0 T, with values of 0.467 ± 0.007 Hz/°C and 1.058 ± 0.008 Hz/°C, respectively (p < 0.001), with respective standard deviations of the residuals of 0.5°C and 0.8°C for 1.5 T and 3.0 T respectively. This indicates that sensitivity, but not precision, of the PRF method is increased at 3.0 T than at 1.5 T.

MR thermometry in heated tissues

The temperature range in the experiments was 15-56 degrees Celsius.
The results of the various experiments are tabulated in Tables 1 and 2; the relation between tissue temperature and T_1- and PRF-changes are shown in Figures 1 and 2 at 1.5 and 3.0T respectively.

Table 1. Precision, calculated as the standard deviation of the residual, of the temperature measurements for 1.5 and 3.0 T.

Field strength	T_1			PRF		
	1.5T	3.0T	p	1.5T	3.0T	p
Liver	3.92 °C	3.24 °C	0.106	0.54 °C	1.06 °C	0.024
Muscle	3.31 °C	3.65 °C	0.004	1.07 °C	0.22 °C	<0.001
Kidney	3.55 °C	3.49 °C	<0.001	1.17 °C	1.24 °C	<0.001

The experimentally found T_1-values of the different tissues were not significantly different from the theoretically predicted (p=0.116-0.888), with the exception muscle tissue at 3.0 T (p < 0.001). The results for T_1-based MR thermometry in heated tissues were consistent with the results found in the heated gels (again contradicting our initial expectation): the temperature sensitivity was worse, not better, with increasing magnetic field strength going from 1.5 to 3.0T. Thermal precision in the various tissues was not significantly different at 1.5 and 3.0T (Table-1). Differences between the temperature readings of the different Luxtron sensors showed a mean absolute difference of < 1.5°C for all experiments.

For PRF-based temperature measurement, we observed an increase in temperature sensitivities at 3.0T in comparison to 1.5 T (Table-2). The thermal precision, however, was comparable between the two field strengths (Table-1).

Table 2.   Calculated temperature sensitivities for 1.5T and 3.0T (range 20-60 °C, except for PRF method in the kidney at 3.0T : range 20-40 °C)

Field strength	T_1 (% /°C)			PRF (Hz /°C)		
	1.5T	3.0T	p	1.5T	3.0T	p
Liver	21.1 ± 2	18.1 ± 1	< 0.001	0.518 ± 0.001	1.348 ± 0.021	< 0.001
Muscle	17.8 ± 1	15.0 ± 2	< 0.001	0.596 ± 0.005	1.670 ± 0.001	< 0.001
Kidney	3.6 ± 1	3.5 ± 1		0.394 ± 0.015	1.022 ± 0.001	< 0.001
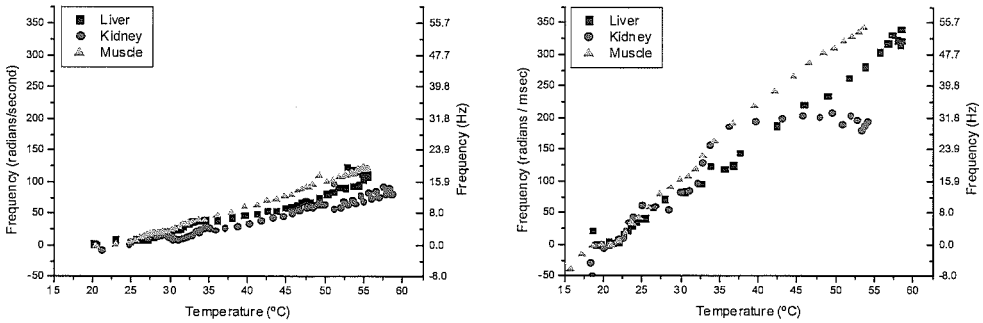
Figure 1.   Change of frequency versus temperature using 1.5 T (left) or 3.0T (right). Linearity holds well for muscle and liver, but from 30-35 °C, non-linear changes with temperature start to occur, most notably in the kidney.
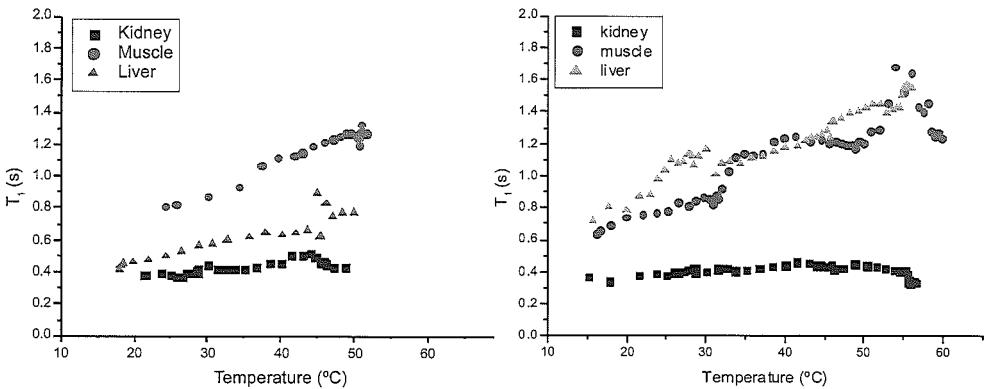
Figure 2.   Changes in T_1 with temperature at 1.5T (left) and 3.0T (right), for kidney (square), muscle (circle) and liver (diamond).

DISCUSSION

Our results show that for T_1-based MR thermometry, temperature sensitivity and thermal precision did not improve at higher field strength. This contradicts the commonly accepted model that predicts increased sensitivity at higher main magnetic field strength,[5] but our data are in fact consistent with a literature review

on experimental data.[16] This phenomenon is seen in all tissues, but more importantly, also in the gel experiment. Because of the absence of macromolecules (most notably proteins), the gel experiments is a good approximation for thermal sensitivity changes that occur in free water, to which the temperature sensitivity is typically attributed. A tentative explanation for the discrepancy with the commonly accepted model may be that the T_1-relaxation due to bound water fraction is becoming more dominant at high field. PRF-based MR thermometry showed the theoretically expected doubled temperature sensitivity when going from 1.5 to 3.0T, but this better thermal sensitivity did not result in increased thermal precision at 3.0 T in comparison to 1.5 T. We presume that the gain in SNR is probably offset by the increased effect of T_2* decay in our measurements.

In a one-on-one comparison, the PRF-based MR temperature measurements are more accurate than those of T_1-based MR thermometry, for all tissues at both 1.5 and 3.0T (with the single exception of muscle tissue at 1.5T). This is consistent with previous research[1-3] and literature reviews.[16-18] The empirically found T_1 values for tissue agree with the empirically predicted values, with exception of the muscle tissue at 3.0T. Also, the spread in sensitivities for the different tissues is much reduced for the PRF measurements, which reduces effects associated with incorrect calibration of the temperature sensitivity constant.

Both T_1 and PRF-based methods showed a dependency of the temperature sensitivity on tissue type. This is a well-known issue in T_1-based MR thermometry. Potential problems occur when more than one tissue type is present, because the combined change in relaxation will underestimate the individual relaxation times, and hence negatively influence temperature sensitivity. This effect increases as the two tissues are becoming more distinct in T_1, the overall estimated error in the actual thermal sensitivity is on the order of 5%.

Based on previous research reports in *ex-vivo* tissue samples, it is often stated that PRF-based MR thermometry shows no significant tissue dependency, that is, that the temperature sensitivities will be the same for several different tissue types.[8] However, in this previous study also, some tissue dependency was encountered, the temperature sensitivity in this study showing a 95% confidence interval of approximately ± 7.7 % (worst case ± 17.5 %). Variability in the temperature constant is problematic, as a deviation of 10 % accounts for a systematic temperature difference of 3 °C at a target temperature of 67 °C, regardless of other sources of error.

In our experiments, we found different temperature sensitivities for PRF in different tissues above 30-35°C. Changes in mass volume susceptibility account for local magnetic flux changes that confound the PRF method (typically on the order of 10%).[19] In addition, the blood denaturation due to heating could be another potential confounding mechanism. In figure 3, it is shown that vessels show markedly different flux changes when compared with surrounding tissue.
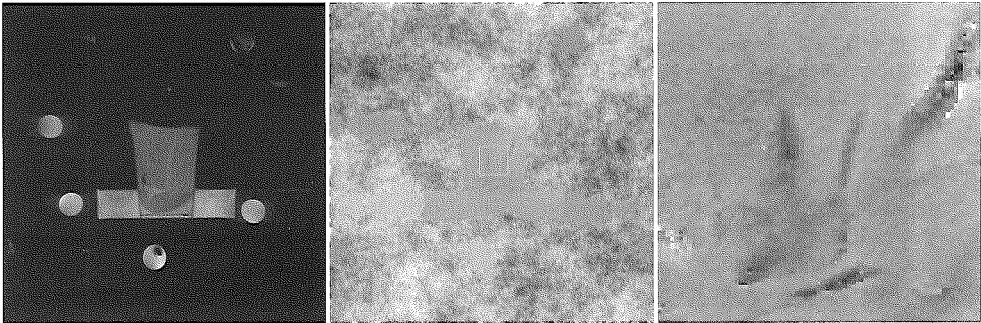
Figure 3. Example of experimental setup. Left, a sample of liver is shown in a container. Partially surrounded by reference markers for the PRF shift. In the center image, we see an unwrapped PRF subtraction map at 38°C. In the right image, the area in the yellow box is magnified and wrapped again, to improve clarity. It can be clearly seen that the PRF shift is inhomogeneous near the vasculature.

Temperature dependent changes in the electrical conductivity of tissue[20] are ruled out as a confounding factor because we used multi-echo acquisitions, which are intrinsically compensated by removal of the TE=0 phase value. It has been shown that the presence of fat potentially modulates the temperature sensitivity.[9] Due to the employed fat suppression and the absence of fat-like signal modulation in our multi-echo fast spoiled gradient echo sequence we could also rule out this confounding effect.

Both T_1 and PRF methods for temperature measurement have been shown feasible at the used field strengths. Our data suggests that higher field leads to increased sensitivity for the PRF method only. No increase of thermal precision was observed for either the T_1 or the PRF method. The T_1 method showed reduced sensitivity at high field, which was offset by intrinsic better signal-to-noise ratio. The PRF method showed better overall consistency, has potentially less problematic calibration, and should be the method of choice for quantitative MR thermometry applications.

REFERENCES

1. Steiner P, Botnar R, Dubno B, Zimmermann GG, Gazelle GS, Debatin JF. Radio-frequency-induced thermoablation: monitoring with T1-weighted and proton-frequency-shift MR imaging in an interventional 0.5-T environment. Radiology 1998; 206:803-810.
2. Kahn T, Harth T, Schwabe B, Schwarzmaier HJ, Modder U. MR tomographic temperature quantification at 1.5 T in vitro: a comparison of fast T1 maps and a phase-sensitive sequence. Rofo Fortschr Geb Rontgenstr Neuen Bildgeb Verfahr 1997; 167:187- 193.
3. Wlodarczyk W, Boroschewski R, Hentschel M, Wust P, Mönich G, Felix R. Three-dimensional monitoring of small temperature changes for therapeutic hyperthermia using MR. J Magn Reson Imaging 1998; 8:165-174.
4. Bertsch F, Mattner J, Stehling MK, et al. Non-invasive temperature mapping using MRI: comparison of two methods based on chemical shift and T1-relaxation. Magn Reson Imaging 1998; 16:393-404.

5.   Bottomley PA, Foster TH, Argersinger RE, Pfeifer LM. A review of normal tissue hydrogen NMR relaxation times and relaxation mechanisms from 1-100 MHz: dependence on tissue type, NMR frequency, temperature, species, excision, and age. Med Phys 1984; 11:425-448.
6.   Hindman JC. Proton resonance shift of water in gas and liquid states. J Chem Phys 1966; 44:4582-4592.
7.   Ishihara Y, Calderon A, Watanabe H, Okamoto K, Suzuki Y, Kuroda K. A precise and fast temperature mapping using water proton chemical shift. Magn Reson Med 1995; 34:814-823.
8.   Peters RD, Hinks RS, Henkelman RM. Ex vivo tissue-type independence in proton-resonance frequency shift MR thermometry. Magn Reson Med 1998; 40:454-459.
9.   de Zwart JA, Vimeux FC, Delalande C, Canioni P, Moonen CT. Fast lipid-suppressed MR temperature mapping with echo-shifted gradient- echo imaging and spectral-spatial   excitation. Magn Reson Med 1999; 42:53-59.
10. Nekolla S, Gneiting T, Syha J, Deichmann R, Haase A. T1 maps by K-space reduced snapshot-FLASH MRI. J Comput Assist Tomogr 1992; 16:327-332.
11. de Zwart JA, van Gelderen P, Kelly DJ, Moonen CT. Fast magnetic-resonance temperature imaging. J Magn Reson B 1996; 112:86-90.
12. Deichmann R, Hahn D, Haase A. Fast T1 mapping on a whole-body scanner. Magn Reson Med 1999; 42:206-209.
13. Haacke EM, Brown RW, Thompson MR, Venkatesan R. Magnetic Resonance Imaging, physical priciples and sequence design. first edition ed: John Wiley & Sons, Inc., 1999.
14. Ghiglia DC, Pritt MD. Two-dimensional Phase Unwrapping: Theory, Algorithms, and Software. New York: John Wiley and Sons, Inc., 1998.
15. Press WH, Teukolsky SA, Vetterling WT, Flannery BP. Numerical Recipes in C. Cambridge: Cambridge University Press, 1992. pp. 704-705.
16. Quesson B, de Zwart JA, Moonen CT. Magnetic resonance temperature imaging for guidance of thermotherapy. J Magn Reson Imaging 2000; 12:525-533.
17. McDannold NJ, Jolesz FA. Magnetic resonance image-guided thermal ablations. Top Magn Reson Imaging 2000; 11:191-202.
18. Germain D, Chevallier P, Laurent A, Saint-Jalmes H. MR monitoring of tumour thermal therapy. Magma 2001; 13:47-59.
19. De Poorter J. Noninvasive MRI thermometry with the proton resonance frequency method: study of susceptibility effects. Magn Reson Med 1995; 34:359-367.
20. Peters RD, Henkelman RM. Proton-resonance frequency shift MR thermometry is affected by changes in the electrical conductivity of tissue. Magn Reson Med 2000; 43:62-71.

Phase Unwrapping Improves Phase Shift-based Temperature Measurements with Magnetic Resonance Imaging

ABSTRACT

MR thermometry based on the water proton resonance frequency (PRF) shift phenomenon to monitor thermal ablative treatment is vulnerable to phase wrapping. Fast heating at high field MRI can result in phase differences that exceed π radians, which, if uncorrected for, will give rise to erroneous temperature estimates. We investigated whether application of phase unwrapping improved the accuracy of MRI-based temperature measurements.

We monitored temperature increase during radio-frequency ablation of muscle tissue using PRF based MR-thermometry at 3T in two orthogonal slices. Agreement between temperature measurements for pixels that were visible in both orientations was calculated, by using two conventional methods that are vulnerable to potential phase wrapping (raw subtraction, "running sum") and application of a phase unwrapping routine after raw subtraction .

Agreement in the presence of phase wraps was -6.7 °C±4.2 °C ($p<0.001$) for direct subtraction and -6.6 °C±4.2 °C ($p<0.001$) for the "running sum" method and 0.1 °C±5.1 °C for the novel method. Temperature measurements using the conventional calculation schemes were biased due to the presence of phase wraps ($p<0.001$). No such bias was found between temperature measurements after application of the phase unwrapping method ($p>0.624$).

Phase unwrapping improves PRF-based MR thermometry during heating in comparison with the conventional methods.

Suprijanto, MSc ✳
Mika W. Vogel, MSc ◆
Frans M. Vos, PhD ◆✳
Henri A. Vrooman, PhD ◆♥
Albert M. Vossepoel, PhD ✳
Peter M.T. Pattynama, PhD, MD ◆

From
◆ Departments of Radiology and
♥ Medical Informatics,
  Erasmus MC, University
  Medical Center Rotterdam,
  The Netherlands.
✳ The Department of
  Quantitative Imaging, Delft
  University of Technology,
  Technical University Delft,
  Delft, The Netherlands

INTRODUCTION

Radio-frequency (RF) ablation is a promising minimally invasive alternative to establish local control for some tumors. A key requirement for acceptance of the technique is reliable real-time monitoring of induced heating during treatment. For this purpose magnetic resonance imaging has been proposed to monitor the heat deposition and improve the efficiency of the treatment.

For accurate temperature measurements using magnetic resonance imaging, the water proton resonance frequency shift (PRF) method is preferred.[1,2] This method quantifies changes in phase ($\Delta\varphi$) to changes in temperature (ΔT) according to :

$$\Delta T = \frac{\Delta \varphi}{\omega \alpha \tau} \qquad [1]$$

Where ω is the resonance frequency, τ is the time for PRF sensitization and a is the temperature sensitivity constant. Because of quantification of phase changes, the method is sensitive to phase wrap (Figure 1). Phase wrap occurs when the absolute change in phase ($\Delta\varphi$) exceeds π, because, due to its cyclic nature, phase in the MR image can only have values from $-\pi$ to π. To overcome phase wrap, it is customary to calculate partial PRF shifts between subsequent phase images and integrate these from the starting image up to the most recent image, the so called "running sum" method.[3] This method, however, is equally vulnerable to phase wraps that occur between subsequent images. In addition, such error is propagated onto all consecutive images.

As an alternative method, we propose that phase wrap between subsequent images can be corrected for, or can be unwrapped, by using the phase information of neighboring pixels in the same geometrical MR image. If the phase were unwrapped using neighboring phase values before calculating the PRF shifts, we speculate that the stability in the overall temperature estimation will be increased, because phase wrap is corrected for and erroneous phase measurement do not propagate in the measurements over time.

We evaluated the use of a phase unwrapping routine to assist the PRF calculation, whereby it was of interest if additional phase unwrapping would result in more accurate MR thermometry, during RF ablation in *ex-vivo* muscle tissue.

MATERIALS AND METHODS

Experimental design

We performed thermal ablation in an *ex-vivo* chicken meat sample, while monitoring the temperature increase using PRF based MR-thermometry in two orthogonal imaging slices. We evaluated agreement (See *Statistical analysis*) between temperature measurements for three conditions. For the first condition, temperature measurements were calculated using quantification of phase shift

relative to the first acquired image only, which served as a reference image. For the second condition, temperature measurements were calculated using quantification of phase shift relative to the previously acquired image, which served as a 'floating' reference image. Total temperature change was determined by integration of all calculated partial temperature changes from the first image. For the third condition, we calculated temperature change, relative to the first "fixed" reference image, but only after applying the here proposed Flynn's phase unwrapping routine (see *Phase Unwrapping*).

MR imaging and image analysis

All MR images were acquired as complex data on a 3.0 T Signa VH scanner (General Electric, Milwaukee, Wisconsin, USA), with LX M3 software, 40mTm^{-1} gradients and a slew rate of 268 μs. Temperature sensitive images were acquired with a conventional fast spoiled gradient echo sequence (TR/TE/θ/BW=33/25/15°/31.25) in two orthogonal scan planes that intersected at the RF needle with 0.94 mm in-plane resolution and a slice thickness of 5 mm. We positioned an MRI compatible RF needle (Cool-Tip^{TM} RF-M, CTM-1530, Tyco Healthcare, Zaltbommel, The Netherlands; active tip 30 mm, 1.5 mm (17G) ⌀) in a chicken meat sample and performed ablation using an RF generator (Tyco Healthcare, Zaltbommel, The Netherlands; 0-200W with 50Ω load, 0.48 MHZ, max. current 2.0 A) at maximum power with impedance control for 5 minutes. During ablation and subsequent cooling, we alternately acquired axial and coronal images through the RF needle, at a rate of 7 images per minute. Interfering RF noise from the ablation device was suppressed using a lowpass filter matched for a range of impedances (50-70Ω) which was integrated in the RF cabling and grounded to the MRI Faraday's cage.

Images were transferred off-line to a workstation running Matlab (MathWorks; Natick, MA). From complex data, magnitude and phase images were calculated. The phase difference image represent local changes in frequency at time τ expressed as

$$\Delta \varphi = \arctan(\Delta \omega_{loc} \cdot \tau) \qquad [2]$$

where ω_{loc} is the local precession frequency, caused by temperature changes. Due to the arctan operator, a measured phase image has its value interval [-π,π] and phase values beyond this interval will be wrapped.

Temperature calculation methods
Direct complex subtraction

The direct complex subtraction phase shift map is calculated based on complex phase subtraction between the latest available nth image and the first baseline image as a fixed reference.

$$\Delta \varphi_n = \arctan((\Re_i \Re_0 + \Im i \Im_0) - j(\Re_i \Im_0 - \Re_0 \Im_i))$$
$$\equiv \arctan(S_i S_0^*) \tag{3}$$

The phase calculation after the multiplication with the complex conjugate of the baseline image (S_0^*) ensures the maximal dynamic range of $\pm\pi$ and is therefore theoretically to be preferred over subtraction after phase calculation of the individual images. This method assumes that total phase changes are always less than π. Direct complex subtraction is generally not performed because of potential phase wraps. As an alternative, phase shift can be calculated based on addition ("running sum"). The "running sum" method is generally performed because of its reduced sensitivity to phase wraps in comparison with the direct subtraction technique.

Running sum
The "running sum" phase shift map is calculated based on complex phase subtraction between the latest available n^{th} image and the preceding $(n-1)^{th}$ image (i.e. a floating baseline image), then added to the sum of all previous the phase shift map, resulting in the objective phase shift map ϕ.

$$\varphi_n = \sum_{i=1}^{n} \arctan(S_i S_{i-1}^*) \tag{4}$$

where S_i represents the complex valued pixel for which the phase for sample is to be calculated. S_{i-1}^* is the complex conjugate of S_{i-1}. This method is based on the assumption that phase changes between subsequent images are always less than $|\pi|$ (due to small incremental temperature changes). The calculated temperature data is reported as Method 2.

Phase unwrapping assisted direct subtraction
The "running sum" method will yield erroneous measurements whenever, due to rapid heating, the PRF change between two subsequent images exceeds π. Then, an erroneous temperature measurement is added and the error propagates in consecutive measurements. In order to compensate for such occurrences, we used the following formulation for phase shift :

$$\Delta \varphi_n = PU[\arctan(S_i S_0^*)] \tag{5}$$

When 2π phase discontinuities occur in a PRF map due to direct complex subtraction, phase unwrapping restores the appropriate phase shift in the instantaneous image, using the phase information of the neighboring pixels in the

same geometrical scan plane. Subsequently, the temperature map is determined by application of equation 1. This prevents the build up of errors due to propagation of invalid measurements (caused by phase wrapping). We assessed the use of a phase unwrapping with Flynn's minimum discontinuity phase unwrapping algorithm[4] (see *Phase Unwrapping*).

Phase Unwrapping
Phase unwrapping is essentially the process of recovering the integer value of multiple of 2π to be added to each pixel of the wrapped phase data in order to obtain the absolute phase (unwrapped phase). Phase unwrapping in the presence of noise is not trivial and generally requires dedicated algorithms.

Flynn's minimum discontinuity algorithm
Given an array of phase-wrapped data, Flynn's minimum discontinuity criterion is designed to minimize the error measure ε

$$\varepsilon = \sum_{i=0}^{n} h_i + \sum_{i=0}^{n} v_i \qquad [6]$$

where n is the number of pixels and h and v are dichotomous variables that indicate the presence of a phase jump at position i of horizontal and vertical transitions in a single MR image. Because the solution should be in accordance with the original data set, the error measure evaluates to

$$\varepsilon = \sum_{i=0}^{n} \left| \phi_{i+1} - \phi_i - \frac{\delta\phi_i}{\delta x} \right| + \sum_{i=0}^{n} \left| \phi_{i+xres} - \phi_i - \frac{\delta\phi_i}{\delta y} \right| \qquad [7]$$

where $\delta\phi_i$ are the partial derivatives at position i with regard to x and y, and xres is the number of elements per row. Because of the discrete nature of the jumps, the discontinuity measure is equal to the jump count. Flynn's algorithm employs a tree searching algorithm to trace contours of discontinuities. When enclosed regions are identified, integer multiples (the jump count) of 2π are added to reduce the number of discontinuities. The algorithm is guaranteed to converge and has the ability to receive additional input in the form of quality maps to weigh the phase information in the presence of noise. We used a quality map for phase unwrapping using the local variance of the derivatives of the magnitude data.[5] The larger the variance, the more likely it is that this region exhibits noise-like behavior.[6]

Statistical analysis
For comparison of the different temperature calculation methods we calculated agreement with temperature measurements at the same position in the orthogonal slice. We assessed agreement instead of product-moment calculations, because it provides an unbiased estimate of the accuracy of both temperature measurements.[7] We quantified agreement between the PRF based measurements from the axial and coronal planes for the three different methods. In the coronal plane, we manually

selected a region in which wraps were present, in a row of 4 adjacent pixels, at the intersection of both planes. To estimate the lower bound accuracy, we calculated agreement between the scan planes in a 2x2 region in which no phase wrap was observed. Agreement was defined as the mean of the differences between two measurements and the limits of agreement as the 95% confidence interval around the mean. All values are reported in degrees Celsius. Paired student t-tests were used to calculate significance of differences. Differences were deemed significant at the p=0.05 level.

RESULTS

RF heating showed a peak temperature change of almost 45 °C within 10 seconds. The fastest observed heating showed local temperature increases of over 15°C / second. Figure 1 shows the reconstructed magnitude and phase images before, during and after the heating process. The low-pass filter effectively filtered the noise of the RF generator, with only 7 dB loss in SNR.
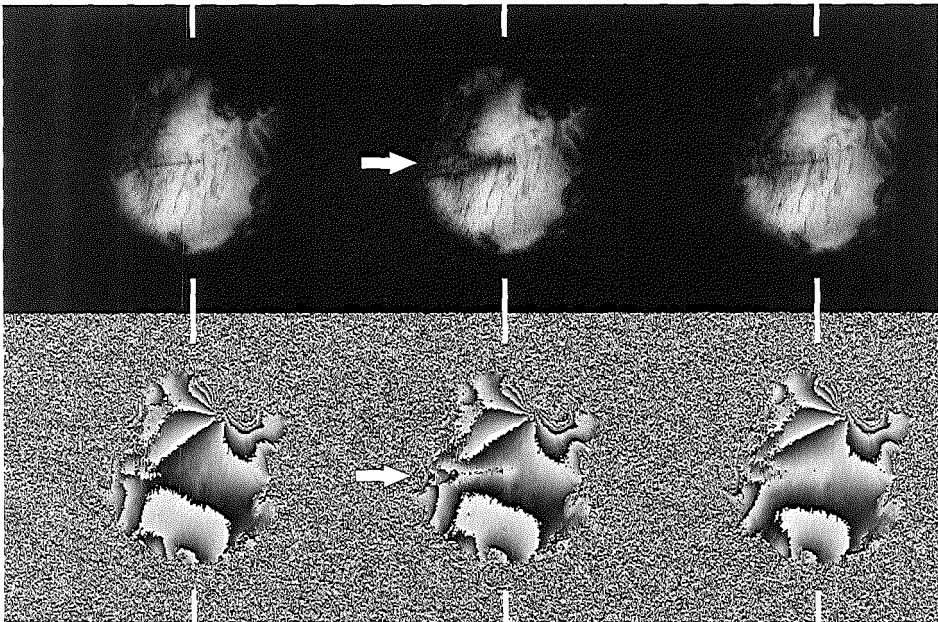
Figure 1. Coronal magnitude and phase images as acquired at different time points (at 14, 40 and 98 seconds) during the heating experiment. In the phase images (bottom row), phase wrap is visible as lines that separate wrapped phase (from π (white) to -π (black), or vice versa). Around the needle, thermal changes are visible (see arrows) as signal drop in the magnitude images and as a phase change in the phase images. The white ticks indicate the position of the perpendicular scan plane, that was used as temperature reference.

Figure 2.   Temperature maps during the experiment (left to right) for the three different conditions (top to bottom). Abrupt changes in the thermal profile are indicative of phase wraps. The top row shows the calculated thermal changes using direct subtraction. The middle row shows the calculated thermal changes using "running sum". And the bottom row shows thermal maps based on phase-unwrapping assisted subtraction. While the "running sum" method recovers most of the phase wrap errors that are present in the direct subtraction row, some errors remain (see arrows in the second column). Discontinuities in the calculated temperature using the "running sum" method are located close to the needle (arrows). Phase unwrapping removed these discontinuities. (A full color version of this illustration can be found in the color section).

The loss in signal intensity due to temperature-dependent T_1-lengthening was clearly visible around the RF needle (arrows, Figure 1). The thermal spot was clearly visible in both the axial (not shown) and coronal planes (Figure 1, second column).

From the region outside of the wrapping area, we calculated agreement between coronal and axial temperature measurements of -0.06 ($p=0.674$) and limits of agreement of -3.41 and 3.30 °C and represents the lower bound agreement of the setup. The agreement in the area that showed phase wraps was -6.7 °C±4.2 °C ($p<0.001$) for direct subtraction and -6.6 °C±4.2 °C ($p<0.001$) for the "running sum" method. After phase unwrapping assisted direct subtraction

we found an agreement of 0.1 °C±5.1 °C. (p=0.709). Figure 2 shows the overlaid temperature maps for the different methods. In the case of direct subtraction phase wrap around the needle occurs and is masked out (Figure 2, top). Using the "running sum" method these errors are largely corrected, although effects of phase wrap were still discernible in certain pixels (Figure 2, middle). Phase unwrapping was able to remove isolated wrapped areas in the heat profile (Figure 2, bottom). These results (see Table 1) show that only in the case of phase-unwrapped phase good agreement was found between the two orthogonal measurements. The conventional methods suffered from residual phase wraps in the PRF measurements.

Table 1. Differences between measurements in the two orthogonal planes for regions without phase wraps and a region near the RF-needle where phase wraps occurred due to rapid heating. Phase unwrapping removed bias due to phase wraps.

Method	Mean difference (orthogonal measurements)	
	No phase wrap (°C)	Phase wrap (°C)
Direct subtraction	-0.06	-6.70
Running sum subtraction	-0.06	-6.71
Phase unwrapping after direct subtraction	-0.06	0.10
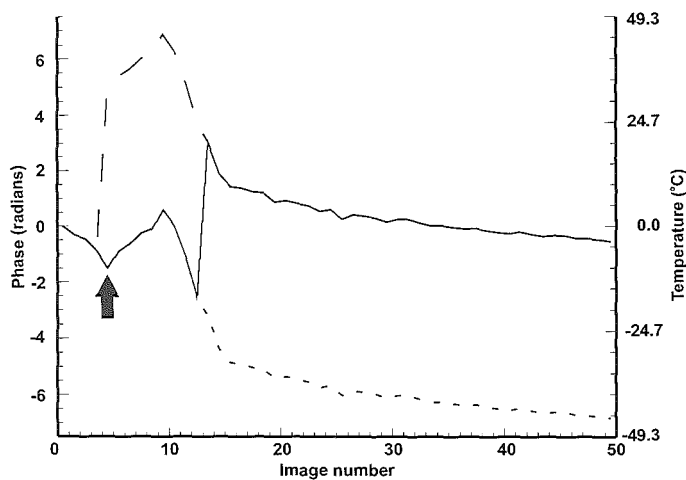
Figure 3. The phase evolution for a single pixel near the RF needle tip is shown over the duration of the experiment. This pixel experienced rapid heating (arrow), which resulted in incorrect temperature calculation, due to phase wrap, using either the direct subtraction (line) or "running sum" (dot) method. After phase unwrapping the thermal profile was restored. Note the error propagation that results from the "running sum" method, which is absent when either the direct subtraction or phase unwrapping method is used.
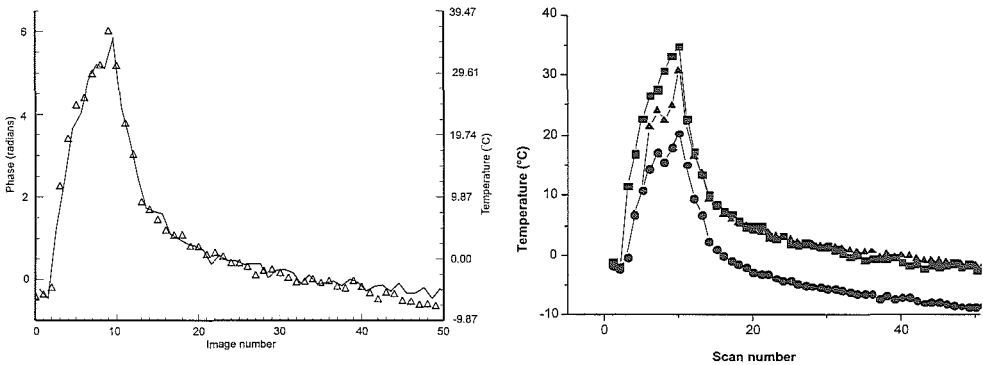
Figure 4. In the left graph, the phase unwrapped temperature profile of a single pixel versus image number is shown for both the coronal (triangles) and axial plane (line). To the right the temperature profile from a four pixel region near the RF needle is shown for the axial plane (squares) and the coronal plane using either the "running sum" (circles) or phase unwrapping (triangles) method. Again the influence of wrapped phase is visible in the calculated temperatures. Note again the incorrect temperature of -10°C at the end of the experiment for the "running sum method".

The effect of the three different methods on a single pixel is graphically depicted in figure 3. It can be appreciated that the irregularities in the temperature profile disappear after application of the phase unwrapping assisted method. Comparison with temperature data acquired in the perpendicular plane shows similar heat profiles (Figure 4) for the phase unwrapping assisted method, but not for the "running sum" method. This indicates that phase wrapping due to rapid heating can invalidate the "running sum" method. These errors can be corrected by application of phase unwrapping in combination with direct subtraction.

Discussion

The results in the present study show that phase unwrapping techniques can help guard the consistency in the PRF based temperature measurements. In some pixels, rapid RF heating caused a more than 15.5°C temperature rise between images. This exceed a π radians difference, causing both direct subtraction and the "running sum" method to fail, if phase wrapping was not accounted for. In the "running sum" approach the introduced error propagated in the subsequent calculated temperatures and consequently data obtained from these measurements did not agree with the reference thermometric data. Phase unwrapping, after direct subtraction of the images, corrected the aliased measurements and restored thermal accuracy.

Phase unwrapping becomes important when performing PRF-based MR thermometry at high field and at longer echo times, when signal to noise is critical. Increased noise levels can easily cause phase wraps by "tipping" the phase over the π boundary. Temperature dependent T_1-lengthening reduces the useful SNR

for PRF-based MR thermometry using fast spoiled gradient echo imaging. In addition, many current MR compatible RF needles have characteristics that influence PRF-based thermometry. Even though these needles are made from MR-compatible materials such as titanium or nitinol, the used alloys give rise to susceptibility differences in tissue that lead to reduced T_2^* around such needles.[8] This typically results in reduced SNR for PRF-based measurements, and potentially induced phase wraps.

The proposed phase unwrapping requires only processing of the direct subtraction images and is readily implemented and the computational burden is limited with conventional computer hardware. Alternatively, one can try to minimize the possibility of observing a phase wrap using the "running sum" method. The RF current could be limited to achieve slower tissue heating. In practice, one should use Flynn's phase unwrapping algorithm to assist the running sum method, because typically less phase contours are found. The algorithm thus performs faster, which is desired for the goal of real-time MR thermometry.

In summary, we have shown increased reliability of PRF based thermometry using phase unwrapping. The robustness of the technique allows reliable monitoring of rapid heating at high field. In addition, the proposed algorithm is readily applied to other areas in MR where correct phase information is necessary. For instance, for phase contrast velocity measurements and for calculation of magnetic field maps,[9] such as those typically acquired for calculating (high order) shim compensation over a region of interest.

REFERENCES

1. Germain D, Chevallier P, Laurent A, Saint-Jalmes H. MR monitoring of tumour thermal therapy. Magma 2001; 13:47-59.
2. Ishihara Y, Calderon A, Watanabe H, Okamoto K, Suzuki Y, Kuroda K. A precise and fast temperature mapping using water proton chemical shift. Magn Reson Med 1995; 34:814-823.
3. Chung AH, Hynynen K, Colucci V, Oshio K, Cline HE, Jolesz FA. Optimization of spoiled gradient-echo phase imaging for in vivo localization of a focused ultrasound beam. Magn Reson Med 1996; 36:745-752.
4. Ghiglia DC, Pritt MD. Two-dimensional Phase Unwrapping: Theory, Algorithms, and Software. New York: John Wiley and Sons, Inc., 1998.
5. Suprijanto, Vos FM, Vogel MW, Vossepoel AM, Vrooman HM. Additional Processing for Phase Unwrapping of Magnetic Resonance Thermometry Imaging. In Sonka M, Fitzpatrick JM, eds. Proc. SPIE. San Diego, CA, USA: Springer Verlag, Berlin, 2001, 2002. pp. 4684.
6. de Zwart JA, van Gelderen P, Kelly DJ, Moonen CT. Fast magnetic-resonance temperature imaging. J Magn Reson B 1996; 112:86-90.
7. Bland JM, Altman DG. Statistical methods for assessing agreement between two methods of clinical measurement. Lancet 1986; 1:307-310.

8. Aube C, Schmidt D, Brieger J, et al. Magnetic resonance imaging characteristics of six radiofrequency electrodes in a phantom study. J Vasc Interv Radiol 2004; 15:385-392.
9. Cline, H. E., S. Ludke, et al. (2003). B_0 Maps using Three-Dimensional Phase Imaging. ISMRM, Toronto, ON, CA.

A Precious Metal Alloy Needle for Improved Magnetic Resonance Thermometry of Interstitial Radiofrequency Heating

Chapter 4

ABSTRACT

Radiofrequency (RF) induced ablation allows local destruction of tumor tissue, and is becoming an increasingly popular way of doing minimal invasive thermal treatment. Because such thermal lesions are fairly unpredictable, monitoring the therapeutic intervention by magnetic resonance (MR) thermometry increases the confidence of treatment outcome.

Current MR-compatible radiofrequency needles show susceptibility artifacts around the needle. This limits their use for MR thermometry.

In this work we compared standard MR compatible RF needles versus needles, based on an alloy of tissue mimicking susceptibility, previously described for the use of vascular stents. We evaluated the use of this alloy which reduced MR thermometry artifacts. We characterized and quantified the artifacts due to magnetic field disturbance of both this alloy needles and standard MR compatible needles. In addition, we assessed thermometric fidelity, between our alloy and standard RF needles in phantoms.

Thermal accuracy is affected by the susceptibility of the used RF needle. The results show that artifacts are much reduced using alloy needles, and that it is feasible to monitor temperature changes using the PRF method over the complete relevant therapeutic range.

Mika W. Vogel, MSc ◆
Lucas C. Van Dijk, PhD, MD ◆
Jan-Willem Kuiper, MD ◆
Herman J. Flick, MSc ▲
Peter M.T. Pattynama, PhD, MD ◆

From
◆ Department of Radiology, Erasmus MC, University Medical Center Rotterdam, The Netherlands.
▲ General Electric Medical Systems Europe, Buc, France.

INTRODUCTION

Percutaneous radiofrequency (RF) ablation is a new technique for minimally invasive local treatment of tumors, especially in the liver.[1-2] An RF needle inserted into the tumor will heat up and coagulate the tumor tissue at temperatures >60°C by the "microwave oven effect". It is desirable to monitor the thermal treatment in real-time: too little heat distribution around the RF needle will result in incomplete treatment of the tumor, and too much in unnecessary destruction of healthy tissue surrounding the tumor. Also, too high tissue temperatures will cause vaporization and carbonization effects which will reduce the effectiveness of the ablation treatment.[3]

An attractive method for real-time monitoring is magnetic resonance (MR) thermometry based on quantifying the proton resonance frequency (PRF) shift,[4,5] which provides precise and accurate thermal maps of the region of interest. But performing PRF-based MR thermometry during RF ablation is not trivial. Standard RF needles are made of superparamagnetic stainless steel that cannot be readily used in the MR environment. Several manufacturers have now marketed MR compatible MR needles made of, for example, titanium alloys. But even the commercially available RF needles designed for MR compatibility (the ones that we are aware of) still have magnetic susceptibility considerably different from that of tissue. Resulting MR imaging artifacts limit the visibility of the needle during MR imaging and the accuracy of MR thermometry.

We reasoned that an RF needle constructed of material that would be more MR compatible would improve MR imaging and MR thermometry, and thus, would be better suited for performing RF ablation and monitoring in an MR environment. Potentially, such a material could be the metal alloy ABI, which has mechanical properties similar to that of stainless steel and a magnetic susceptibility that is better matched to liver tissue than the commercially used MR compatible needles. We have previously described the use of ABI-alloy in the construction of MR compatible vascular stents.[6]

Here, we wish to describe our initial experimental experience with RF needles constructed of ABI-alloy. We compared the ABI-needles to commercially available MR compatible RF needles, with regard to imaging artifacts at MR imaging and resultant accuracy of MR thermometry around the needle tip.

MATERIALS AND METHODS

RF needles

We constructed two RF-needles made of ABI, of 0.3 mm (23.5G) and 2.0 mm (12G) diameter, respectively. ABI is a bio-compatible, iron- and nickel-free precious metal alloy that mainly consists of palladium and silver (Elephant Dental BV, Hoorn, The Netherlands). Its mechanical properties are similar to those of stainless steel, with elasticity of 1.1×10^5 N/mm^2, elongation of 30%, and hardness of 220 Hv. For comparison, we used two commercially available MRI compatible

RF needles, whereby it was of interest to compare the size-matched needles with regard to the relevant artifacts around the needle tip :

1) an RF needle 1.5 mm in diameter (Cool-Tip™ RF-M, CTM-1530, Radionics, Burlington, MA); and
2) an RF needle with expandable metal hooks of 0.2 mm in diameter (Starburst, RITA medical systems, Mountain View, CA)

Magnetic susceptibility induced needle artifacts
An RF needle will cause local magnetic field distortion, the magnitude of which will depend on the magnetic susceptibility difference relative to its environment, needle shape, and needle volume. Three phenomena will hamper MR imaging and MR thermometry:

1) signal loss due to intravoxel dephasing,[7] because of phase dispersion of the transverse magnetization within a voxel. This will lead to T_2* shortening and subsequent loss of SNR around the RF-needle. Consequenyly, this will lead to lower optimal PRF sensitization times,[8] and thus lower thermal accuracy using PRF-based MR thermometry.
2) distortion of MR images, because of superposition of local magnetic fields onto the imaging gradients. This is relevant especially in fast multiple echo gradient echo (FSPGR) sequences such as PRESTO,[8] spiral[9] or EPI.[10] sequences favored in MR thermometry. This effect becomes problematic when mapping the thermal changes to the correct anatomy.
3) Suboptimal spectral suppression of fat. This will limit the accuracy of PRF-based MR thermometry, because the presence of unsuppressed fat within a voxel will change the temperature sensitivity constant.[11]

Assessment of artifacts, and accuracy of MR thermometry
First, we compared the four RF needles with respect to magnetic susceptibility induced artifacts on the MR magnitude and phase images. We quantified the changes in magnetic field and T_2* changes near the RF needles by using FSPGR images with multiple echo times (TE=10..21 ms, 1 ms increment, θ/TR/BW/FOV = 10°/60/15.6/12). The needles were placed in a syringe filled with gel (5% agar, 0.1mmol CuSO4, T_2*/T_1 = 33.2 / 158.3 ms, measured at 1.5T), vertically oriented in the MR scanner, which is similar orientation as during actual *in-vivo* ablation of the liver.

Then, we compared the RF needles with respect to the effect of the susceptibility artifacts on the resultant accuracy of MR-based thermometry near the needle tip. We acquired 100 consecutive images from the four needles simultaneously at ambient temperature using a multiple echo FSPGR sequence (TE=4.6 .. 42.0 ms, 4.3 ms increment, θ/TR/BW/FOV = 10°/80/15.6/24) for both parallel and perpendicular orientations with regard to the main magnetic field.

Next, we positioned the needle in a gel (2.5% gelatin with 0.1mmol CuSO4, T_2^*/T_1 = 56.1 / 168.7 ms measured at 1.5T) together with a fiberoptic thermometer (Luxtron 740, Luxtron Corporation, Santa Clara, CA; accuracy 0.2°C) as a gold standard. The gel was uniformly heated to 60°C and slowly cooled down in an insulating Styrofoam box. During cooling, MR images were continuously obtained with a single echo FSPGR sequence with θ/TE/TR/BW/FOV = 10°/20/30.5/15.6/12. Additionally, we compared the fat suppression with an spectral inversion technique for each of the needles in a meat sample. We acquired a 3D volume both with and without fat-suppression FSPGR (θ/TR/BW/FOV = 20°/18.4/15.6/16) with 2.0 mm slice thickness.

Finally, we assessed the quality of MR imaging and MR thermometry when using the four RF needles during actual RF ablation in *ex-vivo* chicken muscle. The Luxtron thermometry fiber was positioned in close proximity to the needle tip. We continuously acquired 100 images, using a 3D FSPGR sequence (θ/TE/TR/BW/FOV = 10°/10/16.3/15.6/18) using a 3" surface coil during RF ablation (20W for 4 minutes) and the subsequent 10 minutes-period of cooling-down. MR imaging was done in the coronal and sagittal scan planes. The different needles differed with respect to SNR around the needle tip, and we therefore compared MR thermometry measurements obtained at similar SNR of 40 in the region of interest around the RF needle tip. Images were transferred off-line, and a comparison was made between all needles with regard to mean temperature deviation and absolute errors, relative to the gold standard.

MR imaging and image analysis

MR images were acquired as complex data on a 1.5T scanner (Signa CV/i , General Electric, Milwaukee, WI) with LX 9.1 software, $40 mTm^{-1}$ gradient strength and $150 mTm^{-1}$ slew rate. Images were transferred off-line to a workstation running IDL 5.4 (Research Systems Inc; Boulder, CO). Because of the increased noise levels in the presence of the commercially available MR compatible needles, we applied phase unwrapping algorithms on the resultant MR phase images by using Flynn's minimum discontinuity method.[12] Regression analysis was performed by applying the least absolute deviates-method.[13]

RF ablation

RF ablation was done by using an RF generator (Tyco Healthcare, Zaltbommel, The Netherlands; 0-200W with 50Ω load, 0.48 MHz, max. current 2.0 A) connected to the RF needle by means of an MR compatible connection cable set (CCS-MR, 8 meter) and a grounding pad (DGP-HP, Tyco Healthcare). A custom-made low-pass filter suppressed interfering harmonic frequencies using double impedance tuning. The connection cable was cut and the filter was placed in series with the cable, and grounded to the MRI's Faraday cage, using a copper plate, effectively creating an RF penetration panel.

RESULTS

Assessment of artifacts, and accuracy of MR thermometry

Artifacts on MR images are shown in Figure 1. It can be readily appreciated that the large 2-mm-diameter ABI needle, even though it was 100 times more voluminous than the thin 0.2 mm-diameter commercially available MR compatible Starburst needle, caused less artifacts (Figure 1, B versus D).
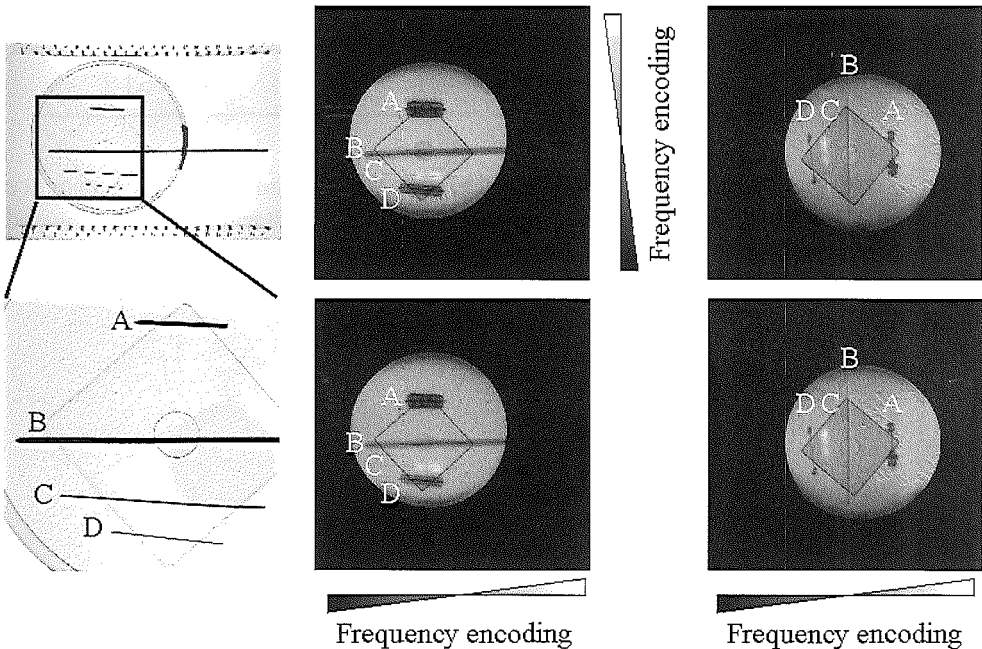

Frequency encoding   Frequency encoding

Figure 1. RF needle artifacts on fast spoiled gradient echo images for the Cool-Tip (**A**),ABI (**B,C**) and Starburst (**D**) needles, for different orientations relative to themain magnetic field. It can be appreciated that in the parallel orientation (left), signal loss at the tip prevents accurate localization and insufficient SNR foraccurate MR thermometry.

Table 1 lists the results of the quantitative measurements of reduction in T_2^*, and the distortion of the magnetic field, expressed as the furthest distance from the needle, at which these artifacts could be demonstrated. It can be seen, for example, that the commercially available 1.5-mm-diameter Cool-Tip needle showed reduced T_2^* in the entire area within 7 mm from the center of the needle ($p<0.007$; Figure 1, A; see also Figure 2). Also, T_2^* could not be reliably calculated within 2 mm distance of the center of the needle.

Table 1.

Needle	Gel T_2^* effect	Gel cooling (SEE)	Chicken (heating SEE)
CoolTip	up to 7 mm	0.59 °C (r^2=0.991)	4.7 ± 4.2 °C
ABI (2.0 mm)	up to 4 mm	0.63 °C (r^2=0.993)	2.2 ± 0.2 °C
Starburst	up to 3 mm	1.01 °C (r^2=0.988)	1.5 ± 0.1 °C
ABI (0.3 mm)	none observed	0.96 °C (r^2=0.976)	0.9 ± 0.1 °C

By contrast, the 2-mm diameter ABI needle showed reduced T_2^* up to a distance of 4 mm (p<0.001). The 0.2-mm-diameter hooks of the Starburst needle caused T_2^* reduction up to 3 mm distance (p<0.001). By contrast, no T_2^* effects were seen in the 0.3mm-diameter ABI needle (p=0.471).
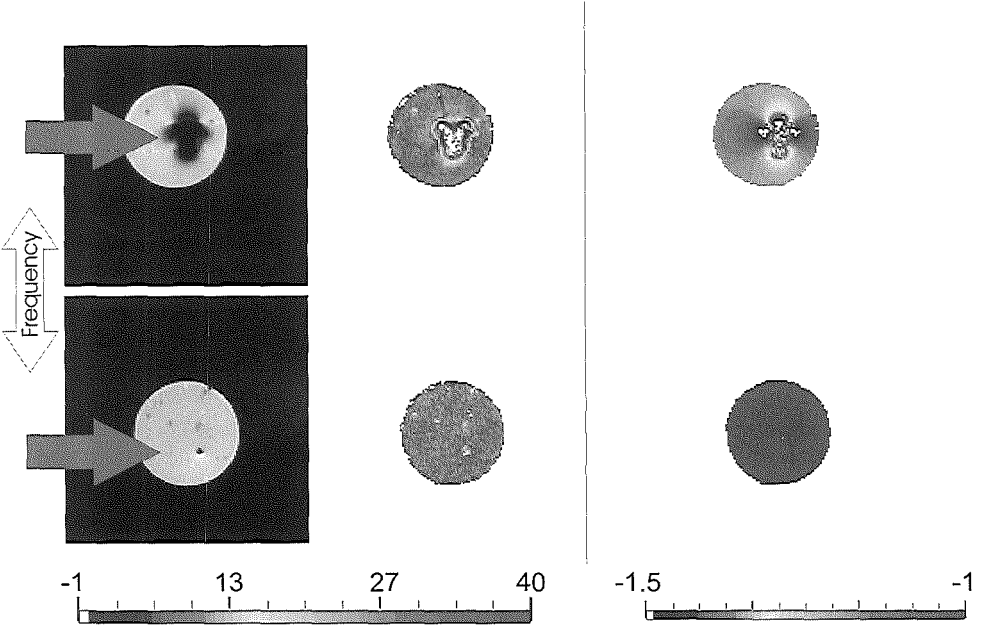
Figure 2. Best and worst cases of the RF needle artifacts. Magnitude images are shown left for the Cool-Tip needle (top) and small ABI needle (bottom). In the center column, T_2^* maps (ms) are shown, in which the magnetic field inhomogeneity around the Cool-Tip needle is clearly visible. To the right, magnetic field deviation maps (ppm) are shown. Little effect is seen around the ABI needle. (A full color version of this illustration can be found in the color section).

Local magnetic field distortion was seen around the 1.5-mm-diameter Cool-Tip RF needle up to a distance of 9 mm (p=0.091) for as much as 0.46 ppm at 4 mm. The 2-mm-thick ABI needle showed minimal field disturbance of 0.01 ppm up to 3 mm. The maximal field disturbance around the 0.2-mm-diameter Starburst needle was 0.05 ppm and returned to normal at 3 mm. Even smaller field disturbance was seen around the 0.3-mm-thin ABI needle, for a maximum of 0.03 ppm. No field effects were seen beyond 1mm distance from the ABI-needle (p=0.249). These results show that the commercially available MR compatible RF needles show more magnetic susceptibility artifacts that the ABI-needles of similar size.

Figure 3 shows the thermal accuracy of the temperature measurements in the gel at ambient temperature versus echo time for the four needles. It can be appreciated that the variance of the measurements are lower for the ABI needles that for the MR-compatible RF needles.

Figure 3. PRF standard deviation quantified to temperature error for different echo times for both
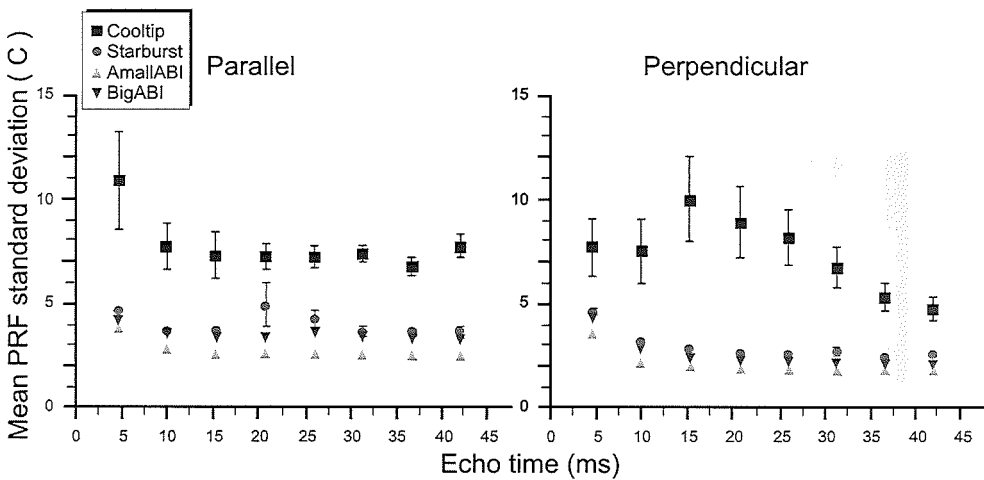
parallel and perpendicular orientation to the main magnetic field. The large susceptibility effect of the Cooltip needle prevents accurate temperature quantification near the needle. For both the Starburst and the ABI needles is good quantification possible. Even though the 2-mm-diameter ABI needle is 100x more voluminous, it performs slightly better than the Starburst needle.

Table 1 shows the correlation coefficients and SEE of the regression lines of the PRF shift versus temperature during gel cooling. In the gel phantom, excellent correlation with small residual SEE was found for all needles (when precautions had been taken to measure at similar SNR of 40). When compared with the measurements obtained in a gel without any needle present, we found that the large 1.5-mm-diameter commercially available Cool-Tip RF needle caused a large deviation in the temperature coefficient of 22% (Figure 4).
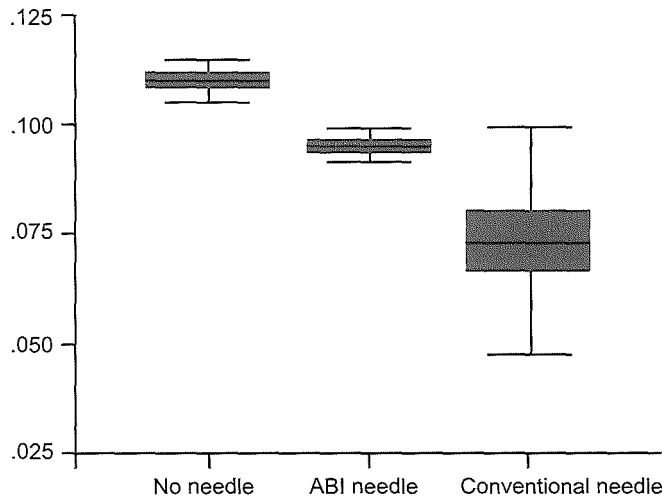
Figure 4. Temperature sensitivity constants measured without needle present (left), with ABI needle present (middle), or with a conventional needle present (right).
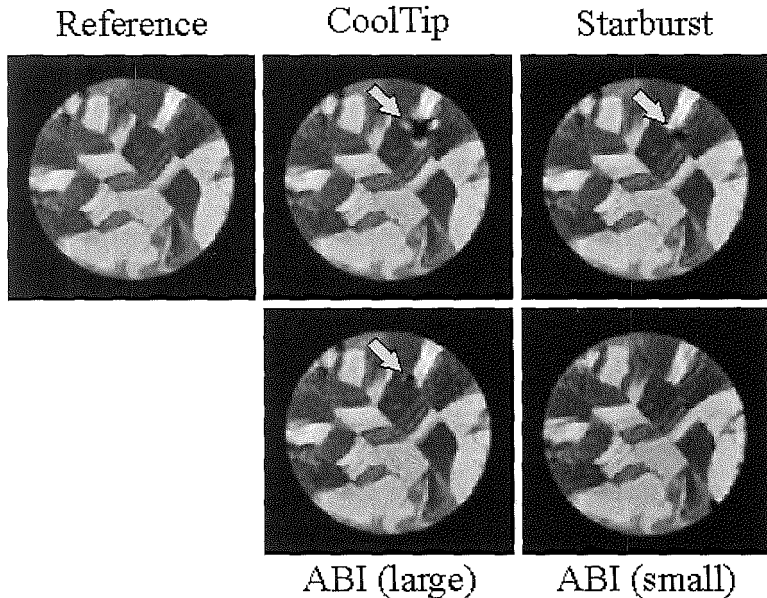
Figure 5. Fat suppression artifacts in a meat sample. The arrows indicate the position of fat suppression artifacts for the CoolTip, which are vastly reduced with the 2-mm-diameter ABI needle. No observable artifact is present near both the 0.3-mm-diameter ABI needle and the Starburst needle.

Much reduced deviations in the calculated temperature coefficient were seen for the three other needles (< 10%).

Spectral fat saturation showed artifacts with the used CoolTip RF needle (Figure 5). This artifact was much reduced, but still noticeable when using the 2-mm-diameter ABI needle. In the presence of both the Starburst and the 0.3-mm-diameter ABI needle, no fat saturation artifacts were observed.

Active RF ablation in the muscle tissue resulted in a temperature rise to at least 50°C within 4 minutes in all four needles, and it proved well feasible to image the temperature evolution during the RF ablation (Figure 6).
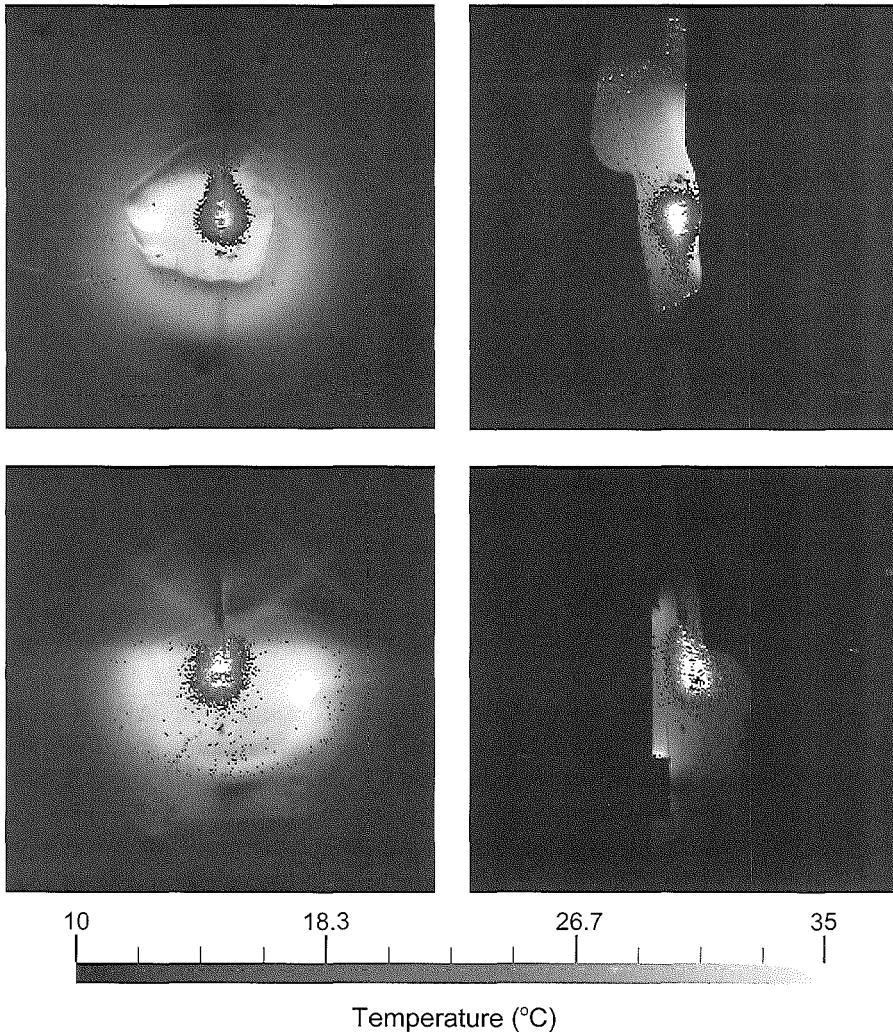
Temperature (°C)

Figure 6. RF heating around small tip ABI needle (top) and Cool-Tip needle (bottom),the temperature profile is much distorted at the needle tip for the Cool-Tip needle, as could be expected from the magnitude images in Figure 1. No such effect is appreciable around the ABI needle. (A full color version of this illustration can be found in the color section).

Good correlation with the gold standard was seen, which was slightly better in the ABI needles. More favorable, smaller SEE was found in the ABI-needles in comparison to the commercially available RF needles of similar size.

DISCUSSION

Suppression of electronic interference from the RF generator, allows the use of MRI to guide and monitor the radiofrequency ablation. Using PRF based MR thermometry it is possible to obtain quantitative temperature maps from the RF power deposition. During ablation in an *ex-vivo* chicken breast specimen, we were able to quantify temperature up to and beyond the clinical therapeutic threshold of 65°C.

However, currently-used needles may exhibit sub-optimal properties for reliable monitoring using the PRF method. The worst case in our experiments showed spatially dependent field disturbances up to 0.46 ppm, significant T_2* shortening and a rather poorly defined temperature constant. Consequently, temperature quantification within approximately one centimeter from the tip appears problematic, as temperature uncertainty almost doubled in our experiment.

We have shown that use of the ABI alloy with a tissue mimicking susceptibility reduces T_2* decay. In addition, we find a much more narrowly defined temperature constant and only limited field disturbances in our setup. In the RF heating experiment, we did not find significant differences in measurements near the needle and near the needle tip. Therefore we feel that the ABI needle allows more reliable monitoring of the temperature effects during RF ablation. The difference in results between the 0.3-mm-diameter ABI and Starburst needle will in practice probably not result in a noticeable improvement in PRF monitoring of ablation, as other factors will limit the achievable accuracy of *in-vivo* measurements.

The radio-opacity and tissue mimicking susceptibility of ABI potentially complicate the targeting procedure. Several approaches could be followed to increase the conspicuity of the needle. Using an catheter introduction set (as currently used for interstitial laser coagulation) or MR active tracking approaches[14] precise targeting could be accomplished. Alternatively, application of a small current will induce sufficient signal loss to be able to locate the needle in the MR images.

In summary, we have demonstrated the feasibility of using of an susceptibility matched RF needle using the ABI alloy.

REFERENCES

1. Kettenbach J, Kostler W, Rucklinger E, et al. Percutaneous saline-enhanced radiofrequency ablation of unresectable hepatic tumors: initial experience in 26patients. AJR Am J Roentgenol 2003; 180:1537-1545.
2. Fontana RJ, Hamidullah H, Nghiem H, et al. Percutaneous radiofrequency thermalablation of hepatocellular carcinoma: a safe and effective bridge to livertransplantation. Liver Transpl 2002; 8:1165-1174.
3. Goldberg SN, Gazelle GS, Halpern EF, Rittman WJ, Mueller PR, Rosenthal DI.Radiofrequency tissue ablation: importance of local temperature along the electrode tipexposure in determining lesion shape and size. Acad Radiol 1996; 3:212-218.
4. De Poorter J, De Wagter C, De Deene Y, Thomsen C, Ståhlberg F, Achten E.Noninvasive MRI thermometry with the proton resonance frequency (PRF) method: invivo results in human muscle. Magn Reson Med 1995; 33:74-81.
5. Ishihara Y, Calderon A, Watanabe H, Okamoto K, Suzuki Y, Kuroda K. A precise andfast temperature mapping using water proton chemical shift. Magn Reson Med 1995;34:814-823.
6. van Dijk LC, van Holten J, van Dijk BP, Matheijssen NA, Pattynama PM. A preciousmetal alloy for construction of MR imaging-compatible balloon-expandable vascularstents. Radiology 2001; 219:284-287.
7. Bos C, Viergever MA, Bakker CJ. On the artifact of a subvoxel susceptibility deviationin spoiled gradient-echo imaging. Magn Reson Med 2003; 50:400-404.
8. de Zwart JA, van Gelderen P, Kelly DJ, Moonen CT. Fast magnetic-resonancetemperature imaging. J Magn Reson B 1996; 112:86-90.
9. Stafford RJ, Hazle JD, Glover GH. Monitoring of high-intensity focused ultrasoundinducedtemperature changes in vitro using an interleaved spiral acquisition. MagnReson Med 2000; 43:909-912.
10. Weidensteiner C, Quesson B, Caire-Gana B, et al. Real-time MR temperature mappingof rabbit liver in vivo during thermal ablation. Magn Reson Med 2003; 50:322-330.
11. de Zwart JA, Vimeux FC, Delalande C, Canioni P, Moonen CT. Fast lipid-suppressedMR temperature mapping with echo-shifted gradient- echo imaging and spectralspatialexcitation. Magn Reson Med 1999; 42:53-59.
12. Ghiglia DC, Pritt MD. Two-dimensional Phase Unwrapping: Theory, Algorithms, and Software. New York: John Wiley and Sons, Inc., 1998.
13. Press WH, Teukolsky SA, Vetterling WT, Flannery BP. Numerical Recipes in C. Cambridge: Cambridge University Press, 1992. pp. 704-705.
14. Dumoulin CL, Souza SP, Darrow RD. Real-time position monitoring of invasivedevices using magnetic resonance. Magn Reson Med 1993; 29:411-415.

68

Use of Fast Spin Echo for Phase Shift Magnetic Resonance Thermometry

ABSTRACT

A modified Fast Spin Echo magnetic resonance imaging sequence (FSE) is proposed for MR thermometry, employing the proton resonance frequency shift (PRF) by means of MR phase maps. Despite their obvious advantages of speed and high Signal-to-Noise Ratio (SNR), FSE sequences have not until now been used for this purpose due to the restraints imposed by the Carr-Purcell-Meiboom-Gill (CPMG) conditions.

The new FSE combines a new phase modulation scheme that maintains magnetisation that ordinarily is destroyed under CPMG conditions, while employing conventional FSE gradient waveforms. The echoes are read in a single shot using 128 readouts in 650 ms, with a phase sensitive preparation using an optional time shift τ before the start of the refocusing gradient waveforms. This feature allows the quantification of temperature dependent phase shifts. We tested the sequence by imaging a heated agar gel phantom while cooling, using different values for τ.

There was good correlation between FSE and fiberoptic-based temperature measurements in the phantom($r^2 \geq 0.95$). Temperature sensitivity could be adjusted by varying the τ value.

With the proposed non-CPMG FSE sequence it is feasible to quantify temperature changes by means of the PRF shift.

Mika W. Vogel, MSc ◆
Peter M.T. Pattynama, PhD, MD ◆
Franck L. Lethimonnier, PhD ◆ ▲
Patrick Le Roux, MSc ▲

From
◆ Department of Radiology, Erasmus MC, University Medical Center Rotterdam, The Netherlands.
▲ General Electric Medical Systems Europe, Buc, France.

INTRODUCTION

Thermometry is important for monitoring minimally invasive treatment with thermal therapy. Several approaches can be undertaken, but magnetic resonance (MR) thermometry is generally favored because of its excellent soft tissue contrast, thermal sensitivity and the utility of MR for guidance of the thermal applicator.

Currently, the most accurate MR thermometric methods employ the water proton resonance frequency (PRF) shift using MR phase maps.[1-4] All current PRF-based approaches employ fast gradient echo sequences, usually on high field MR scanners (≥ 1.5T).

It would be advantageous if a pulse sequence could be used for PRF-based MR thermometry, that generated high signal to noise ratio (SNR) at the lower field strengths, typically used for interventional MR scanners. It has been shown that one can use spin echo sequences, for PRF quantification.[5] The classical spin echo (SE) acquisition schemes, however, render the technique too slow for clinical use. It would thus be reasonable to explore the use of the more time-efficient Fast Spin Echo (FSE) sequence to overcome this problem. So far, however phase sensitive preparation of FSE has been hampered because the Carr-Purcell-Meiboom-Gill (CPMG) condition in FSE effectively destroys magnetization perpendicular to the axis of the refocusing pulses in order to reach a steady state with imperfect π pulses.[6] This has dramatic consequences, and precludes CPMG FSE from use in certain types of imaging: specifically any procedures that rely on induced phase encoding (flow, chemical shift, diffusion). Crushing schemes[7,8] have been proposed to preserve the phase sensitive preparation, but reduce the available signal by about one half and appear therefore less competitive, especially when imaging a volume.

In this study we have assessed the capability of a modified FSE sequence,[9-10] to generate phase maps in which the PRF phenomenon is present. In addition, we performed MR thermometry based on these phase maps, and assessed the sensitivity of the new sequence.

MATERIAL AND METHODS
non-CPMG FSE sequence

The sequence used in this work is depicted in Figure 1. The non-CPMG train of echoes is at the right of the reference time, or "echo 0" point on the time axis. As can be verified in the figure there is no apparent difference in gradient waveforms between the current non-CPMG sequence and the conventional CPMG sequence. The only differences consist of a carrier phase change for each of the refocusing pulses and the introduction of sensitization time τ.

If the carrier phase values φ_1, φ_2, . . ., φ_n are chosen appropriately, the echotrain is stable and produces a high amplitude signal, even when the original transverse

magnetization, at "echo 0", is perpendicular to the refocusing axis. The choice of the transmission phases φ_1, φ_2,. . ., φ_n and the setting of the receiver phase for each echo sampling used in the current non-CPMG FSE sequence is beyond the scope of this article and has been described in detail previously.[9]
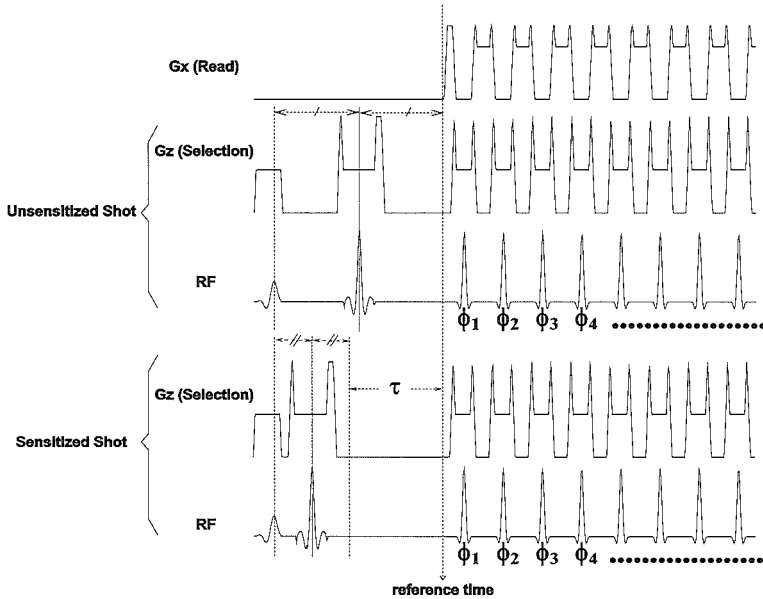

Figure 1. Depiction of the non-CPMG sequence used in this work. The non-CPMG train, at the right of the reference time, is very similar with the standard CPMG FSE sequence. The only difference lies in a change of carrier phase $\varphi 1,\varphi 2$.. for each of the refocusing pulse. When chosen appropriately this phase modulation produces a spin-echo signal with a large amplitude, whatever the initial phase of the magnetization is at the reference time. This property allows the insertion of a preparation sequence between the excitation pulse and the spin-echo train, even when this preparation results in a phase variation of the magnetization at the reference time. That is what is done here, at least for the particular sequence denoted 'sensitized shot', where during the time τ the chemical shift (or the main magnetic field inhomogeneity) influences the phase of the magnetization.

The theoretical basis of the work underlying the sequence has also been detailed previously.[10] The insensitivity of signal amplitude with regard to the initial magnetization phase permits the insertion of any contrast preparation or sensitization event in the time period between the excitation pulse and the reference time, even if this sensitization results in a phase variation of the transverse magnetization. In this study we inserted a free evolution period during which the water proton resonance frequency shift is transformed into a phase variation. To reduce the influence of the inhomogeneity during the excitation pulse rephasing, an initial π pulse was inserted in the preparation period. Each measurement is composed of at least two shots; in the first shot (the unsensitized

shot in Figure 1), the first π pulse is positioned such that there is no phase change due to the water proton resonance frequency shift at the reference time. In a second shot, the sensitized shot, the first π pulse block is shifted so that the time of the first magnetization refocusing is positioned at a time τ, away from the reference time. In practice, the reconstruction of a non-CPMG sequence is special[10] and necessitates the calibration of a 'receiver' phase φ_r. This is the role of the calibration shot, which would normally only be played once at the start of the experiment (there is no reason for the phase φ_r to evolve in time if the geometrical position of the slices is kept constant). In order to simplify the programming, and also to allow slice position variations without having to rely on a problematic 3D mapping of φ_r, we decided to simply play three shots for each temperature measurement: one φ_r calibration shot, one unsensitized shot, and one sensitized shot. These three shots permit the reconstruction of two complex valued images, one corresponding to the unsensitized shot, one to the sensitized-shot. From these two complex images we produce by phase difference, a new complex valued image, where the phase of the local complex value is mainly influenced by the local frequency differences during the evolution time τ (hardware errors are eliminated through subtraction).

Water proton resonance frequency shift
The proton resonance frequency shift is a shift in the resonance frequency of water protons caused by a change in the efficiency of the shielding electrons of the water proton under the influence of temperature.[11] With increasing temperature, water becomes more diamagnetic, with a temperature coefficient of -0.01 ppm/°C. These small changes can be detected as phase changes in the complex image, and the temperature difference ΔT can be quantified using

$$\Delta T = \frac{\Delta \varphi}{\gamma \cdot \alpha \cdot B_0 \cdot \tau} \qquad [1]$$

where $\Delta \varphi$ is the measured phase change, γ is the gyromagnetic ration, B_0 is the main magnetic field, and τ is the sensitization time, which allows the build up of the PRF shift. Analysis of the SNR of the temperature measurement versus τ shows, that ideally, PRF thermometry should use a τ that is close to T_2^*.[12-13] In gradient echo imaging this is typically accomplished by both echo shifting techniques[13] and echoplanar readouts.[2]
As shown in equation 1 the measured chemical shift is linearly related to temperature. Because the main field inhomogeneity is indistinguishable from the proton resonance frequency shift, one can only measure a change in temperature: we thus acquire images in series, with the first image serving as a thermal baseline. Changes from this baseline are considered to reflect chemical shift dependent temperature changes, using the generally accepted relation from equation 1.

Natural cooling experiments
To demonstrate the feasibility of PRF based MR thermometry, using the proposed non-CPMG FSE method, experiments were performed, in which images from a phantom were acquired during cooling. The phantom used was a gel (5% agar, Sigma; 95% distilled water, T_1/T_2^*=2263.7±52.6 ms / 45.4±0.8 ms), that was uniformly heated up to 60°C, placed in a thermally insulating Styrofoam block together with similar agar gels at room temperature and put in the scanner. To validate our MR measurements, fibers from a Luxtron 790 fiberoptic thermometric device (Luxtron; Santa Clara, California, USA) were carefully positioned in all gels. This setup was placed in the scanner where it was allowed to cool down, during continuous acquisition of images by the MR imager.

   In six experiments we assessed the dependence of PRF-shift quantification produced by the proposed non-CPMG FSE versus τ (7,11,15,19,24 and 30 ms). All experiments were replicated four times, leading to a total of 24 experiments, each containing 100 phase maps with corresponding temperature.

Laser experiment
To demonstrate the feasibility of measuring locally varying temperature, images were taken from the same gel while a laser (Dornier Medilas 5100, λ=1064, ⌀ 0.6 mm, sapphire tip, 10 W for 2 minutes) was irradiating the gel.

MR imaging
Imaging was performed with GE Signa CV/*i* (General Electric, Milwaukee, Wisconsin, USA), with LX 8.4 software, 40mTm^{-1} gradients and 268 μs slew rate. In the natural cooling experiment, we first located the Luxtron fibers in the gel using standard localizing sequences. Then, the thermosensitive non-CPMG FSE sequence was run TE_{Eff}/TR/ETL=47.9+ τ ms/4000 ms/128 (Table 1). For the laser experiment, the laser fiber was located, and consecutive images were acquired.
During imaging the gel was locally heated by the laser. Every acquisition consisted of three shots. From these shots real and imaginary components were calculated and stored in the scanners database.

Table 1.   Imaging settings for the two experiments.

Target	TR	TE_{eff}	ET	BW	CS	FOV	Matrix	NEX	Thick
Gel	4000	47.9 + τ	128	62.5	fat	240x240	256x128	1	10
Laser	4000	57.9 (τ =10 ms)	64	62.5	No	240x120	256x64	1	10

Image processing
Real and imaginary images were taken from the scanner database, and converted to phase maps using IDL 5.3 (Research Systems Inc; Boulder, Colorado, USA). Then images were masked with a binary magnitude image and unwrapped using Flynn's Minimum Discontinuity Method,[14] to yield the linear phase change from the baseline image. From the series of phase maps regions were chosen in the heated gel and in the non heated gels. Phase difference maps were created by subtracting the first phase map from all consecutive maps. The phase difference calculation for the laser experiment was performed using complex subtraction, which was possible because of the low value of τ. Large values of τ may cause the phase difference to exceed 2π and may require phase unwrapping. For the natural cooling experiment, the changes in background magnetic field were estimated by fitting a plane through the phase difference of the nonheated markers.[15] The calculated phase that originates from magnetic field drift was subtracted from the image, and the residual phase near the Luxtron fiber was recorded together with the Luxtron reading. Correlations were calculated using SPSS 9.0 (SPSS; Chicago, Illinois, USA). Phase noise was estimated from both the correlation with real temperature and noise in an unheated phantom during the scanning procedure. Analysis of variance (ANOVA) was used to assess differences in temperature sensitivity, fitting errors and phase noise. Differences were analyzed using the Student-Newman-Keuls post hoc test. For the natural cooling experiment, a temperature map was calculated based on the PRF method.

RESULTS
Phase maps were collected every 30 seconds (12 seconds acquisition time, actual thermosensitive imaging about 650 ms), with a resolution of 1.9 x 0.9 x 10 mm. Typical magnitude and phase images are given in Figure 2. The images are relatively blurred, which is caused by the long echo train compared to the T_2 of the gel (650 vs 47 ms). However the large region of the uniformly heated gel is sufficiently visible to accurately quantify phase evolution over temperature. Scatter plots of MR phase versus temperature are shown in Figure 3, and they demonstrate that the phase value in the phase maps varied linearly with temperature. The correlation confidence r^2 varied from 0.952 to 0.990, depending on the τ value, with statistically identical standard error of the fitted coefficient ($p=0.216$). ANOVA showed that the temperature sensitivity was dependent on the τ setting, except for a τ value of 7 or 11 ms, which were statistically undistinguishable ($p=0.258$). With increasing values for τ an increase in sensitivity of -0.0106±0.0005 ppm/°C for each ms increase of τ was found.
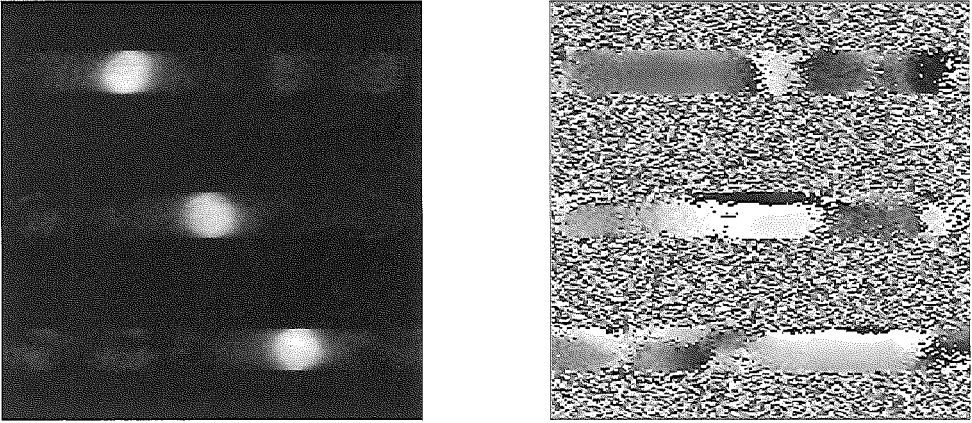
Figure 2. Typical magnitude (left) and phase (right) image. Note the extensive blurring that occurs due to the long echo train.
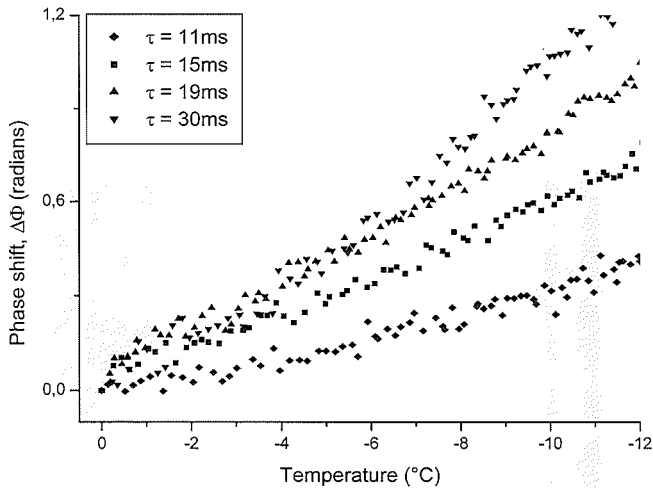

Figure 3. Different values of τ implicate different sensitivities to temperature. Temperature is normalized at the start of the experiment. Phase differences are taken from the reference phase at the start of the experiment.

The mean and variability of the fitted temperature sensitivity are shown in Figure 4. Statistically the phase noise did not change significantly with varying τ ($p=0.119$).
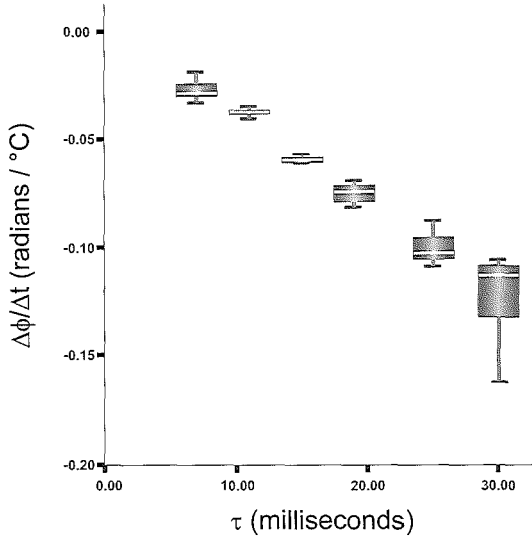
Figure 4. The box plot shows the mean (line within the box), ±2 standard deviations (box) and extreme values (whiskers). Apparently, at $\tau \cong 10$ ms, we find a very narrowly defined heat coefficient. With larger τ, we find increased temperature sensitivity, but also increased confidence interval. The relation of this heat coefficient over τ, shows that the value of the temperature dependent screening constant agrees well with given in the literature value[18] (-0.0106±0.005 versus -0.0101 ppm/°C). No differences in the temperature dependent screening constant were found with regard to τ (p=0.094).
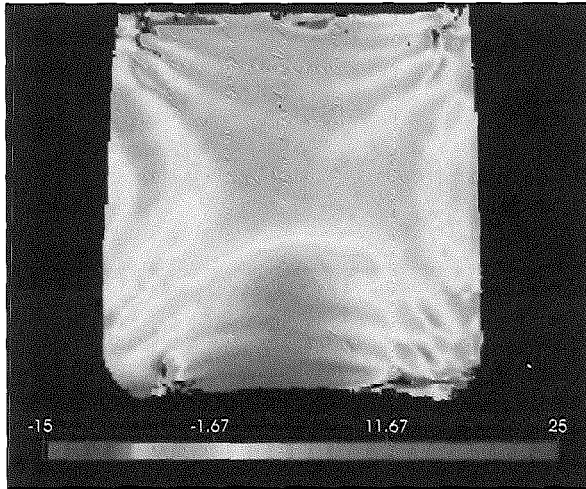
Figure 5. Images of the heat distribution after two minutes of laser irradiation using PRF sensitization of τ=10 ms. Extreme values at the edges of the phantom were clipped, and noise was masked out to improve image clarity. One can clearly see the reflection of laser light on the bottom of the container, resulting in an unexpected hot spot (A full color version of this illustration can be found in the color section).

A color coded image representing the laser induced heat distribution is shown in Figure 5, and in the color section of the appendix. The hot spot can be seen clearly, although there is some ringing artifact. Sufficient image detail is preserved to allow localization of temperature to the specific region of interest.

DISCUSSION

In this paper we have shown that by using a modification, the CPMG limitation can be overcome, and FSE can be used for precise and reproducible temperature measurements. Temperature sensitivity of the technique is set by the τ value. For both low and high values of τ we find increased uncertainty in the actual measurements on the heat coefficient. Optimization of τ has little impact on total imaging time, whereas gradient echo sequences typically must rely on echo shifting, or echo planar imaging in order to adjust the echo time to the optimal value of T_2^* of the region of interest, to achieve optimal temperature sensitivity.

Due to T_2 relaxation during readout, the spatial resolution is decreased. This is problematic as the thermal profile is smoothed, and therefore underestimates the true extent of thermal coagulation, when calculated using an Arrhenius model.[16] Therefore the sequence should be further optimized using outer volume suppression, point resolved spectroscopy (PRESS) selection or by using sensitivity encoding (SENSE) type reconstruction.[17] Doing so allows a smaller matrix to be used, while maintaining good spatial resolution. The shortened echo train will reduce blurring of the image while maintaining the advantages of the sequence, thereby increasing its potential for thermal therapy monitoring.

The proposed FSE sequence is still in an early development phase, and a full comparison with available optimized gradient echo sequences is premature. However, we believe that the current single-shot FSE approach provides some potential advantages over the conventionally used gradient echo techniques. Most significant is that the magnetization is sampled very rapidly. Apart from having good temporal resolution, one can hypothesize that this will also prevent short term chemical shift instability (during the acquisition in multi-shot gradient echo acquisition schemes), which could cause instability and spatial inconsistency of the thermal image. Also, oscillations in magnetization, brought about by incomplete steady state, cannot complicate the temperature measurements. And T_1 effects during multi-shot sampling, possibly due to rapid heating, cannot occur with the proposed single-shot FSE acquisition scheme. Because the generated signal is relatively large, the sequence is expected to achieve better results when using low field interventional scanners than conventional gradient echo techniques, given that gradient hardware is not a limiting factor.

The gain in SNR depends directly on the T_1, T_2' and T_2^* values of the target region. The FSE sequence is expected to perform better than gradient echo based sequences, except when T_1 of the target tissue is very short.

In summary, we have shown feasibility of PRF based thermometry using a non-CPMG FSE sequence. The robustness of the technique is promising. Thus *in-vivo* studies using this sequence are warranted and this is the topic of our current research.

REFERENCES

1. Salomir R, Vimeux FC, de Zwart JA, Grenier N, Moonen CT. Hyperthermia by MR-guided focused ultrasound: Accurate temperature control based on fast MRI and a physical model of local energy deposition and heat conduction. Magn Reson Med 2000; 43:342-347.
2. Stafford RJ, Hazle JD, Glover GH. Monitoring of high-intensity focused ultrasound-induced temperature changes *in vitro* using an interleaved spiral acquisition. Magn Reson Med 2000; 43:909-912.
3. Peters RD, Chan E, Trachtenberg J, et al. Magnetic resonance thermometry for predicting thermal damage: An application of interstitial laser coagulation in an *in vivo* canine prostate model. Magn Reson Med 2000; 44:873-883.
4. Hynynen K, Pomeroy O, Smith DN, et al. Mr imaging-guided focused ultrasound surgery of fibroadenomas in the breast: a feasibility study. Radiology 2001; 219:176-185.
5. Ishihara Y, Calderon A, Watanabe H, Okamoto K, Suzuki Y, Kuroda K. A precise and fast temperature mapping using water proton chemical shift. Magn Reson Med 1995; 34:814-823.
6. Carr HY, Purcell CM. Effects of diffusion on free precession in nuclear magnetic resonance experiments. Phys Rev 1954; 94:630-638.
7. Norris DG, Bornert P, Reese T, Leibfritz D. On the application of ultra-fast RARE experiments. Magn Reson Med 1992; 27:142-164.
8. Alsop DC. Phase insensitive preparation of single-shot RARE: application to diffusion imaging in humans. Magn Reson Med 1997; 38:527-533.
9. Le Roux P. Spin Echoes with a Quadratic Phase Modulation of the RF Pulse Train. Proceedings of Nineth Scientific Meeting of the International Society for Magnetic Resonance in Medicine. Glasgow, UK, 2001. pp. 1788.
10. Le Roux P. Non-CPMG Fast Spin Echo with full signal. J Magn Reson 2002; 155:278-292.
11. Hindman JC. Proton resonance shift of water in gas and liquid states. J Chem Phys 1966; 44:4582-4592.
12. MacFall JR, Prescott DM, Charles HC, Samulski TV. 1H MRI phase thermometry *in vivo* in canine brain, muscle, and tumor tissue. Med Phys 1996; 23:1775-1782.
13. de Zwart JA, van Gelderen P, Kelly DJ, Moonen CT. Fast magnetic-resonance temperature imaging. J Magn Reson B 1996; 112:86-90.
14. Ghiglia DC, Pritt MD. Two-dimensional Phase Unwrapping: Theory, Algorithms, and Software: John Wiley and Sons, Inc., 1998.
15. De Poorter J. Noninvasive MRI thermometry with the proton resonance frequency method: study of susceptibility effects. Magn Reson Med 1995; 34:359-367.
16. Sapareto SA, Dewey WC. Thermal dose determination in cancer therapy. Int J Radiat Oncol Biol Phys 1984; 10:787-800.
17. Pruessmann KP, Weiger M, Scheidegger MB, Boesiger P. SENSE: sensitivity encoding for fast MRI. Magn Reson Med 1999; 42:952-962.
18. Peters RD, Hinks RS, Henkelman RM. Ex vivo tissue-type independence in proton-resonance frequency shift MR thermometry. Magn Reson Med 1998; 40:454-459.

Towards Motion-Robust Magnetic Resonance Thermometry

ABSTRACT

Magnetic Resonance Imaging allows for minimally invasive targeting and thermal ablation of tumors while monitoring the temperature distribution. Conventional MR thermometry procedures are hampered by either low accuracy or high sensitivity to motion artifacts due to the use of a reference temperature image. A new, dual-echo technique has been developed to obtain the temperature distribution within a single MR-acquisition. The acquired phase images were post-processed using noise filtering and advanced phase unwrapping, to obtain the two-dimensional temperature distribution. *In-vitro* calibration experiments showed that the accuracy of our newly developed technique is similar to existing thermometry approaches. There was a good linear relationship (r^2=0.99) between the measured phase difference and the recorded temperature up to at least 65°C. The reproducibility of the temperature coefficient ($\Delta\varphi/\Delta T$) was within 5%. Real-time temperature mapping and solving susceptibility inhomogeneity are under investigation.

Mika W. Vogel, MSc ♦
Suprijanto, MSc ✳
Frans M. Vos, PhD ♦✳
Henri A. Vrooman, PhD ♦♥
Albert M. Vossepoel, PhD✳
Peter M.T. Pattynama, PhD,MD ♦

From
♦ departments of Radiology and
♥ Medical Informatics
Erasmus MC, University Medical Center Rotterdam, The Netherlands.
✳ Department of Applied Physics, Delft University of Technology, The Netherlands

Keywords
Magnetic Resonance Imaging
Thermography
Phantom
Proton Resonance Frequency shift

INTRODUCTION

On-going improvements in recognition and staging of tumors allow for early management of related morbidity. Tumor size is usually controlled by suppressive chemotherapy. Minimally invasive surgery may be especially beneficial in the early stage of cancer, when lesions are small. Thermal surgery may be an appropriate form of minimally invasive surgery since coagulated tissue allows for regeneration of healthy tissue.

The curative effect of (ablative) hyperthermia on soft tissue tumors has been known for over half a century. The resulting heat distribution, however, is difficult to predict. Due to the *a priori* unknown differences in thermal conductivity, diffusion and physiological cooling effects, the efficiency of hyperthermic applications is greatly reduced. Models for predicting the temperature distribution, especially in the higher temperature range used for ablative therapy, are not yet fully established.[1] With the availability of advanced imaging equipment, temperature changes during treatment can be visualized using ultrasound[2] or Magnetic Resonance Imaging (MRI).[3-4] Use of temperature information allows for monitoring and controlling temperature related events.[5-6] Registering changes in temperature for specific pixels allows for precise thermal dose calculation.[7]

MRI has been favored for monitoring local hyperthermia therapy, since it offers both target visualization and temperature sensitivity. Temperature sensitivity by MRI has been demonstrated for the apparent diffusion constant, the spin-lattice relaxation time (T_1), and the water proton resonance frequency shift. The frequency shift approach is accurate, but very sensitive to motion artifacts that may lead to corrupted temperature information.

The objective of this paper is to show that sufficiently accurate temperature information can be collected in a single MR-acquisition using a newly developed procedure, which may apply for thermometry purposes *in-vivo*.

MATERIAL AND METHODS

There is a direct relationship between tissue temperature and proton (spin) mobility.[8-10] For diamagnetic materials, such as soft tissues in the human body, the moving electrons around the proton spin result in a small local magnetic field, opposing the applied field (B_0). This shielding is temperature dependent. For water, the screening constant (α shows a linear increase with increasing temperature over a broad range ($T\varepsilon\,[0,83°C]$).[9,11]

Conventional Phase Shift Thermometry

The change in the local magnetic field causes a change in the Larmor frequency, resulting in phase differences in the acquired MR phase image. The measured phase $\Delta\phi$ can be used for calculating differences in temperature ΔT, according to:[12]

$$\Delta\varphi = \gamma \cdot \alpha \cdot B_0 \cdot \Delta T \cdot \tau \qquad\qquad [1]$$

where γ is the gyromagnetic ratio, α the temperature coefficient, t the echo time, and B_0 the main magnetic field.

Measured phase is relative to the phase at initial temperature and therefore easily invalidated when voxels are displaced by patient breathing or patient movement. Recent studies have shown the feasibility of MR-controlled hyperthermia using the phase shift method, albeit in the absence of tissue motion.[13] In order to be able to employ the phase shift, the method should be robust for phase changes that result from motion.

Dual-echo Phase Shift Thermometry
Because currently not all movement artifacts can be corrected for, we investigated the use of the phase that develops between two subsequent echoes for the measurement of temperature, instead of referencing to the static phase reference from a fixed geometry that was acquired prior to heating. The difference between two sampled phases for the same region yields, with a given period, a specific frequency for that region, which translates into local temperature differences.

We modified the standard spoiled gradient echo sequence to incorporate a second readout period. If two echoes are acquired successively using one excitation only, this yields:

$$\varphi_1 - \varphi_0 = \gamma \cdot \alpha \cdot B_0 \cdot (T_1 - T_0) \cdot \tau_1,$$

$$\varphi_2 - \varphi_0 = \gamma \cdot \alpha \cdot B_0 \cdot (T_2 - T_0) \cdot \tau_2. \qquad\qquad [2]$$

Now if we assume that

$$T_1 \approx T_2 \Rightarrow \Delta\varphi_{2-1} = \kappa \cdot \Delta T \cdot (\tau_2 - \tau_1), \qquad\qquad [3]$$

where κ incorporates the constant terms, temperature relates directly to the phase evolution. When we take into account the surroundings of the object, for which we assume identical shielding and main magnetic field, we can normalize the evolution of phase to the pixels in the vicinity, rather than using base images.

Analysis of the local magnetic field in a chemically homogeneous sphere, shows that the macroscopic susceptibility is approximated by $H * (1-2) * (\chi_e - \chi_0)/3)$.[14] At the microscopic level, we arrive at an expression for the local magnetic field that is only a function of the temperature dependent screening constant.

Experiments
To demonstrate the reproducibility of the conventional thermometric procedure and to compare the measured α with values in the literature, an experiment was carried out in which phase images from a phantom (n=10) were acquired

(Experiment 1). The used phantom was a gel (5% agar, Sigma; 95% distilled water) that was heated in a water bath up to 70°C and was put in a Styrofoam box. This setup was placed in the MR-scanner, where it was allowed to cool down to 30°C during continuous acquisition of MR images. In total, more than 100 time samples were acquired. MR hardware consisted of a GE CV/*i* 1.5T scanner (slew rate 150 $Tm^{-1}s^{-1}$, gradient strength 40 mTm^{-1}, rise time 268 μs). Scanning was done using a conventional gradient echo scanning technique (Table 1). Gel temperature was simultaneously recorded using a fiber optic measurement device (Luxtron 790, Luxtron, Santa Clara, USA). The fibers were positioned in both the phantom and a reference gel.

To be able to make comparisons between the temperature sensitivity of the conventional and the newly developed dual-echo method, two experiments (Experiment 2 and 3) were carried out, with identical experimental setup and comparable imaging settings. In Experiment 2 (n=10), a spoiled gradient recalled echo sequence was employed to assess the conventional phase difference versus temperature. The procedure was repeated for Experiment 3 (n=10) employing the newly developed dual-echo pulse sequence.

Table 1. Imaging parameters for the different experiments. All sequences were steady state incoherent.

Parameter	Experiment 1	Experiment 2	Experiment 3
Sequence	Conv. GRE	Conv. GRE	Dual-echo GRE
TR (msec)	40	40	40
τ_1 / τ_2 (msec)	6.8 / NA	20 / NA	20.0 / 30.0
Temporal resolution (sec)	10	10	10
Flip angle (^{o})	20	20	60
Number of excitations	1	1	1
Slice thickness (mm)	10	10	5
Field of view (mm^2)	480 x 480	240 x 240	240 x 240
Bandwidth (kHz)	16	16	16
Matrix	256 x 256	256 x 256	256 x 256

To assess the generalizability of referencing the temperature using the phase difference between the current pixel and neighboring pixels, a final experiment was carried out, using a homogeneous spherical phantom, positioned at the iso-center of the MR-bore. According to the theory, there should be a uniform

phase over a homogeneous sphere. Two phase images were acquired, using the same pulse sequence as was used in the Experiment 3, with identical processing.

Image Post-processing

Images were transferred off-line from an SGI Octane (SGI, Mountain View, CA, USA) to a PC using the DICOM transfer protocol. Further processing was carried out using IDL 5.3 for Windows (Research Systems Inc, Boulder, CO, USA). Phase values are normally computed by taking the arctangent of the real and imaginary part of the MR image, yielding phase values modulo 2π. Further post-processing of the data is hampered by the resulting phase jumps (transitions from π to $-\pi$). An example of a phase image is shown in Figure 1. The central object is the heated agar gel. The surrounding objects are reliability markers to correct for main field drift.

To correctly restore the original linear phase in a pixel, its direct surrounding can be used. The solution to this problem, however, is not trivial. We unwrapped the phase images using Flynn's Minimum Discontinuity Method.[15] In addition to Flynn's algorithm, quality maps and noise filtering (of the real and imaginary part of the signal) were used to optimize the unwrapping process. Afterwards, phase maps were calculated by subtracting the reference image from consecutive phase images. From these phase maps a pixel was selected within the heated gel nearby the inserted Luxtron fiber. The local phase evolution was compared with the measurements of the Luxtron device for the times at which the echoes were acquired. For the dual-echo technique a similar procedure was followed, except that the difference was computed from the phase images that were acquired in one single acquisition.
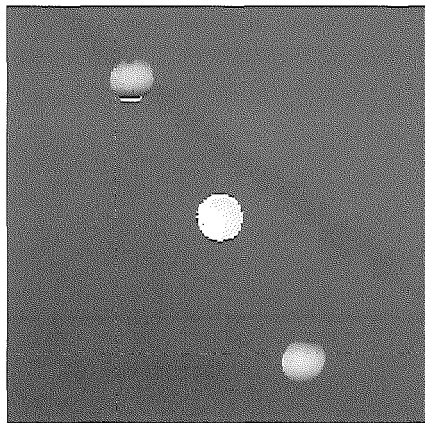
Figure 1. A typical resulting phase image with three gels in the field of view. The outer two function as magnetic field markers. The temperature over the central gel changed during the course of the experiment. Phase of the background is masked out in this image, to improve visibility. Note the small phase jump in the upper marker.

In both experiments the mean heat coefficient was determined by linear regression. The temperature uncertainty was defined as ±SD of the temperature difference between MR and the fiber optic measurements. Phase noise was estimated from the ±SD of the phase signal in the non-heated reliability markers.

Results

To validate the newly developed procedure for MR thermometry, the reproducibility and accuracy of the measured temperature coefficient α was determined from the experiments mentioned above.

Reproducibility of the Temperature-Dependent Screening Constant

The temperature-dependent screening constant α (Table 2) was within the range of values from the literature,[16] and showed low standard error for the conventional as well as the dual-echo technique. The variation of the screening constant using the conventional method was about 5%, which may be caused by a variety of sources and is generally acceptable.

Temperature Sensitivity

The linearity and sensitivity for the dual-echo technique are depicted in Figure 2. There was good linearity (r^2=0.99) with temperature that holds up to at least 65°C.
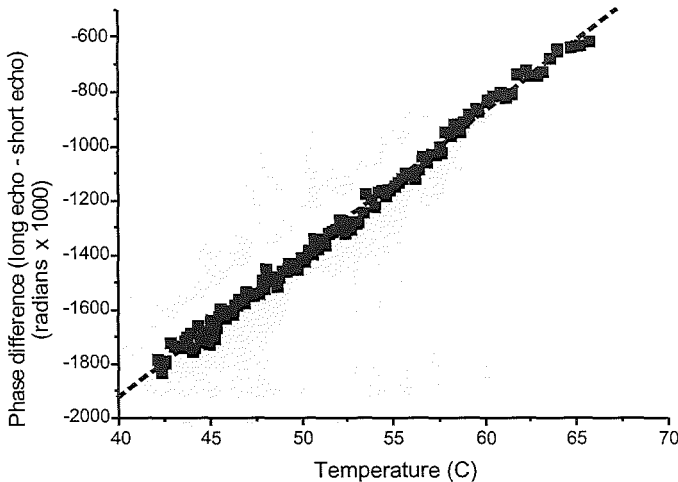
Figure 2. The evolution of phase difference from the dual-echo technique is plotted against temperature.

The sensitivity of the dual-echo technique was slightly less than that of the conventional technique (see Table 2), as it was the result of two measurements

with unrelated errors. The dual-echo sequence suffered from lower SNR due to a smaller voxel size and a relatively high flip angle.

Table 2. Temperature uncertainties, noise, and coefficients for both the conventional and the dual-echo method.

Parameter	Experiment 2	Experiment 3
Sequence	Conventional GRE	Dual-echo GRE
MR versus Luxtron	±0.57 °C	±1.20 °C
MR noise	±1.10 °C	±0.89 °C
Temperature coefficient	0.0106±0.0001 ppm/°C	0.0098±0.0001 ppm/°C

Spatial Stability of the Dual-echo Phase Difference
As seen in Figure 3, the spatial stability of the phase was low. The dual-echo sequence used did not compensate for sampling errors during the two different readout periods. The conventional method is compensated for this type of errors, since it acquires images, which will be compared against each other, using the same gradient waveforms. Controlling and compensating for the sampling error due to the gradient waveforms of the dual-echo sequence is the topic of current research.
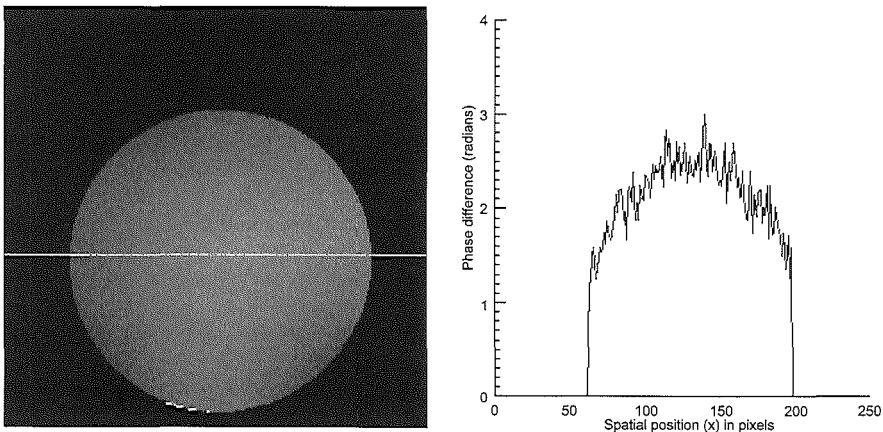
Figure 3. Clearly visible is the change of phase value over the spherical phantom (left). In the right graph, the intensity (phase difference) profile along the horizontal line is shown. Again the background phase is masked for improved visualization. Sampling errors lead to such a pattern, and can be compensated for.

DISCUSSION
In this paper, we have shown that the dual-echo sequence may allow for temperature encoding using the information from one MR acquisition only. Phase

difference between the two generated images, varies linearly with temperature. The accuracy is slightly less when compared with the conventional thermometry method. The reproducibility of the temperature coefficient, however, was good. The inconsistency between the screening constants from the conventional method versus the dual-echo method may be explained by a slightly different makeup of the fabricated gel. Minuscule bubbles of air, may affect the evolution of phase approaching the order of the heating constant. However, *in-vivo* micro-bubbles are not an issue. The expectation is that temperature changes can be calculated using the established screening constant of -0.0101 ppm °C^{-1}.[16]

The found temperature resolution is sufficiently close to 1°C, and therefore within the acceptable range for hyperthermia applications. Several reports[17,18] have shown a decreased sensitivity in actual *in-vivo* settings. Consecutive experiments will include *in-vivo* measurements to determine whether the sensitivity of the proposed dual-echo technique suffices for *in-vivo* application.

Due to sampling error, variations in the spatially localized signal occur. These imperfections cannot be estimated from the acquired images. Theoretically they can be assessed when using a slightly adapted version of the dual-echo sequence, incorporating refocusing pulses. Removing these imperfections is the strategy to overcome the spatial limitation of the dual-echo technique. In order to allow quantification of temperature from pixels relative to others in the same image, the overall phase should be constant. Using this constant, one can normalize the phase to a properly referenced temperature.

REFERENCES

1. Sherar MD, Moriarty JA, Kolios MC, et al. Comparison of thermal damage calculated using magnetic resonance thermometry, with magnetic resonance imaging post-treatment and histology, after interstitial microwave thermal therapy of rabbit brain. Phys Med Biol 2000; 45:3563-76.
2. Gertner MR, Worthington AE, Wilson BC, Sherar MD. Ultrasound imaging of thermal therapy in in vitro liver. Ultrasound Med Biol 1998; 24:1023-32.
3. McDannold NJ, Jolesz FA. Magnetic resonance image-guided thermal ablations. Top Magn Reson Imaging 2000; 11:191-202.
4. Quesson B, de Zwart JA, Moonen CT. Magnetic resonance temperature imaging for guidance of thermotherapy. J Magn Reson Imaging 2000; 12:525-33.
5. Madio DP, van Gelderen P, DesPres D, et al. On the feasibility of MRI-guided focused ultrasound for local induction of gene expression. J Magn Reson Imaging 1998; 8:101-4.
6. de Zwart JA, Salomir R, Vimeux F, Klaveness J, Moonen CTW. On The Feasibility Of Local Drug Delivery Using Thermo-Sensitive Liposomes and MR-Guided Focused Ultrasound. Proceedings of ISMRM 2000.
7. Sapareto SA, Dewey WC. Thermal dose determination in cancer therapy. Int J Radiat Oncol Biol Phys 1984; 10:787-800.
8. Bottomley PA, Foster TH, Argersinger RE, Pfeifer LM. A review of normal tissue hydrogen NMR relaxation times and relaxation mechanisms from 1-100 MHz: dependence on tissue type, NMR frequency, temperature, species, excision, and age. Med Phys 1984; 11:425-48.
9. Hindman JC. Proton resonance shift of water in gas and liquid states. J Chem Phys 1966; 44:4582-92.

10. Nelson TR, Tung SM. Temperature dependence of proton relaxation times in vitro. Magn Reson Imaging 1987; 5:189-99.

11. Schneider WG, Bernstein HJ, Pople JA. Proton magnetic resonance chemical shift of free (gaseous) and associated (liquid) hydride molecules. J Chem Phys 1985; 28:601-7.

12. Ishihara Y, Calderon A, Watanabe H, et al. A precise and fast temperature mapping using water proton chemical shift. Magn Reson Med 1995; 34:814-23

13. Salomir R, Palussiere J, Vimeux FC, et al. Local hyperthermia with MR-guided focused ultrasound: spiral trajectory of the focal point optimized for temperature uniformity in the target region. J Magn Reson Imaging 2000; 12:571-83.

14. de Poorter J, Noninvasive MRI thermometry with the proton resonance frequency method: study of susceptibility effects. Magn Reson Med 1995; 34:359-67.

15. Ghiglia DC, Pritt MD. Two-dimensional Phase Unwrapping: Theory, Algorithms, and Software: John Wiley and Sons, Inc., 1998.

16. Peters RD, Hinks RS, Henkelman RM. Ex vivo tissue-type independence in proton-resonance frequency shift MR thermometry. Magn Reson Med 1998; 40:454-9.

17. De Poorter J, De Wagter C, De Deene Y, et al.. Noninvasive MRI thermometry with the proton resonance frequency (PRF) method: in vivo results in human muscle. Magn Reson Med 1995; 33:74-81.

18. Botnar RM, Steiner P, Dubno B, et al. Temperature quantification using the proton frequency shift technique: In vitro and in vivo validation in an open 0.5 Tesla interventional MR scanner during RF ablation. J Magn Reson Imaging 2001; 13:437-44.

Displacement Correction Scheme for MR-Guided Interstitial Laser Therapy

ABSTRACT

MR guided interstitial laser therapy can be used to monitor the extent of tumor tissue coagulation during thermal treatment based on a temperature map. In a non-stationary object that was influenced by respiratory motion, the temperature map may show errors due to incorrect spatial baseline images. Moreover, an unwanted phase shift due to object displacement contributes to errors in the temperature map, that must be suppressed. This paper describes a strategy which addresses the difficulties of MR guided interstitial laser therapy in the presence of respiratory motion. The multi-baseline images, supported by the displacement correction scheme, were used to improve the temporal resolution of a temperature map in the respiratory cycle. In the displacement correction scheme, the object coordinates that are provided by an active tracking coil were employed to support a matching strategy between the thermal and baseline images. To avoid errors in the temperature map due to the motion artifact, a detector of low quality images was proposed as part of the displacement correction scheme.

Suprijanto, MSc ✳
Mika W. Vogel, MSc ◆
Frans M. Vos, PhD ◆✳
Henri A. Vrooman, PhD ◆♥
Albert M. Vossepoel, PhD ✳

From
◆ The departments of Radiology and
♥ Medical Informatics Erasmus MC, University Medical Center Rotterdam, Rotterdam, The Netherlands.
✳ Department of Quantitative Imaging, Delft University of Technology, Technical University Delft, Delft, The Netherlands

INTRODUCTION

The use of intense localized change in temperature is rapidly becoming an established surgical technique for destroying undesired tissue. Tissue ablation by percutaneous application of optical fibers and deposition of thermal energy via lasers, (called interstitial laser therapy), is an option for localized lesions, such as tumors, accessible via needle insertion. Dynamical temperature monitoring, with adequate spatial and temporal resolution could provide information about the extent of tissue coagulation. The goal is to avoid excess heating of surrounding healthy tissue and to ensure sufficient treatment of the tumor tissue.

MR Thermometry imaging is preferred for guided interstitial laser therapy, that is based on the relaxation time (T_1), the diffusion coefficient (D) or proton resonance frequency (PRF) shift of tissue water. The excellent linearity and near independence with respect to tissue type, together with good temperature sensitivity, make MR Thermometry based on PRF shift the preferred choice. In this approach, the PRF shift due to temperature changes can be mapped using the MR phase images in gradient-echo imaging.[1-3]

In the absence of motion, MR thermometry based on phase imaging is quite accurate.[1,3] Unfortunately, many clinical targets for tumor therapy however, especially in the abdomen, can not be held in stationary position due to respiration motion. In a non-stationary object, an error in the temperature map may occur due to incorrect spatial baseline images. Although a spatial transformation of the baseline image can be matched to the thermal image, an unwanted phase shift cannot be fully suppressed. Spatially varying field deviations can not be distinguished from temperature changes, and therefore leads to reduced thermal accuracy. A previous study showed that a reproducible phase image can be created, when scanning was done in the same position.[4] To improve the temporal resolution of temperature measurement, an objective phase shift map must be determined from various scanning positions that occur in the respiratory cycle. Furthermore, multiple temperature maps can be interpolated to more accurately follow the temperature profile in time.

Another problem that must be considered is the error in the temperature maps due to the motion artifact. This artifact is caused by movement of an object during MR signal readout, yielding a low quality image. One approach to minimize the motion artifact is using a fast imaging technique. For MR thermometry based on phase imaging, the echo shifted gradient-echo imaging has been developed to increase the imaging speed with optimal temperature sensitivity.[5] Nevertheless, due to the variability of respiratory motion, occasionally a motion artifact occurs in an image.

In this paper, we describe a strategy to determine a temperature map based on a phase-shift map in the presence of respiratory motion. To recover a phase-shift map, we propose using multi-baseline images, supported by a displacement correction scheme. In this scheme, the object coordinates that are provided by an

active tracking coil were employed to support a matching strategy between the thermal and baseline images. To avoid low quality images, a detector for sufficient image quality was proposed as part of the displacement correction scheme. For validation, the displacement correction scheme was applied to monitor temperature evolution during interstitial laser therapy in a liver model under respiratory motion simulation.

METHODS

Temperature Calculation Based on Objective Phase Shift Maps

A complex MR image $I(\vec{r}, T)$ which is acquired by MRI at a certain temperature, is reconstructed by a Fourier transform of k-space data. Here, $\vec{r}$ and T denote the image coordinate and a specific temperature, respectively. $\Phi (\vec{r}, T)$ is a component of complex images that can be determined by taking arctan $[I(\vec{r}, T)]$. The objective phase shift is formulated as follows [5]:

$$\Phi\left(\overrightarrow{\Delta r}, \Delta T\right) = PU\left[\arctan\left[I\left(\vec{r}, T\right). I^*\left(\overrightarrow{r_{bl}^o} + \overrightarrow{\Delta r}, T_o\right)\right] + \Delta\,\phi(\overrightarrow{\Delta r})\right] \qquad [1]$$

where $I(\vec{r}, T)$, $I(\overrightarrow{r_{bl}^o}, T_o)$ are respectively a thermal and a baseline image, I^* is the complex conjugate of I. Phase unwrapping (PU) is used to recover the absolute phase shift in order to ensure that the phase shift is proportional with the large temperature variations in the therapeutic range. $\Delta\phi$ $(\overrightarrow{\Delta r})$ is the bulk of an unwanted phase shift, that must be suppressed. Ideally, proper subtraction can be done when thermal and baseline images were scanned at exactly the same location. This condition can be expressed as $\vec{r} = \overrightarrow{r_{bl}^o} + \overrightarrow{\Delta r}$ and $\overrightarrow{\Delta r} \approx 0$. Furthermore, after an objective phase shift can be recovered, the temperature map in each sample time t can be determined by taking the ratio between the current phase shift value and the temperature sensitivity ($\alpha\gamma B_o \tau$) in radians/°C, that formulated is as follows [1,3]:

$$\Delta T(\tau) = \frac{\Phi\left(\overrightarrow{\Delta r}, \Delta T, t\right)}{\alpha\gamma B_o \tau} \qquad [2]$$

where α is the temperature dependent water chemical shift, for which a value of 0.0101 ppm/°C is used in this work,[3] γ, B_o, and τ are respectively the gyromagnetic ratio, the magnetic field strength and the echo time.

Displacement Correction Scheme

Location Tags-Matching Strategy. The proper temperature maps can be determined when a thermal image matches with a baseline image. In a previous study, navigator echoes were employed for detection of 1-D object displacement, to support a matching strategy.[5-7] In this work, an active tracking coil was used to obtain the 3-D coordinates, relative to the heat-source location. The active tracking coil was integrated into a power laser sheath which was introduced into the object.

A custom receiver was used to detect a location information from the active tracking coil. In each scanning, the coordinates of location tags can be provided as
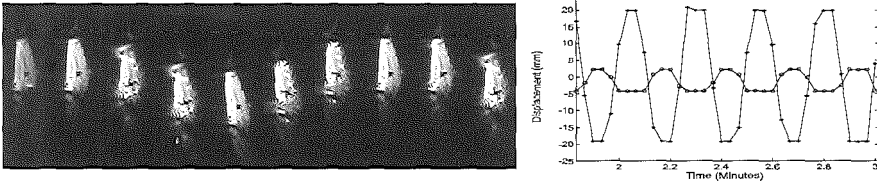

Figure 1. (Left) Sequences of intensity images in respiratory motion simulation in one cycle, (Right) the location tags from the active tracking coil that are scanned during 1.2 minutes; 'o' and '*' are the location tag projections on the x-axis and y-axis, respectively

additional information for MR images. The example of a series of intensity MR images and the location tag, that were acquired from a sample of porcine liver in a respiratory motion simulation, are shown in Figure 1.

The thermal image at a certain temperature T is given the notation $I(\vec{r},T)$ and multi-baseline images are given the notation $I(\vec{r}_{bl}^{\,o}, T_o)]$, where $bl = 1, 2, ..., n$ is a number of location tag for each multi-baseline image. The objective phase shift can be calculated when $I(\vec{r},T)$ matches with one of $I(\vec{r}_{bl}^{\,o}, T_o)]$, with minimized distance between r and one of $\{\vec{r}_1^{\,o},....,\vec{r}_n^{\,o}\}$, that is formulated as follows:

$$\left|\Delta\vec{r}_{bl}\right| = \min\left\{\left|\Delta\vec{r}_1\right|,.....,\left|\Delta\vec{r}_n\right|\right\} \qquad [3]$$

where

$$\left|\Delta\vec{r}_1\right| = \left|\vec{r}-\vec{r}_1^{\,o}\right| = \left|\left(x - x_1^0\right),\left(y - y_1^o\right),\left(z - z_1^o\right)\right| and \left|\Delta\vec{r}_n\right| = \left|\vec{r}-\vec{r}_n^{\,o}\right| = \left|\left(x - x_n^o\right),\left(y - y_n^o\right),\left(z - z_n^o\right)\right|.$$

The minimum distance value from one element $\{\left|\Delta\vec{r}_{bl}\right|\}$ is related with the index bl. When the index bl can be found, one of the multi-baseline images can be matched with a thermal image, allowing a temperature map to be calculated, based on objective phase subtraction, as formulated in Equation 1.

Detection of Low Quality Images
During scanning, a location tag and an image are acquired, respectively, and updated in each scan. Due to the typical respiratory motion profile, it is possible that two images have a similar location tag, but different image quality. As we explained above, low quality images may occur due to the motion artifact acting as a filter that smears the temperature information in the MR phase images. Therefore, low quality images must be removed. To support this task, image quality detection is proposed. The image quality can be determined from the degree of similarity between a grey value distributions of thermal and a baseline MR intensity image. As part of the displacement correction scheme, measurement

of the image quality was done after the location tags matching criterion could be achieved. In this work, the Entropy Correlation Coefficient (ECC),[6-7] in formula

$$ECC\left(S_T, S_{bl}\right) = \frac{2I\left(S_T, S_{bl}\right)}{H\left(S_T\right) + H\left(S_{bl}\right)} \qquad [4]$$

was used, where S_T and S_{bl} represent the intensities of the thermal and the baseline images, $I(S_T, S_{bl})$ and $H(.)$ represent the mutual information of both images and the entropy of the image, respectively. The lowest value of the ECC that is yielding an unreliable temperature map will be applied as a threshold value in the detector of low quality. The threshold value was determined experimentally.

MATERIALS AND RESULTS
Material
All experiments were performed at a clinical MRI, GE CV/i 1.5T scanner. Echo-shifted gradient imaging was applied to allow formation of gradient echoes that were shifted with one period (TR) periods after signal excitation. Thus echo time-TE>TR is employed. A 3-inch surface coil was used as a receiver. As imaging parameters, TR=9 ms ,TE=17 ms, FOV=250 mm x 250 mm, slice thickness 5 mm and flip angle 22° are used. With these imaging parameters, acquisition time for each image is about 2 seconds. As heating source, a laser fiber (600 micrometer diameter) with a diffusing tip was inserted into the liver model. Laser irradiation (wavelength 1064 nm) with a power of 10-25 Watt was applied as the heat-source. The laser sheath was then introduced into a sample of porcine liver. This was placed onto a device that simulated respiratory motion, with a motion profile as shown in Figure 1.

Experimental Procedure
Before the MR-guided interstitial laser was applied, the following steps were performed :

Step-I. The respiratory motion simulator was activated, after the heating and tracking devices had already been installed into the liver model. Without activated laser, pre-scanning was applied to acquire multi-baseline images were defined from location tags that simulated inspiration and expiration locations. Furthermore, a temperature map was calculated based on the location tags matching strategy.The criterion for minimum distance of$\{\left|\overrightarrow{\Delta r_{bl}}\right|\}$ $\leq$ 1.0 mm was selected. After that, a threshold value of ECC (Θ_{ECC})was determined to eliminate the lowest quality images from temperature calculation, as follows:
   - tabulation of relationship between background temperature and ECC values
   - select a set of ECC values that have a relationship with the variation of the background temperature within a certain range
   - calculation of mean (μ_{ECC}) and standard deviation (σ_{ECC}) of the ECC from a set of ECC values, that was already selected

- The threshold value of Θ_{ECC} defined as $\mu_{ECC} - \sigma_{ECC}$

Step-II. In this step, the displacement correction scheme is ready to monitor temperature evolution for a liver model under interstitial laser therapy, in series scanning.

For reliable thermometry, the variation of the temperature should be within a range of 1°C, a value that often can be achieved for immobile object.[1] From a previous study, a variation of temperature in the moving liver within range ±3.5°C was reported after 6 minutes of laser irradiation.[4] Considering the ideal value and a tolerable value to the unwanted phase shift was not fully eliminated, the variation of the background temperature within ±1.5°C was applied to select a set of ECC value.

Experiment

In the first experiment, the performance of the motion correction scheme was evaluated to calculate the background temperature in a liver model in the respiratory motion simulation, without activated laser. In step I, the baseline images were defined from images with location tags $\vec{r}_1^{\,o}$ =(-1.5mm, 25.0mm , 0.0mm) and $\vec{r}_2^{\,o}$ = (1.5mm, -25.0mm, 0.0mm). The average temperature from 4 voxels, 5 mm from the laser tips position was used for evaluation. After that, pre-heating scanning with an effective duration of 2-3 minutes was done to determine Θ_{ECC}. Then, tabulation of the relationship between background variation of temperature and the value of ECC was done. An example of the relationship between both parameters is shown in Figure 2. Relationships between low value of ECC and the background variation of temperature beyond ±1.5°C can be seen in this figure. Furthermore, after Θ_{ECC} was determined, the displacement correction scheme was ready to calculate background temperature from continuous scanning during 10 minutes.
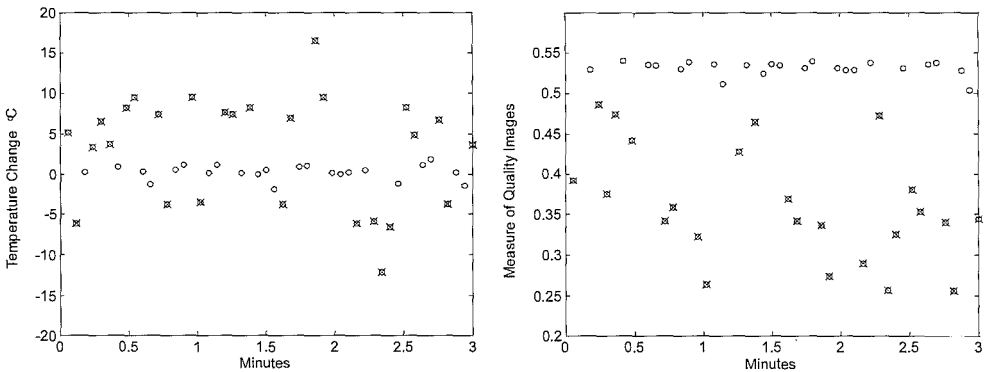
Figure 2. Relation between the temperature variation and the value of ECC. The temperature maps that yield the background temperature beyond ±1.5° C are marked by 'X', that relate to low values of ECC are also marked by 'X'

In Table 1, the standard deviation of background temperature obtained from multi-baseline images supported by the location tags matching strategy alone, and by a full displacement correction scheme are presented. A number of thermal images can be included to calculate a temperature map from 300 images acquired during 10 minutes, also given in Table 1.

Table 1. Standard deviation of background temperature from continous scanning in duration 10 minutes, without activated laser.

Baseline Image	Location Tags Matching	Displacement correction scheme
$\overrightarrow{r_2^o}$	4.9 °C (92 images)	1.1 °C (62 images)
$\overrightarrow{r_1^o}$	5.6 °C (93 images)	1.4 °C (65 images)
Interpolating $\overrightarrow{r_1^o}$ and $\overrightarrow{r_2^o}$	6.2 °C (185 images)	1.2 °C (127 images)

In the second experiment, the performance of the displacement correction scheme was evaluated for calculating the temperature evolution in the liver model in the respiratory motion simulation when laser power was activated. The range of respiratory motion was different from the first experiment. In step I, the baseline images were defined from two baseline images with location tags $\overrightarrow{r_1^o}$ = (-4mm, 25.0mm , 0.0mm) and $\overrightarrow{r_2^o}$ =(4mm, -25.0mm , 0.0mm). After that, preheating scanning during 4 minutes was applied to determine Θ_{ECC}. In step II, after Θ_{ECC} was determined, the displacement correction scheme was ready to monitor temperature evolution. The scanning series was done during 12 minutes under laser irradiation to acquire thermal images.

The uncertainties of temperature evolution due to position difference among temperature maps were analyzed. From the r_2-temperature map, five types of exponential function were fitted to the temperature evolution on 5 location points (See Figure 3). Furthermore, the temperature evolution from the r_1-temperature map was calculated also from 5 location points. The standard deviation of the temperature uncertainties (σ_{Tr}) were used to measure the uncertainties of temperature evolution from the r_1-temperature map relative to the exponential function fitted to the temperature evolution from the r_2-temperature map. The results of σ_{Tr} from 5 location points are presented in Table 2.

Finally, the area of iso-temperature was calculated from multiple 2-D temperature maps. The area evolution when T> 43°C and T> 50°C are presented in Figure 4.
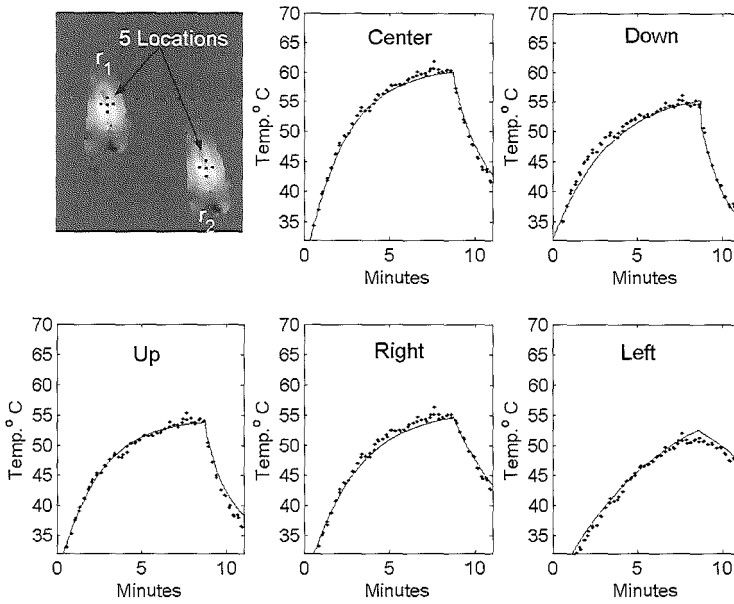
Figure 3. The temperature evolution of the average of 4 voxels is measured at 5 location points in the temperature map. Five points were located at the center (i.e at laser tip), and 4 mm down, up, left and right relative to the center . The temperature evolution from the r_1-temperature map was marked by ' $\cdot$ '. The exponential function that fitted to the temperature evolution from the r_2-temperature map was marked by ' – '.
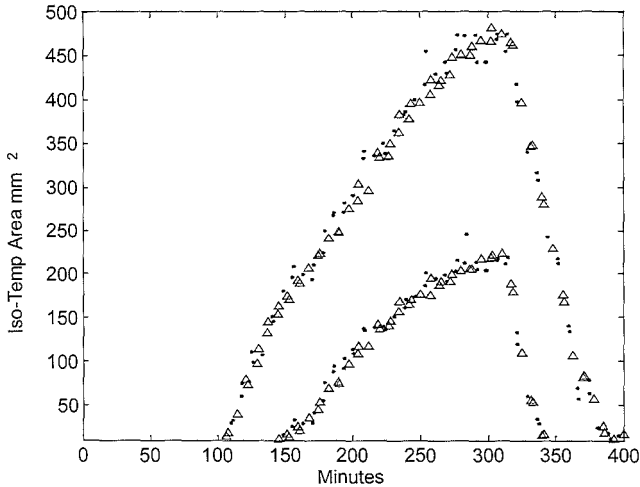
Figure 4. The iso-temperature area (mm^2) from the temperature map for $T > 43°C$ and $T > 50°C$; 'Δ' and ' $\cdot$ ' resulted from the r_1 and r_2 -temperature maps, respectively.

Table 2. The σ_T between temperature evolution from the r_1-temperature map and the exponential functions that fitted to temperature evolution from the r_2-temperature map on 5 location points.

Location points	Center	Down	Up	Right	Left
σTr	0.36 °C	0.29 °C	0.53 °C	0.42 °C	0.32 °C

Conclusions

We have developed a displacement correction scheme for MR guided interstitial laser therapy, and this scheme was tested in a liver model under a simplified respiratory motion profile. When an object can be assumed rigid, the combination between a tracking coil employed for a location tags matching strategy on the one hand, and a detector of low quality images on the other hand are useful to support a multi-baseline image technique. When multiple temperature maps can be interpolated to more accurately follow the temperature profile, then the proposed scheme will improve the temporal resolution of tissue-coagulation monitoring during interstitial laser therapy.

Acknowledgements

References

1. Quesson B, de Zwart JA, Moonen CT. Magnetic resonance temperature imaging for guidance of thermotherapy. J Magn Reson Imaging 2000; 12:525-533.
2. Wlodarczyk W, Hentschel M, Wust P, et al. Comparison of four magnetic resonance methods for mapping small temperature changes. Phys Med Biol 1999; 44:607-624.
3. Vogel MW, Suprijanto, Vos FM, Vrooman HM, Vossepoel AM, Pattynama PMT. Towards Motion-Robust Magnetic Resonance Thermometry. In Viergever M, Dohi T, Vannier M, eds. 4th Int. Conf. on Medical Robotics, Imaging and Computer Assisted Surgery. Utrecht, NL:
4. Heisterkamp J, Matheijssen NA, van Hillegersberg R et al. Accuracy of MR phase mapping for temperature monitoring during interstitial laser coagulation (ILC) in the liver at rest and simulated respiration, Magn Reson Med 1999; 41: 919–925
5. de Zwart JA, Vimeux FC, Palussiere J, et al. On-line correction and visualization of motion during MRI-controlled hyperthermia. Magn Reson Med 2001; 45:128-137.
6. J.V. Hajnal, D.L.G. Hill, D.J. Hawkes. Medical Image Registration, CRC Press LCC 2001
7. M. Frederik, A. Collignon, et.al. Multimodality Image Registration by Maximization of Mutual Information, IEEE Trans On Medical Imaging, Vol. 16, No.2, 1997

Phase-shift based magnetic resonance thermometry in moving objects:
combining unipolar echo-planar imaging with a multi-baseline acquisition scheme

Mika W. Vogel, MSc ◆
Suprijanto, MSc ✳
Peter M.T. Pattynama, PhD, MD ◆

From
◆ Department of Radiology, Erasmus MC, University Medical Center Rotterdam, The Netherlands.
✳ From the Department of Quantitative Imaging, Delft University of Technology, Technical University Delft, Delft, The Netherlands.

ABSTRACT

Motion-related artifacts can compromise current phase-shift based MR thermometry methods. Here, we propose a novel MR thermometry scheme to improve the accuracy of phase-shift based MR thermometry during motion.

MR thermometry was performed at 1.5T using single shot echo-planar imaging in combination with a multi-baseline referencing method. The accuracy of the proposed MR thermometry technique was validated and compared with the conventional spoiled fast gradient echo sequence, both under static conditions and during various types of motion.

In-vitro calibration experiments showed good temperature sensitivity and better accuracy than the reference technique (standard error of the estimate of 0.25°C versus 1.41°C, $p<0.001$). It also proved feasible to image laser heating in a moving liver phantom, with accurate temperature readings.

Using the proposed technique and processing scheme, phase-shift based MR thermometry is feasible during motion. This is an improvement over standard MR thermometry techniques.

INTRODUCTION

Percutaneous thermal ablation of tumor tissue is gaining increasing acceptance as a patient-friendly, minimally invasive alternative treatment to surgical resection. A key issue is monitoring the treatment in real-time, to decide when it is complete and should be stopped to avoid destruction of too much healthy, surrounding tissue.

An attractive method to monitor thermo-ablative treatment is by real-time magnetic resonance (MR) thermometry based on the proton resonance frequency (PRF) shift.[1] Spins in heated tissue will have increased PRF, according to:

$$\Delta\varphi = \gamma \alpha B_0 \tau \Delta T \qquad [1]$$

Where $\Delta\phi$ is change in phase, γ is the gyromagnetic ratio, α is the temperature sensitivity constant, B_0 is the strength of the main magnetic field, τ is the PRF sensitization factor, and ΔT is the change in temperature. The PRF shift thus quantifies the tissue temperature relative to baseline conditions, assuming that it is directly proportional to a temperature change only. PRF-based MR thermometry has been shown to be accurate and precise, with <1.0°C in temperature estimates.[2,3]

Problems occur, however, in moving tissues. Magnetic flux is dependent on position and susceptibilities of nearby structures.[4] And any change in position will thus lead to a specific change in magnetic field that confounds the PRF shift. Furthermore, in moving tissue, a velocity dependent phase shift typically develops as a consequence of application of the imaging gradients (a feature that is well known and put to clinical use, e.g., in MR velocity mapping) causing even more PRF-shifts. The resulting overall PRF-shift will therefore not accurately reflect temperature change. Therefore PRF-based thermometry is severely hampered when respiratory motion is pronounced, for example in the liver. Unfortunately, the liver is also the organ most commonly treated with thermo-ablation.

It has been shown that one can accommodate the problem of displacement using reference (baseline) images that have been obtained at exactly the same geometric position, to quantify the PRF-shift in the actual image.[5] In absence of movement this will yield a PRF shift that will solely reflect a change in temperature[6] because there is no change in magnetic flux anymore, when transient magnetic field changes are ignored or compensated for.

Our aim was to develop an MR thermometry method that would accommodate the unwanted PRF-shifts that occur during positional changes and motion, making it feasible to perform PRF-based MR thermometry in moving objects such as the liver. We hypothesized that this could be achieved by combining two approaches: (1) using multiple reference points for MR thermometry obtained at multiple baseline positions (multi-baseline method) and (2) using a dedicated MR pulse sequence that would be inherently insensitive to

the extra PRF-shifts caused by motion, in particular, a modified single shot Echo Planar Imaging (EPI) pulse sequence.

First, we validated the accuracy of the proposed method in heated gels and in a focally heated spot during motion, using absolute temperature measurements with fiberoptic thermometry as the gold standard. Then, we directly compared, under varying conditions of motions, the proposed EPI MR pulse sequence and a conventional Fast SPoiled GRadient echo (FSPGR) pulse sequence, which is currently the standard sequence used for PRF-based MR thermometry.

METHODS
MR hardware and MR pulse sequences
MR imaging was done at 1.5T (CV/i, CNV3, 40mT/m, with 268µs rise time; General Electric, Milwaukee, Wisconsin). Validation studies at changed geometrical positions and during motion were done under controlled conditions by employing the motorized tabletop in the MR scanner. The movements of the tabletop were programmed using custom-made software and controlled from within the MR acquisition program.

The proposed new MR pulse sequence for PRF-based MR thermometry was a single-shot EPI sequence with an even echo single polarity echo train and an extra first order gradient moment nulling pulse preceding the readout gradient (Figure 1). Minimizing any linear velocity induced phase shift involves nulling of zero and first moment, M_0 and M_1 respectively:

$$M_{0,TE} = \int_0^{TE} kx\, dt = 0 \qquad [2]$$

$$M_{1,TE} = v_x \int_0^{TE} t\, kx\, dt = 0 \qquad [3]$$
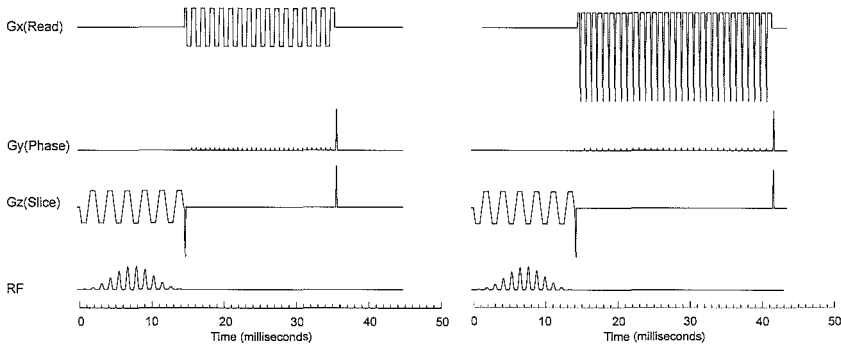
Figure 1. Conventional Echo Planar Imaging (EPI) sequence (left) and a single polarity EPI (right). Note that the echo rephasers employ maximal gradient switching in order to increase efficiency of the single polarity EPI.

The observation has been made that a single polarity multi echo readout train always fulfills the condition for a zero and first order moment for the second and higher echoes when these are sampled symmetrically. Therefore, such a gradient structure should be inherently insensitive to the phase terms caused by moving structures with constant velocity along the compensated gradient waveforms. Due to the speed of acquisition, motion blur along the imaging gradients and magnetic flux changes as a function of position are minimized.

Sequence parameters for the proposed EPI sequence were $(\theta/TE/TR/BW/FOV=90°/40/1500/62.5/18)$ using a 3" surface coil. In between the readouts, the gradient rephasers employed maximal gradient power that could be adjusted to minimize the effects of eddy currents. No noticeable eddy current distortions remained when using a 2% longer rephaser gradient. The calculated maximal gradient switching was 132 T/s, 75% of the upper limit imposed by the International Electrotechnology Commission (IEC 60601-2-33) for the used gradient waveform timing. A spatial spectral pulse suppressed potential off-resonance effects from the presence of fat.[3] Image reconstruction was adapted to not perform time reversal on odd views. For comparison, we used a conventional FSPGR echo MR pulse sequence with a field of view of 18 cm. $(\theta/TE/TR/BW/FOV=10°/10/12.3/32/18)$, a type of sequence most commonly used for PRF-based MR-thermometry.[7-10]

MR thermometry of a uniformly heated gel in static and motion conditions
To assess the ability of the proposed EPI sequence to perform accurate PRF-based MR thermometry results, we performed three experiments, in which PRF measurements in a heated gel during cooling were compared against a fiberoptic thermometer (Luxtron 790, accuracy ±0.2°C; Luxtron Corp., Santa Clara, California, USA). In the first experiment, the gel remained static, and PRF was calculated from the voxels closest to the fiberoptic sensor by taking the arctangent of complex subtraction of the first image from all consecutive images. In the second experiment, the gel was alternated between two positions, and static during the image acquisition. PRF was now calculated from the first image at the object position from all consecutive images as before. Finally, we also acquired images during linear motion (13 mm/s) and processed them by position as before. Linear regression of the measured PRF versus fiberoptic temperature yielded the temperature sensitivity constant α. And comparisons were made between stationary and moving conditions.

MR thermometry of a heated focal spot in a moving porcine liver
Next, we assessed whether EPI MR thermometry could be applied to a focal spot in liver tissue, which is most relevant for MR thermometry in clinical practice. We inserted a laser fiber ($\varnothing$ 0.8 mm, diffuser tip Lightstic™; Rare Earth Medical, W. Yarmouth, MA) into an excised porcine liver. A focal hot spot was created by

applying continuous laser irradiation at λ=1064 nm, 20 W, for 5 minutes (Dornier Medilas 5100; Dornier Medizintechnik; Munich, Germany), during which continuous MR-thermometry was done. The movements of the table were the same as in the previous experiment. From the real time sequence controller, table positions (resolution 0.1 mm) were reported to the MR host immediately before an instance of the pulse sequence was played out. These positions were used to identify baselines that were used to reference other images as before. Because of the steep non-linear heat profile, we validated this experiment differently. We reasoned that, if the temperatures at zero motion were correct (as proved in the previous experiments), then the temperature curve within the voxel of interest at zero motion could serve as the reference to validate the MR-based temperatures in that same voxel during motion. Thus, we obtained the MR-based temperature data during motion and correlated these with the MR-based temperatures obtained under stationary conditions as the reference method.

MR thermometry in a heated gel under varying conditions of motion

We made a one-on-one comparison between the two methods in a moving heated gel phantom with fiberoptic temperature measurements as the gold standard. The MR tabletop was programmed to move in repetitive cycles at eight different linear velocities (13, 18, 23, ... 48 mm/s) over a 50-mm-distance. In a pilot experiment, we had measured the maximum velocity of the liver motion in healthy subjects during quiet breathing, and the velocities in the current experiment were chosen accordingly. A single MR acquisition run consisted of one cycle at each of the table speeds (Figure 2).
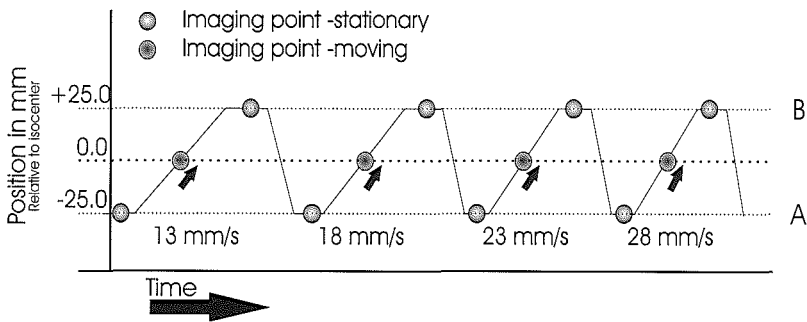
Figure 2. Schematic of programmed table positions for realtime pulse sequence controller. Here four runs (out of eight) are depicted, in which first the gel is imaged in stationary position A (bottom dotted line at -25 mm). Then the table is set in motion with a particular speed (for example 13 mm/s), and the gel is imaged as it travels through the center of the bore (central dotted line at 0 mm). Then the gel is imaged again in stationary position B (top dotted line at +25 mm). The gel is transported back to the initial position, speed is adjusted and the next cycle is ready to commence. Using this scheme, images are acquired during cooling at two stationary positions and at one position with eight different velocities.

Each cycle consisted of four parts. First, the phantom was held at position-A for two seconds, during which it was imaged. After the image was acquired, the table

was then moved 50 mm at a given linear velocity to position-B. During the motion, MR data were obtained at a single, fixed position halfway between positions-A and B. At position-B, the table was held stationary, and another MR image of the phantom was acquired. Then, the table was directed back to position-A, where, after a small pause, the next cycle commenced at the next velocity. During image acquisition, the scanner kept track of the motion and table position, to achieve central k-space traversal at the same position in the scanner for each run.

For both MR pulse sequences, we obtained the following PRF-based MR thermometry curves: (1) a thermometry curve at stationary conditions (using two baselines for the two different spatial positions), (2) one curve made up of the eight individual velocities which were referenced by a baseline image from each individual velocity (at the same spatial position), and (3) a composite thermometry curve combining all data points obtained throughout the experiment at all different velocities, referenced by three baselines (two for the stationary conditions and one for all eight velocities). Each MR thermometry curve was validated against the fiberoptic temperature measurements using ANOVA, and we compared the absolute errors in measured temperature using a one sample t-test at p=0.05 .

In-vivo baseline MR thermometry of the liver in a human subject
To assess if our technique would allow for improvement in PRF based thermometry during natural breathing, we compared the single shot EPI and the conventional FSPGR MR pulse sequences for monitoring temperature in the liver in a healthy subject under baseline free-breathing conditions (no heating). Assuming that the temperature of a given region of interest in the liver is a constant, we reasoned that all variability in measured temperature should be ascribed to artifacts of MR-thermometry. The acquisitions were not triggered to the electrocardiogram. A series of 100 consecutive complex images were acquired per sequence over a period of 2.5 minutes. Other than in the *in-vitro* set-up, it was not possible to follow the motion of the liver by recording the variations in table position. It has been shown that MR active tracking[12] can assist MR thermometry during motion.[13-14] Because we were unable to use an active tracking platform to provide the 3D position of the liver by inserted active tracking coils, as could be done in a real thermal treatment, we relied on image post-processing. The corresponding images of the liver during motion were found using an FFT-based magnitude cross-correlation in an off-line analysis to establish the 10 images that were most alike in each acquisition series. In these we calculated the standard deviation of measured temperature in the sequential time frames for a 2 cm^2 region of interest (which roughly corresponds to the achievable ablation size of the laser equipment we used) in the central part of the liver, and compared the two MR pulse sequences with respect to absolute temperature deviation from the presumed constant temperature using ANOVA at p=0.05 .

RESULTS

MR thermometry of a uniformly heated gel in static and motion conditions

In the static gel at a single position, the EPI sequence showed excellent correlation with absolute temperature over the 40-75°C temperature range with a temperature sensitivity constant (of 0.0114±0.0001 ppm/°C (r^2>0.999, Standard Error of the Estimate (SEE)=0.16°C, Figure 3).
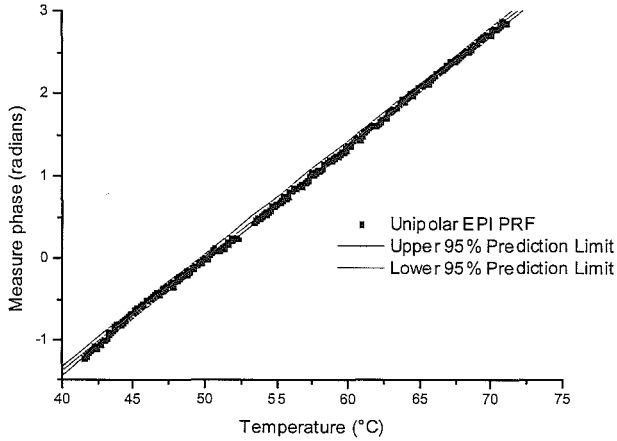

Figure 3. Temperature dependence of phase measurement in a stationary gel using the unipolar EPI sequence (temperature constant α of -0.0114±0.0001, r^2>0.999, SEE=0.16°C), with 95% prediction limits. The gap in the temperature measurements around 53°C was due to storage limitations.
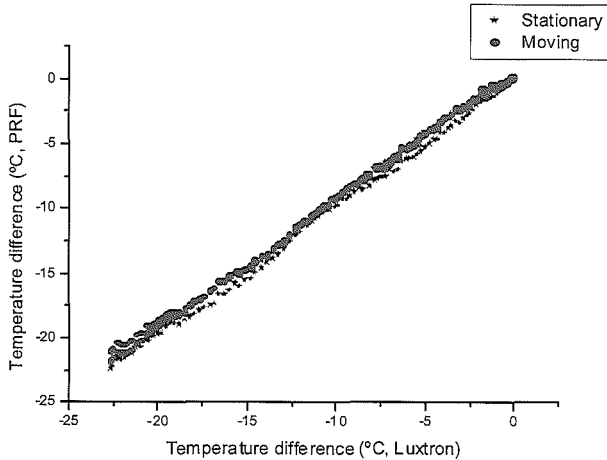
Figure 4. Validation plots are shown of PRF based MR temperature measurements under stationary conditions (star-symbol, r^2=0.997, SEE=0.37°C) and during motion (circle-symbol, r^2=0.998, SEE=0.27°C), both versus Luxtron fiberoptic temperature as gold standard, respectively.

The MR thermometry curve based on data points obtained at the two stationary positions-A and B showed excellent correlation with absolute temperature (r^2=0.997, SEE=0.37°C, range 35-60°C, Figure 4). The data showed minor transient position dependent field drifts, with negligible resultant errors in temperature quantification below ±0.4°C. Using a shifted baseline for both positions resulted in an temperature offset of almost 24°C, and increased SEE of 1.39°C. When using the multi-baseline correction for each position, the temperature offset disappeared (p<0.001). The PRF based temperature curve obtained during linear motion showed excellent correlation with the fiberoptic measurements (r^2=0.998, SEE=0.27°C, Figure 4). The MR thermometry curve combining the data points of stationary and motion conditions had slightly lower but also excellent correlation (r^2=0.996, SEE=0.41°C). These results show that 1) the proposed EPI sequence is inherently accurate for MR thermometry over the entire temperature range relevant for monitoring thermo-ablative treatment; 2) the proposed multi-baseline method significantly reduces the error associated with changes in geometrical position and 3) the proposed single echo EPI-based thermometry method was robust at linear velocity motion.

MR thermometry of a heated focal spot in a moving porcine liver

Using EPI MR thermometry, it proved possible to quantify the development of hyperthermia over time, in a region of interest in the moving liver close to the laser tip - also when combining the data from images with different baselines (Figure 5, top). The PRF shifts quantified during motion showed excellent correlation with the PRF shifts quantified under stationary conditions, r^2=0.991 (Figure 5, bottom).
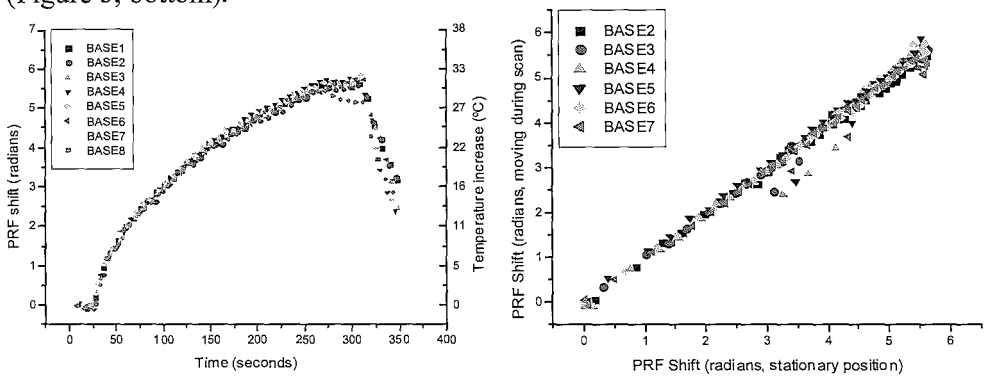
Figure 5. Based on measurements from a single pixel using all baselines, thermal history can be reconstructed (left), even in the presence of continuous motion. Linear regression of PRF-shift of single pixel during motion, versus PRF shift of the stationary condition is shown in the plot right.

The temperature uncertainty was <0.4°C, and SEE of stationary and all conditions combined were 0.3°C and 0.4°C respectively. This showed that the EPI MRI method provided accurate temperatures in a focally heated spot during motion. The EPI sequence allowed the MR imaging of a high quality thermal map (hybrid temperature-magnitude images are shown in Figure 6).
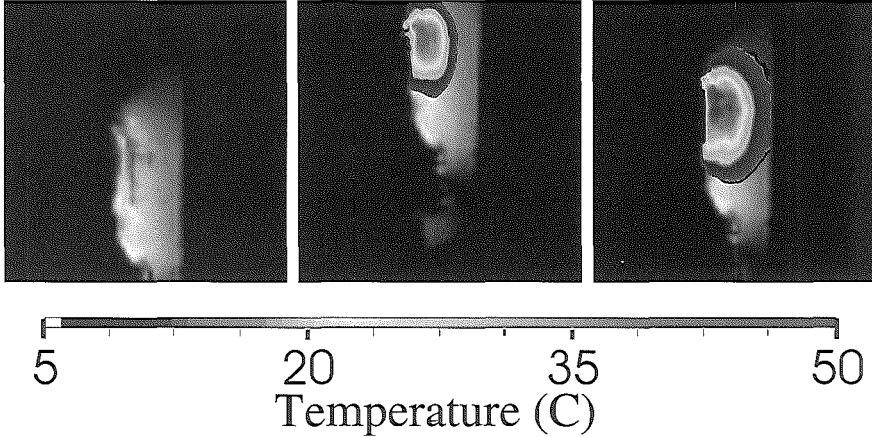

Figure 6. For three positions thermal maps are calculated based on baselines at that specific position and are projected onto the corresponding magnitude image. Background phase is masked out to improve clarity. The evolution of temperature around the laser fibre is clearly visible. (A full color version of this illustration can be found in the color section).

MR thermometry in a heated gel under varying conditions of motion

The EPI sequence showed excellent correlation between the gold standard and the MR temperature measurements during stationary conditions, as well as at the eight different velocities,
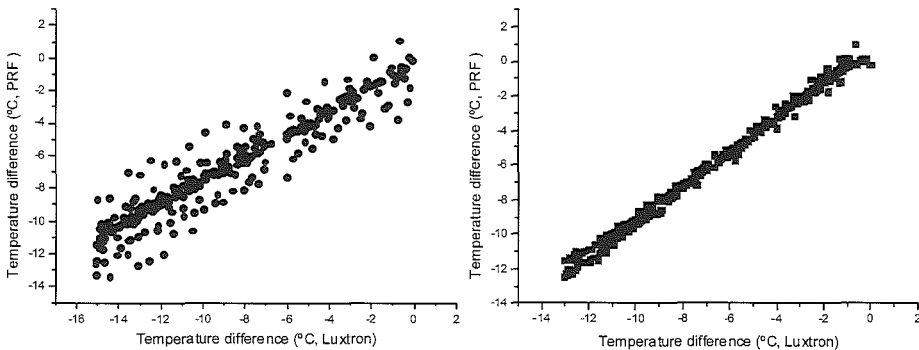
Figure 7. PRF shift of moving and stationary conditions combined (left FSPGR, right EPI) versus temperature as measured by the fiberoptic thermometer. The PRF shift is calculated using three baselines, two for the stationary conditions, and one for the moving condition, which is made up of eight different speeds. In the FSPGR, we see a large deviation in calculated temperature (r^2=0.82, SEE=1.41°C), which is much reduced in the gradient moment nulled EPI (r^2=0.996, SEE=0.25°C).

and with all data points combined (r^2=0.996, SEE=0.23°C, r^2=0.996, SEE=0.25°C and r^2=0.996, SEE=0.25°C, respectively; temperature range 48-61°C; see also Figure 7). This was different, however, for the conventional FSPGR sequence. Here, we also found good accuracy under stationary conditions and at each of the individual linear velocities (r^2=0.994, SEE=0.27°C). When combining the data points at different velocities into a single MR thermometry curve, however, the resulting accuracy was less and showed larger variability (Figure 7, r^2=0.822, SEE=1.41°C, temperature range 46-60°C).

EPI and FSPGR had similar absolute temperature deviations for the stationary and velocity compensated conditions (0.8°C versus 1.0°C, p=0.264), but when using all data from the motion experiment, the EPI sequence was significantly more accurate, with lower absolute temperature errors of 0.8°C versus 2.3°C, p<0.001 .

The difference between the two sequences was caused by a significant extra table speed-related temperature term only in the FSPGR experiments (p<0.001 versus p=0.460). These results demonstrated that the EPI sequence but not the FSPGR sequence was robust under the varying tested conditions of motion. The problems with the FSPGR sequence occur when combining data points acquired at different velocities, as would occur in actual *in-vivo* situations.
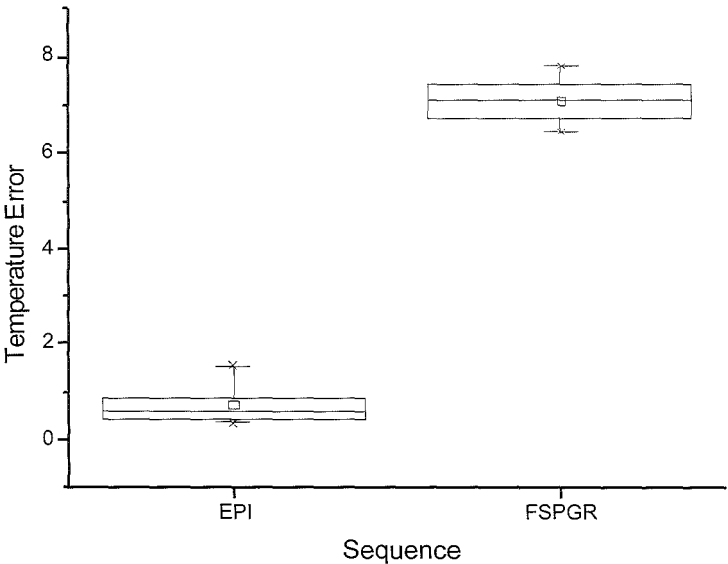
Figure 8. Mean temperature quantification errors (°C, with standard deviation) in the central region of interest in the liver of a volunteer are shown for both the EPI (left box) and FSPGR (right box) sequence. Use of EPI shows a much reduced temperature uncertainty compared to the FSPGR sequence in the free breathing experiment.

Baseline MR thermometry in a human subject

In-vivo, the EPI sequence proved significantly better than the FSPGR sequence. The variability in the (presumed constant) temperature in the liver was significantly lower for EPI, 1.6°C versus 8°C, $p<0.001$ (Figure 8).

The maximum variability in temperature per pixel during the experiment is shown in Figure 9. For EPI, this variability was low, and for FSPGR, relatively high over the entire liver region. The EPI image appeared more blurred than the image obtained with FSPGR. These results demonstrated that the EPI but not the FSPGR sequence is robust for MR thermometry *in-vivo*.
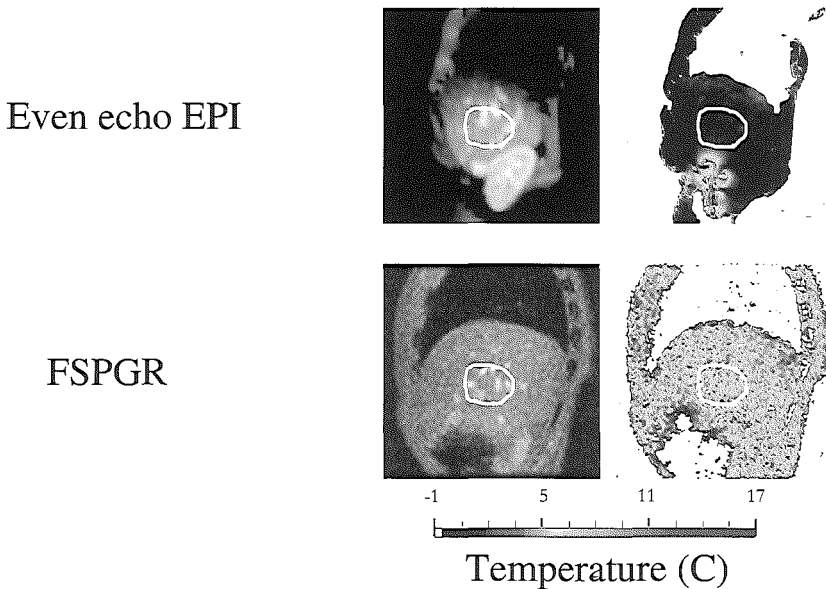
Even echo EPI

FSPGR

-1   5   11   17

Temperature (C)

Figure 9. Parasaggital images through the liver are shown to the left for both FSPGR and EPI sequences with corresponding temperature uncertainty maps to the right. We see much reduced temperature uncertainty in the liver, when using even echo echoplanar readout trains in comparison with a conventional FSPGR sequence during free breathing. In the temperature uncertainty maps, a mask was applied and values exceeding 16°C were clipped in order to improve visualization. The white border shows the defined region of interest used for comparison. (A full color version of this illustration can be found in the color section).

DISCUSSION

The current study showed that accurate PRF-based MR thermometry during motion is feasible when combining a unipolar EPI sequence with multi-baseline reference system. The temperature measurements were highly accurate under varying conditions of motion. The method appeared to be suited for *in-vivo* MR thermometry of the liver under free breathing conditions. The multi-baseline strategy corrects for extra phase shifts due to positional changes (SEE of 1.39°C

versus 0.37°C, $p<0.001$). The EPI sequence makes use of a gradient moment nulling pulse that compensates for the velocity dependent phase term along the readout direction. The EPI sequence proved significantly better than the conventional FSPGR sequence, which was subject to additional phase shifts that varied with the speed of motion (SEE of 1.41°C versus 0.27°C, $p<0.001$). Such added phase shifts make the FSPGR unreliable, especially for *in-vivo* use, as the motions of organs such as the liver are characterized by many different varying velocities with complex (non-linear) components, under conditions of free breathing.

In previous pilot studies (unpublished data) we noted temperature errors due to magnetic flux of 1.97°C (FSPGR, n=121) and 1.32°C (bipolar EPI, n=100) over a distance of approximately 1.2 cm. The magnetic flux, is however problematic to predict in practice, due to the order of complexity of the inversion of the Maxwell equations with regard to tissues of different geometry and susceptibility that surround the liver. In the present *in-vitro* study, we noted that the change in magnetic flux introduced errors that were more than 10 times larger than the velocity error over a distance of 5 cm. However, when sufficiently closely spaced baselines are available (typically within few mm of the actual position), magnetic flux becomes negligible relative to the PRF changes due to velocity.

For the proposed method to be valid, two conditions should be met. First, the position of the region of interest should be known in real time. In the *in-vitro* experiments, simply tracking the table position accomplished this, because the gel phantom was fixed to the moving tabletop. In the *in-vivo* experiment, we did not monitor the position of the liver in real-time but could only determine this afterwards in an off-line procedure. The multi-baseline method is vulnerable to through plane motion, as the heated area may not be in the imaged plane. Therefore, in patient studies, one should use an internal marker for tracking positional changes, which can control the scan plane in the appropriate dimension. Already, potentially suitable methods have been described that allow one to track the region of interest during thermo-ablative treatment. Methods of interest here make use of active tracking in real-time targeted at the laser fiber[13] or microwave probe.[14] Implementation of a real-time baseline selection is straightforward. The processing time to find the optimal baseline depends on the used metric for baseline selection, but can be within the millisecond range using MR active tracking and current workstation configurations.[13] Variable organ deformation is an additional problem, which also affects temperature measurements taken at a single location. Studies have shown that the amount of deformation may differ up to almost 20 mm in normal liver tissue. We speculate that the introduction of a fairly rigid laser or radio-frequency probe will result in much reduced tissue deformation around the thermal applicator. A logical next step would be to combine the two methods: MR thermometry by the motion robust EPI method, assisted by active MR tracking. Active MR tracking would ensure that the scan

plane holds the heated region in the field of view, while simultaneously offering a selection mechanism to find the most appropriate reference image for PRF quantification. Unfortunately, this is currently beyond the capability of the MR tracking platform provided to us by General Electric.

As a second prerequisite, the motion must be periodic in the sense that the target tissue returns to previous locations, so that appropriate baseline images are available. Fortunately, movement of organs during free breathing is intrinsically periodic. Even though the motion of the liver is primarily on the cranio-caudal direction, anterior-posterior and lateral movements need to be addressed in practice. Therefore, ideally, one should use an internal marker for tracking positional changes. By introduction of 3D monitoring of the position of the heat source the issue with regard to through plane motion can easily be resolved in real-time.

Combination of temperature data from different positions tends to average experienced magnetic field drift. In our experiment, the measured errors of the fit to the fiberoptic thermometer increased from 0.37°C, for the static conditions, to 0.41°C, while doubling the number of time samples. Using extra temperature profile information, the uncertainty in calculated thermal dose diminishes. Therefore, a tradeoff can be made whether or not to include measurements from multiple positions. With rapid high-temperature elevations, it is critical to have high temporal resolution. In the case of slow heating, it may be sufficient to use triggered acquisitions. The triggered acquisition strategy has been shown to improve temperature measurements *in-vivo*.[15]

The main limitation of the proposed methods is in the relatively limited spatial resolution, due to T_2^* decay during the readout train. This effect is also the cause of image blur in the volunteer EPI scan compared to the FSPGR scan. This may cause a problem whenever there is a steep temperature gradient in the target tissue. This shortcoming may be overcome using several approaches. Already, inner volume excitation is implemented, which, at the cost of decreased imaging efficiency, can effectively focus onto the target region. Alternatively, when using multiple receivers, parallel imaging techniques[16] can be employed to remove folding inside the field of view. Another alternative may be to use a multishot EPI scan, although error due to local magnetic field changes will increase with scan time.

In conclusion, we have shown that for a moving region of interest with periodic displacements, accurate PRF-based MR thermometry is now feasible by using the proposed method.

REFERENCES

1. De Poorter J, De Wagter C, De Deene Y, Thomsen C, Ståhlberg F, Achten E. The proton resonance frequency shift method compared with molecular diffusion for quantitative measurement of two-dimensional time-dependent temperature distribution in a phantom. J Magn Reson B 1994; 103:234-241.

2. Wlodarczyk W, Hentschel M, Wust P, et al. Comparison of four magnetic resonance methods for mapping small temperature changes. Phys Med Biol 1999; 44:607-624.

3. de Zwart JA, Vimeux FC, Delalande C, Canioni P, Moonen CT. Fast lipid-suppressed MR temperature mapping with echo-shifted gradient- echo imaging and spectral-spatial excitation. Magn Reson Med 1999; 42:53-59.

4. De Poorter J. Noninvasive MRI thermometry with the proton resonance frequency method: study of susceptibility effects. Magn Reson Med 1995; 34:359-367.

5. Heisterkamp J, Matheijssen NA, van Hillegersberg R, et al. Accuracy of MR phase mapping for temperature monitoring during interstitial laser coagulation (ILC) in the liver at rest and simulated respiration. Magn Reson Med 1999; 41:919-925.

6. de Zwart JA, Vimeux FC, Palussiere J, et al. On-line correction and visualization of motion during MRI-controlled hyperthermia. Magn Reson Med 2001; 45:128-137.

7. Wlodarczyk W, Boroschewski R, Hentschel M, Wust P, Mönich G, Felix R. Three-dimensional monitoring of small temperature changes for therapeutic hyperthermia using MR. J Magn Reson Imaging 1998; 8:165-174.

8. Peters RD, Hinks RS, Henkelman RM. Ex vivo tissue-type independence in proton-resonance frequency shift MR thermometry. Magn Reson Med 1998; 40:454-459.

9. McDannold, Hynynen K, Wolf D, Wolf G, Jolesz F. MRI evaluation of thermal ablation of tumors with focused ultrasound. J Magn Reson Imaging 1998; 8:91-100.

10. de Zwart JA, van Gelderen P, Kelly DJ, Moonen CT. Fast magnetic-resonance temperature imaging. J Magn Reson B 1996; 112:86-90.

11. Bland JM, Altman DG. Multiple significance tests: the Bonferroni method. Bmj 1995; 310:170.

12. Dumoulin CL, Souza SP, Darrow RD. Real-time position monitoring of invasive devices using magnetic resonance. Magn Reson Med 1993; 29:411-415.

13. Vogel MW, Suprijanto, Tived M, Pattynama PMT. Correction for positional errors in PRF based MR thermal maps by active tracking. ISMRM. Toronto, ON, CA, 2003. pp. 1204.

14. Morikawa S, Inubushi T, Kurumi Y, et al. New assistive devices for MR-guided microwave thermocoagulation of liver tumors. Acad Radiol 2003; 10:180-188.

15. Vigen KK, Daniel BL, Pauly JM, Butts K. Triggered, navigated, multi-baseline method for proton resonance frequency temperature mapping with respiratory motion. Magn Reson Med 2003; 50:1003-1010.

16. Pruessmann KP, Weiger M, Scheidegger MB, Boesiger P. SENSE: sensitivity encoding for fast MRI. Magn Reson Med 1999; 42:952-962.

Phase-shift based MR thermometry facilitated by MR active tracking during simulated respiration

ABSTRACT

We explored the use of an active tracking platform to correct for the displacement of tissues in real-time magnetic resonance (MR) thermometry. In an experimental setup simulating breathing motion, active tracking allowed accurate proton resonance frequency shift based MR thermometry, as validated with absolute temperature measurements with a fiberoptic temperature probe, r^2=0.99, SEE <0.1°C over a 24-67°C temperature range. Accurate temperature maps of laser-induced heating in porcine liver could be generated from the MR data obtained at different geometrical positions using MR active tracking. Thus, use of active tracking may correct for displacement of the target area during real time MR thermometry.

Mika W. Vogel, MSc ◆
Suprijanto, MSc ✳
Robert D. Darrow, MSc ●
Charles L. Dumoulin, PhD ●
Peter M.T. Pattynama, PhD, MD ◆

From
◆ The Department of
  Radiology, Erasmus MC,
  University Medical Center
  Rotterdam, The Netherlands.
✳ The Department of
  Quantitative Imaging, Delft
  University of Technology,
  Technical University Delft,
  Delft, The Netherlands.
● Global Research Center,
  General Electric,
  Schenectady, NY, USA

INTRODUCTION

Percutaneous thermal ablation of tumor tissue is gaining increasing acceptance and popularity as a patient-friendly, minimally invasive alternative to open surgical tumor resection. A key issue is monitoring the progression of treatment in real-time, to decide when the treatment is complete and should be stopped to avoid destruction of too much healthy, surrounding tissue. A particularly attractive method to monitor thermo-ablative treatment is by real-time imaging of the tissue's temperature with magnetic resonance (MR) thermometry based on the proton resonance frequency (PRF) shift.[1-2] This method has a high degree of accuracy and precision with <1.0°C error in temperature estimates.[3-4]

By measuring the PRF shift for MR thermometry, one can quantify the tissue temperature relative to an appropriate baseline image obtained at the same position. (This assures compensation of spatially variant magnetic flux and background phase). In moving organs such as the liver, however, this is fraught with difficulty. When the heated organ is displaced outside of the field of view (FOV), reliable temperature monitoring is impossible unless the scan-plane is properly adjusted. The instantaneous geometrical position of the target lesion should be exactly known to match the instantaneous thermal image with the appropriate baseline image. (As an additional problem, motion introduces extra PRF shifts in non-velocity-compensated sequences, but one can accurately correct for these extra PRF shifts by using dedicated MR acquisition schemes[5]).

Relatively few publications deal with the issue of correcting errors due to displacement.[6-8] Here, we propose the use of an MR active tracking method for this purpose. Active tracking - a method that determines instantaneously the geometrical position of one (or multiple) tracking coils in the MR magnet in real-time - has been primarily used to track the position of guide-wires and catheters in MR guided vascular interventions.[9] Conceptually, a small MR coil can be easily incorporated in the laser- or radiofrequency probe to be inserted into the target lesion for thermal ablative treatment. The position of the tracking coil can then be used to correct for the displacement of the moving target lesion in MR thermometry. In addition, the fixed position of the tracking coil inside the target lesion allows one to prescribe a moving scan plane that tracks the target lesion in real-time. In this feasibility study, we validated the use of active tracking to correct for changes in geometrical position during PRF-based MR thermometry.

MATERIAL AND METHODS

Outline of the experiments

In pilot experiments, we first studied if MR active tracking and PRF-based MR thermometry would negatively influence one another. We quantified if and how the accuracy of MR active tracking would change at higher temperatures and assessed the imaging artefacts of the active tracking coil and their potential effect on the accuracy of the PRF-shifts measurements. Next, we performed experiments

in heated gels to show the accuracy of PRF-based MR thermometry using the active tracking platform to select the appropriate baseline, thereby effectively correcting for errors due to displacement. MR thermometry was validated with a fiberoptic thermometer (model 790; Luxtron Corporation; Santa Clara, CA; accuracy ±0.2°C). Finally, we showed the use of MR active tracking to track a target lesion in an *ex-vivo* porcine liver during thermal laser ablation, to continuously image the heated focal spot during motion and to quantify its temperature.

To displace the heated gel and porcine liver in the experiments, a custom-made, automated and air-pressure driven device was used that moved along the long axis of the magnet, with a 3-degrees-upwards tilt. The motion followed a quasi-sinusoidal pattern, with plateaus in which the object was held stationary for MR imaging. The device was set to simulate a breathing rate of 12 bpm, with 1 second rest periods. The end positions of motion were 50 mm apart along the length-axis of the magnet bore and differed 2.6 mm in height.

MR imaging was done on a 1.5T system (CV/i, General Electric, Milwaukee, Wisconsin, USA, with CNV3 software, 40 mTm^{-1} gradients and 268 μs slew rate) equipped with a prototype active tracking platform.[10] The platform allows real-time switching between different pulse sequences. For tracking we used a Hadamard encoded active tracking sequence (θ/TE/TR=10°/3ms/10ms) with tracking slabs of 30 cm (24 acquired positions per second). For MR thermometry, we used an echo-shifted fast spoiled gradient echo sequence (θ/TE/TR=15°/18/12) with 1x4 mm in-plane resolution, a slice thickness of 5 mm, and a 3" surface coil.

Reconstruction of data obtained with the MR active tracking platform was performed on the MR host computer. The positional coordinates derived from active tracking and time stamps were transferred to an off-line workstation running on IDL 5.4 software, together with the raw MR thermometry data. The tracking coordinates were used to identify the stationary conditions, and PRF maps at these positions were constructed by complex subtraction of the instantaneous phase images using the appropriate baseline images, which were then converted to temperature maps.

Pilot experiments

A tracking coil catheter (Figure 1) was placed, with its long axis parallel to the B$_0$ field, in a gel phantom uniformly heated to 70°C. We recorded the variability of the registered 3D-position of the coil as provided by the active tracking platform as a function of temperature during cooling. (The actual 3D-position was a constant in this experiment). Temperatures were measured with the Luxtron fiberoptic thermometer and ranged 37-70°C, which is relevant for thermal ablative treatment. The experiment was repeated for two perpendicular orientations of the tracking coil relative to the B$_0$ field, because it is known that the signal strength for active tracking depends on such orientation.
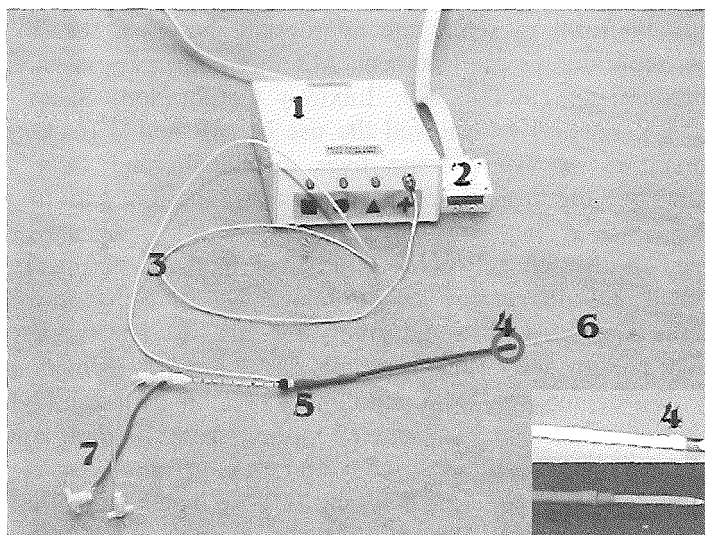
Figure 1.   Active tracking hardware, with 1) preamplifier and isolation circuit, 2) coil connector, 3) coaxial cable, 4) small copper coil, 5) insertion catheter, and 6) the diffusing tip of a 7) irrigated power laser kit. The inset shows the small copper coil in greater detail, without and with shrink wrap.

We assessed artefacts (field distortion and change in T_2^*) in the MR thermometry sequence induced by the tracking coil. These artifacts were seen at the tracking coil itself and at the laser tip of the catheter. We only assessed the worst possible orientation of the tracking coil, perpendicular to the main magnetic field and orthogonal to the read gradient.[11] The influence of artefacts of the tracking coil on the accuracy of MR thermometry was determined in another gel-cooling experiment using the fiberoptic thermometer as gold standard.

MR thermometry in moving heated gels - correction for displacement by active tracking

A tracking coil was positioned in a uniformly heated gel phantom in thermally insulating Styrofoam. During cooling, continuous interleaved MR acquisition of active tracking coordinates and MR thermometry was performed. During the experiment, the gel was moved inside the magnet bore as described above, at a frequency of 12 cycles per minute, alternating between two stationary positions, which were 50 mm apart along the long axis of the magnet, with a 2.6 mm difference in height. Based on the active tracking data, the coordinates of the stationary positions were determined, and the acquired images were converted to instantaneous temperature maps. The first image at each position served as baseline. The temperature of the gel around the tracking coil, as derived from the MR-data, was validated by using the fiberoptic Luxtron thermometer.

As a uniformly-heated gel was used in the previous experiment, potential criticism that correction for displacement may not have been critical to select the appropriate baseline image. We performed the following control analysis. Using the data from the same experiment but now disregarding the active tracking data, we calculated the temperature in a voxel with fixed geometrical coordinates (and that thus represented several different parts of the uniformly heated gel) at the time points in which the gel was held stationary, assuming no displacement. Temperature maps were calculated using only the very first baseline image. We compared the accuracy of MR thermometry using "active tracking correction" versus "no correction for displacement", by quantifying the difference in the thermal error, which is the difference between the temperatures derived from MR thermometry and the gold standard.

MR thermometry of laser ablation of moving liver tissue - correction for displacement by active tracking

We placed a laser fiber (Ø 0.8 mm, diffuser tip Lightstic™; Rare Earth Medical, West Yarmouth, MA) inside the active tracking catheter, which we then inserted into a large sample of porcine liver. An axial MR imaging plane was prescribed through the diffuser tip, and the liver was subject to simulated breatinh motion inside the magnet bore as described above. The active tracking platform was programmed to follow the defined slice. Continuous MR imaging was done, alternating the tracking sequence and the MR thermometry imaging sequences (providing at least one image and corresponding tracking coordinates per second). After having obtained the baselines scans, we started the laser ablation, whereby focal heating was induced at the diffuser tip (Dornier Medilas, Nd:YAG laser; Fibertom 5060, Dornier Medizintechnik GmbH, Germering, Germany, wavelength of 1024nm, 20W for 8 minutes). As before, the active tracking data were used to provide the two baselines at the stationary positions from which temperature maps were calculated for each baseline position individually.

MR thermometry-based temperatures were determined in a region of interest of 25 voxels around the diffuser tip of the laser. We reasoned that, if the MR-thermometry based temperatures at an individual position were correct (as proved in the previous experiments), then the temperature curve within a region of interest at one position could serve as the reference to validate the MR-based temperatures in that same region at another position (using appropriate baselines for each position), in the absence of motion effects. In the current set-up, therefore, we determined agreement between the two measurements obtained at two separate geometrical positions.[12] Additionally, to estimate bias due to non-linear temperature gradients in partial volumes, covered by the voxels in the heated region, we calculated agreement in a region of interest that remained at the reference temperature (as determined retrospectively).

RESULTS

Pilot experiments

The accuracy, expressed as the standard error of the mean for the multiple measurements obtained at a given temperature, of the tracking platform to determine the geometrical position was better than 0.015 mm when the tracking catheter was in an orthogonal orientation relative to the B_0 field and better than 0.05 mm with the tracking catheter parallel to B_0. This accuracy was not dependent on temperature nor on change in temperature.

Artefacts of the copper tracking coil resulted in field distortions near the tracking coil of 0.34 ppm at maximum and in a reduction in T_2* of about 93%. At the diffuser tip (20 mm away from the coil), no remaining effects were observed . The influence of artefacts on the thermal accuracy of PRF based thermometry were negligible. The MR thermometry data showed excellent correlation with the fiberoptic temperatures, with a temperature dependent screening constant α of 0.0107±0.001, which agrees well with the values reported in literature.[4] The residual thermal error was not significantly different (p=0.29) from that found in a control experiment without presence of the tracking coil. Thus, the pilot experiments indicated that MR active tracking and PRF-based MR thermometry did not negatively affect one another.

MR thermometry in moving heated gels - correction for displacement by active tracking

For the two stationary positions of the moving gel phantom, 75 temperature maps were generated. Regression of PRF shift in the gel versus temperature measurements by the Luxtron fiberoptic thermometer showed excellent correlation (r^2=0.99, SEE <0.1°C, temperature range=24-67°C) at both positions. No effect of position was found on the temperature sensitivity (p=0.12) or the magnitude of the residual PRF error (p=0.65).

By contrast, when the data were not corrected for displacement, i.e., when a single, fixed baseline image was used, a large temperature bias of 5.1±1.7°C was introduced, with significantly increased residual error compared to the measurement corrected using MR active tracking(0.83°C vs 10.25°C; p<0.001). The results show that PRF-based MR thermometry is accurate provided that displacement is corrected for by selection of appropriate baseline images. This was accomplished here using the active tracking platform.

MR thermometry of laser ablation of moving liver tissue - correction for displacement by active tracking

Actively tracking the focally heated spot allowed the calculation of high quality temperature maps during heating (Figure 2). Comparison of thermal profiles between temperature maps (Figure 3) obtained at the two different stationary

positions showed good correlation for PRF data in the heated region in the axial scan plane (r^2=0.99, with an SEE of 0.23°C, see Figure 2). Limits of agreement for the heated region
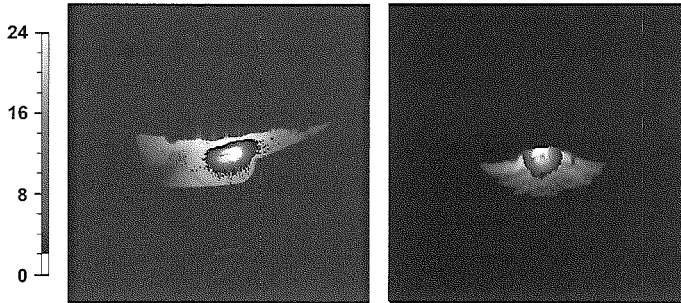

Figure 2.   Sagittal magnitude image with superimposed temperature profile (in degrees Celsius) in a sagittal high resolution scan without geometrical displacement (left) and during the real-time controlled scan at the end of the laser application with thermal image and baseline image taken at the exactly the same location (right). (A full color version of this illustration can be found in the color section).

was [-0.4°C, 3.2°C] with a mean difference of 1.4°C. In the non-heated region, we found a systematic difference of -0.9°C and limits of agreement of [-2.3°C, 0.6°C] between the two stationary positions.
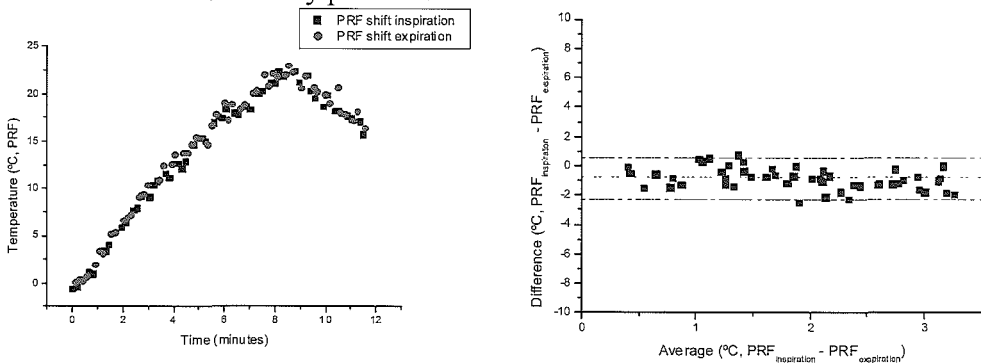
Figure 3.   PRF shift due to laser irradiation in axial images corresponds well between the two simulated end positions. In the left figure, relative PRF shift in the area near the laser fiber is plotted versus time for both positions. In the graph to the right, difference is plotted versus average of the two measurements in order to assess agreement. The dotted line indicates mean difference, and the dashed lines indicate ±2 standard deviations.

DISCUSSION

The results of the present study show that monitoring three dimensional motion in combination with MR thermometric measurements is feasible. From experimental data in gels (unpublished material), we found position dependent differences in frequency and background phase to be a major source of error for PRF-based MR thermometry. The active tracking platform enables one to keep track of the position of the thermal target, so that meaningful PRF-based temperature quantification also is possible when the region of interest will be displaced, by allowing both scan plane adjustment and selection of the appropriate baseline image. We have shown this experimentally for motion through the slice, which is currently (one of) the major factor(s) limiting the applicability of MR thermometry. We found excellent correlation of measured temperature versus PRF in the moving gel phantom. Also, agreement between the PRF measurements in the *ex-vivo* liver was approximately 1.5°C at the stationary endpoints in the moving porcine liver experiment. This agreement was reduced however in the heated region, which may be explained by partial volume effects in the thermal profile.

The motion used in this setup provided stationary positions at which the object was imaged. This was done to exclude errors in the PRF due to motion artifacts. Note that the echo-shifted FSPGR sequence used in our experiments is not particularly robust for motion effects. However, we have shown that faster imaging sequences, such as gradient moment nulled echo planar imaging,[13] will obviate this problem. Unfortunately, combination of such fast MR sequences with active tracking is currently beyond the capability of the MR tracking platform (CNV3/2003) provided to us by the manufacturer. We expect that the combination will be possible in future platforms.

The accuracy of the temperature measurements at the diffuser tip was not limited by the presence of the active tracking coil, even though the active tracking coil introduced a local field distortion. If the tracking coil is to be mounted closer to the laser tip, it may be better to use alloys that mimic tissue susceptibility such as ABI[14] or nitinol. Theoretically, a solenoid coil, when positioned parallel to the main magnetic field, will be unable to pick up any signal, preventing localization of the coil. Multiple attached coils with different orientations should forestall this issue and will greatly increase confidence in the found image position, as the SNR will be increased, and provide the ability to track rotation. Care should be taken that the active tracking coils are not co-linear, which would require modification of current laser catheters.

Previously, Morikawa et al. have demonstrated the feasibility of using optical tracking devices for MR guidance and monitoring during T_1-weighted MR thermometry.[15] However, optical tracking requires rigid devices and free line of sight, which complicates correct positioning of the thermal applicator. These conditions are resolved by the proposed active tracking scheme. Both approaches

allow monitoring of breathing patterns and allow real time adaptation of the scan plane, so that the heated profile is always in the field of view, allowing it to be referenced by an appropriate baseline. Temperature history from each reference position can be combined to improve the temporal resolution and improve accuracy of the thermal treatment effect.

In conclusion, we have shown that MR active tracking allows accurate quantification of temperature changes, by means of multiple baseline images, in objects that undergo three dimensional displacement.

REFERENCES

1. De Poorter J, De Wagter C, De Deene Y, Thomsen C, Ståhlberg F, Achten E. The proton resonance frequency shift method compared with molecular diffusion for quantitative measurement of two-dimensional time-dependent temperature distribution in a phantom. J Magn Reson B 1994; 103:234-241.
2. Ishihara Y, Calderon A, Watanabe H, Okamoto K, Suzuki Y, Kuroda K. A precise and fast temperature mapping using water proton chemical shift. Magn Reson Med 1995; 34:814-823.
3. de Zwart JA, Vimeux FC, Delalande C, Canioni P, Moonen CT. Fast lipid-suppressed MR temperature mapping with echo-shifted gradient- echo imaging and spectral-spatial excitation. Magn Reson Med 1999; 42:53-59.
4. Peters RD, Hinks RS, Henkelman RM. Ex vivo tissue-type independence in proton-resonance frequency shift MR thermometry. Magn Reson Med 1998; 40:454-459.
5. Vogel MW, Suprijanto, Pattynama PMT. Phase-shift based magnetic resonance thermometry during motion. ISMRM. Kyoto, Japan, 2004. pp. 2702.
6. de Zwart JA, Vimeux FC, Palussiere J, et al. On-line correction and visualization of motion during MRI-controlled hyperthermia. Magn Reson Med 2001; 45:128-137.
7. Vigen KK, Daniel BL, Pauly JM, Butts K. Triggered, navigated, multi-baseline method for proton resonance frequency temperature mapping with respiratory motion. Magn Reson Med 2003; 50:1003-1010.
8. Rieke V, Vigen KK, Sommer G, Daniel BL, Pauly JM, Butts K. Referenceless PRF shift thermometry. Magn Reson Med 2004; 51:1223-1231.
9. Ladd ME, Zimmermann GG, McKinnon GC, et al. Visualization of vascular guidewires using MR tracking. J Magn Reson Imaging 1998; 8:251-253.
10. Dumoulin CL, Souza SP, Darrow RD. Real-time position monitoring of invasive devices using magnetic resonance. Magn Reson Med 1993; 29:411-415.
11. Reichenbach JR, Wurdinger S, Pfleiderer SO, Kaiser WA. Comparison of artifacts produced from carbon fiber and titanium alloy needles at 1.5 T MR imaging. J Magn Reson Imaging 2000; 11:69-74.
12. Bland JM, Altman DG. Statistical methods for assessing agreement between two methods of clinical measurement. Lancet 1986; 1:307-310.
13. Duerk JL, Simonetti OP. Theoretical aspects of motion sensitivity and compensation in echo-planar imaging. J Magn Reson Imaging 1991; 1:643-650.
14. van Dijk LC, van Holten J, van Dijk BP, Matheijssen NA, Pattynama PM. A precious metal alloy for construction of MR imaging-compatible balloon-expandable vascular stents. Radiology 2001; 219:284-287.
15. Morikawa S, Inubushi T, Kurumi Y, et al. New assistive devices for MR-guided microwave thermocoagulation of liver tumors. Acad Radiol 2003; 10:180-188.

Monitoring tissue coagulation during thermo-ablative treatment by using a novel MRI contrast agent

Mika W. Vogel, MSc ♦
Cornelius A.C. Entius ♠
Peter M.T. Pattynama, PhD, MD ♦

From the Departments of
♦ Radiology and
♠ Neuroscience
Erasmus MC, University
Medical Center Rotterdam,
The Netherlands.

ABSTRACT

Introduction: We tested the feasibility of using a novel contrast agent, MS-325, as a mark er of coagulating tissue during thermo-ablative treatment.

Materials and Methods: *In-vivo*, we created coagulated lesions in porcine muscle tissue under three different conditions: MS-325 (n=5), gadolinium-DTPA (n=5) or no contrast agent (n=9) present during laser thermo-ablation. At the same time, we performed continuous T_1-weighted MR imaging at 1.5T. We quantified the change in signal intensity during treatment expressed as relative enhancement, and compared the three groups by using Mann-Whitney analysis.

Results: MS-325 resulted in a more than 3.2-fold increase in relative enhancement over the gadolinium-DTPA and non-contrast control groups ($p<0.008$).

Conclusions: MS-325 appears to be a valid marker for coagulating tissue and significantly increased relative enhancement of the treated lesions when compared to both Gd-DTPA and non-contrast enhanced conditions. MS-325 thus has potential for monitoring of thermo-ablative treatment.

INTRODUCTION

Percutaneous thermal ablation of tumor tissue is increasingly gaining acceptance and popularity as a patient friendly, minimally invasive alternative treatment to open surgical tumor resection. By focally heating the tumor up to 70°C, the tumor tissue will be necrosed by coagulation. A key issue in percutaneous thermo-ablative treatment is in monitoring the progression of coagulation in real-time, whereby it is the goal to treat the tumor in its entirety while at the same time sparing the healthy surrounding tissue. The speed of thermo-ablative therapy will vary between tissues and between patients. Therefore, it is difficult to predict when the treatment is complete. Real-time monitoring allows the physician to stop treatment as soon as tumor ablation is complete, avoiding destruction of healthy tissue.

A customary way to monitor thermo-ablative treatment is by real-time imaging of the tissue's temperature with magnetic resonance (MR) thermometry. From the MR-based temperature maps, one can then make an estimate of the extent of the treatment effect by applying theoretical models that correlate temperature (thermal dose) to heat induced tissue coagulation. A frequently used example of such a theoretical model is the Arrhenius model.[1]

MR thermometry relies on temperature-dependent changes in MR-parameters, which can be either a change in the proton resonance frequency[2] or in the T_1-relaxation time.[3-4] By principle, proton resonance frequency-based MR thermometry is the more accurate method of the two. Its use, however, is severely hampered in clinical practice by motion-induced artifacts, especially in the liver -- the organ most commonly treated with thermo-ablation. Therefore, monitoring of thermo-ablative treatment frequently uses MR thermometry based on changes in T_1-relaxation.

Although MR-thermometry based on change of signal intensity of T_1-weighted images provides temperature readings within the target lesion, its use to monitor the effect of thermal ablation has its limitations. Temperature estimates based on T_1-changes are inaccurate because the T_1-relaxation times in solid tissues are not only dependent on temperature, but also on the induced tissue damage, and hysteresis prevents quantitative MR thermometry in repeated treatments. Also, as mentioned earlier, temperature does not directly reflect tumor coagulation but can only be used to indirectly estimate tissue damage by means of theoretical calculations. Consequently, the lesion size as estimated from T_1-based MR-thermometry has been repeatedly shown to deviate from the actual lesion size.[5-7]

An alternative approach of monitoring would be to use a contrast agent during thermal ablation that would directly enhance coagulated tissue. *In-vitro* experiments with such a contrast agent, MS-325 have shown that coagulation dependent enhancement is feasible.[8] Here, we wish to report our initial experience with MS-325 *in-vivo*, performing thermal ablative treatment in experimental

animals. It was our aim to test whether the use of intravenously administered MS-325 would increase the conspicuity of the treated tissue compared to T_1-based MR thermometry, the latter being performed with and without enhancement with gadolinium-DTPA contrast.

MATERIALS AND METHODS

MS-325 contrast agent

MS-325 (EPIX Medical. Cambridge, MA) is a non-FDA approved, non-CE marked, T_1-enhancing contrast agent[9] that has been experimentally used as a blood-pool agent for MR angiography[10-14] and for the investigation of inflammatory activity.[15] MS-325 has some characteristics that are specifically relevant for the proposed use as a marker of coagulating tissue: MS-325 binds primarily to human serum albumin (HSA) and has been shown in several different animals to have a relatively long circulating half time of 2-3 hours.[16] Upon coagulation, HSA undergoes a conformational change that allows more contrast agent to bind to it.[8] Simultaneous conformational changes in MS-325 increase the relaxivity of nearby water protons, which will result in even higher signal intensity (SI) in T_1-weighted MR images.

In-vivo experiments

All animal experiments were approved by the local animal use committee.

We performed thermo-ablation of muscle tissue in 5 pigs. Two lesions were created; one before and one (in the contralateral muscle) after MS-325 contrast administration. Therefore, outside of the MR scan room, two 9F water-cooled laser probes (Somatex, Berlin, Germany) were placed, guided by palpation, in the left and right long thoracic muscles, respectively. Thermal ablation was performed by applying laser energy of $\lambda = 1064$ nm wavelength for 8 minutes $\pm$ 5 seconds at 20 Watt (Dornier Medilas, Nd:YAG laser; Fibertom 5060, Dornier Medizintechnik GmbH, Germering, Germany). The used laser fiber had a 21 mm long diffusing tip (Lightstic; Rare Earth Medical, W. Yarmouth, MA).

For MR imaging, a 3" surface coil was positioned on the skin surface and the position of the laser tip was determined by using a localizer scan. A first thermo-ablative lesion was created without using contrast agent, while continuously performing MR imaging. Then, a single bolus of MS-325 (dose 0.4 ml/kg, arbitrarily chosen) was manually injected, and at 3 minutes the second thermo-ablation treatment was started in the contralateral muscle, also while acquiring continuous MR images (see MR imaging and image analysis). It was of interest if the use of MS-325 would result in increased SI of the lesion, and also if the extent of this increase would be larger than that of the decrease in SI seen during the non-contrast-enhanced part of the experiment.

In one additional pig, we performed a sham experiment, whereby the same procedure was followed as described above, but without activation of the laser.

This control experiment was done to exclude that changes in MR images were independent of the ablation procedure.

In a second experiment using another five pigs, we followed the same procedure, but now used gadolinium-DTPA instead (Magnevist, Berlex Laboratories Inc, Wayne, NJ), at a dose of 0.4 ml/kg. This was done to compare the effect of the two contrast agents on lesion SI and resultant relative signal enhancement of the coagulated tissue. In this experiment also, the control lesion was created first to rule out contrast contamination.

MR imaging and image analysis
All MR images were acquired on a 1.5 T Signa CV/*i* scanner (General Electric, Milwaukee, Wisconsin, USA), with LX 8.4 software, 40mTm^{-1} gradients and a slew rate of 268 μs. In the *in-vivo* experiments, we used 2D SPGR (TR/TE/θ = 15.7/3.8/30°) pulse sequence to image a single slice of 5 mm thickness and a resolution of 0.94x1.88 mm^2, at a framerate of 6 images per minute. MR imaging was started 2 minutes before thermo-ablation, and continued for a period of 17 ± 3 minutes per created lesion. We acquired six images per minute of a single slice through the lesion.

Images were transferred off line to a workstation to calculate relative signal enhancement of the induced lesions. After alignment to correct for bulk motion displacements (1.4 ± 2.0 mm) between images using cross correlation, regions of interest (320 ± 48 pixels) were chosen in regions adjacent to the laser fiber. Then relative signal enhancement was determined in the regions of interest, using the baseline signal (S_{before}), which was the average of the first four images and maximal SI after the laser irradiation (S_{after}):

$$CNR \equiv \frac{S_{after} - S_{before}}{\sigma}$$

For the lesions in which MS-325 was used as the contrast agent, maximum S_{after} was defined as the maximum SI in the lesion after injection. This typically occurred at the end of the experiment as the SI showed a continuous rise towards a plateau. For the non-contrast enhanced studies and the studies in which gadolinium-DTPA was used, S_{after} was defined as the lowest SI reached during the experiment. This typically occurred at the end of the laser treatment at the time that the tissue would have the highest temperature, as the lengthening of T_1 reverses when the tissue cools down. When coagulation is induced T_1 of tissue reverses only partly after heating. A Kruskal-Wallis test was used to test for differences in relative enhancement between the MS-325, gadolinium-DTPA and "no-contrast agent" lesions. Comparisons between relative enhancement of the different groups were performed using a Mann-Whitney-U test (two tailed, exact significance calculation). Differences were deemed significant at the P=0.05 significance level.

Animals and animal handling

The experimental animals were female crossbreeds of Yorkshire pigs, weighing approximately 50 kg each. The pigs were anesthetized using azaperon (intramuscularly, 0.05 ml/kg), ketamine (intramuscularly, 10 mg/kg) and thiopental (intravenously, 10 mg/kg). Anesthesia was maintained by using a gaseous mixture of nitrous oxide and oxygen (1:2 volume) and 1.5 % of isoflurane, as well as pancuronium (intravenously, 4 mg) and fentanyl (intravenously, 0.1 mg). After the experimental procedure, pancuronium was antagonized with neostigmine (intravenously 2 ml). Two weeks after the experiments, the animals were sacrificed using an overdose euthasate. The ablated muscle tissue was excised and non-stained specimens of the lesions were compared with the MR images. The two-week margin was chosen for a qualitative comparison against true lesion size, which may be underestimated by the hyperacute lesion pattern. During the two week follow-up no adverse effects have been noticed or reported in the log book.

RESULTS

Contrast enhancement of MS-325 in-vivo

In the presence of MS-325, laser ablated muscle lesions showed a steady rise of SI towards a plateau (see Figure 1; see Figure 2 for a typical lesion).
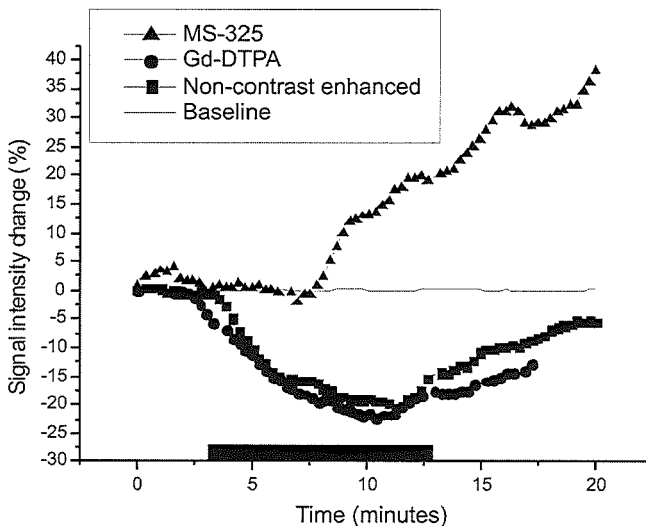
Figure 1. Typical change in signal intensity during and after the local ablation procedure in vivo. In the case of a contrast-enhanced lesion, the particular contrast (either MS-325 (triangles) or Gd-DTPA (circles)) is injected just before the start of imaging. Laser activation is within minutes after the start of the imaging session (black box in figure). The black line indicates the signal intensity change in non-heated areas. Each line represents a single pig, representative results are shown.
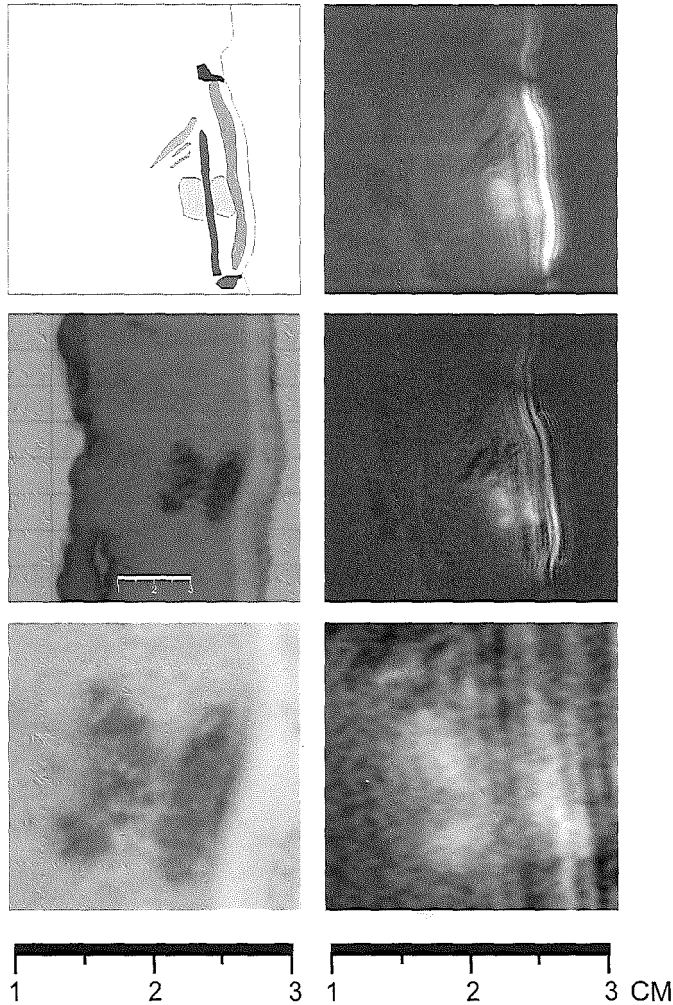
Figure 2. Schematic of the induced lesion (left top) showing laser fiber (red), induced lesion (yellow), coil shading (dark grey), skin fat layer (green), and compression due to the insertion of the laser catheter (blue). The induced tissue coagulation at the end of treatment (at 20 minutes) in muscle tissue (right, top) in the presence of MS-325. The left picture in the center row shows the induced coagulation, and to the right the subtraction image is shown. Below magnifications are provided, with the scale in centimeters to provide more detail. Typically, images showed mild motion artifacts, which increased with time in all groups. (A full color version of this illustration can be found in the color section).

Gadolinium-DTPA resulted in a decrease in SI, with a maximum magnitude occurring at the end of the heating; the SI gradually returned towards baseline

value when the heating stopped. Without contrast agent added, the laser ablated muscle lesions showed similar changes in SI as in the gadolinium-DTPA group. One measurement in the non-contrast enhanced group failed, yielding nine measurements in this group. The lesion in the sham treated animal (laser not activated), showed no changes in SI before and after "treatment".

The maximum absolute change of the signal relative to baseline SI was used to calculate relative enhancement. Lesions treated in the presence of MS-325 showed significantly larger relative signal enhancement (0.58 ± 0.24) during/after treatment than lesions treated in the presence of gadolinium-DTPA (0.17 ± 0.09; $p=0.008$); or in the lesions created without contrast agent present (0.18 ± 0.05; $p=0.001$). The relative signal enhancement in the gadolinium-group was not different from that in the non-contrast enhanced group, $p=0.77$.

After excision, coagulation was visible as a well-defined dark reddish-brown solid spot of 3.0 ± 1.5 cm diameter. In two samples did we note charred tissue along or close to the laser tract. Irregular tissue, that could have been edematous, was visible along the coagulation border. All tissue samples were inspected for coagulative necrosis. All lesions could be identified, except in the sham lesion that was "treated" without activated laser. The enhanced areas of MS-325 matched the form and sizes of the lesions as found by visual inspection of histological samples (Figure 2).

DISCUSSION

The current results indicate that the use of MS-325 during thermo-ablative treatment enhances the visibility of coagulating tissue, both during and after the therapy. The presence of MS-325 during the process of coagulation will result in an increased relative enhancement, when compared to using gadolinium-DTPA or no contrast agent at all. Even in relatively low perfused tissue as muscle, the use of MS-325 resulted in more than 3.2-fold increase in relative enhancement.

The currently proposed use of MS-325 as a marker of coagulating tissue during thermo-ablative treatment is dependent on the characteristic that it binds to HSA. In animal studies it has been shown that HSA-bound MS-325 has an extended blood half-life, between 2 and 3 hours.[16] The distribution of HSA is also favorable for monitoring thermoablation, because HSA is abundant in many extracellular fluid environments, including plasma. The contrast agent reaches tumor tissue by its vascular bed and will be present, bound to HSA in the tumor environment. Also, when administered in high dosage the unbound contrast agent rapidly distributes over the extracellular space, providing another mechanism for delivery to the target site. As the treatment advances, we speculate that MS-325 remains bound to the denatured proteins and will be "trapped" inside the coagulated tissue. The contrast agent will not be washed out from the lesion, and is therefore expected to accentuate the treated tissue with T_1-weighted MR imaging even after the treatment itself: in our experiments, the relative enhancement when using MS-325 remained high. The delayed onset of the contrast increase may be

the result of counteracting T_1-lengthening by temperature and T_1-shortening due to the thermosensitive effect of MS-325. The largest relative enhancement for MS-325 is observed after heating. The time scale of this effect needs to be determined, as the effect may remain detectable for hours or even days. On the other hand, the changes in relative enhancement in T_1-weighted images without contrast agent or when using gadolinium-DTPA were transient, because these changes primarily reflect T_1-changes due to increased temperature during treatment, which normalize upon cooling down of the tissue after treatment. Upon tissue coagulation, the T_1-relaxation time after treatment will be permanently changed. The chosen timing of start of ablation 3 minutes after contrast administration, and completion of treatment within 10 minutes ensures both complete biodistribution of the contrast agents, and is far below the halftime of both contrast agents.

We are aware of a number of experimental studies, which have proposed the use of contrast enhancing material during thermo-ablative treatment. Intravenous Gd-DTPA administration as performed in the current study typically resulted in lower SI during heating,[17] similar to our results. However, due to slow washout of already present contrast agent, contrast to noise compared to the surrounding tissue was observed,[17-18] which correlated well with contrast-enhanced follow-up. Although not the objective of our study, we were unable to replicate this finding using our current study. This may have been because of the combination of relatively high contrast dose and limited time for follow-up; during which wash out of the normal tissue occurs. Another way to mark tissue at coagulation temperature is by means of thermosensitive liposomes containing contrast agent.[19] These liposomes will burst and release the contrast agent at a certain temperature threshold. The contrast agent thus will enhance those regions where the temperature exceeds the bursting temperature of the liposomes, which has shown to be feasible to temperature thresholds up to 57°C.[20] Local release of contrast agent may be helpful in assuring that the proper target region is being treated. However the effect will reflect the threshold temperature and not the induced coagulation, and the effect will be transient as the contrast agent can be washed-out of the lesion before coagulation has occurred.

Important issues regarding the effectiveness of MS-325 for monitoring thermo-ablative treatment remain to be studied. For reliable monitoring, it is paramount that the lesion size as seen with MS-325 enhanced MR imaging corresponds to the actual size of coagulated tissue. It is uncertain, how border areas that are not fully coagulated, will enhance with MS-325. We have performed histological studies of all lesions and from visual inspection the lesion sizes and shapes did indeed correspond between MR imaging and histology. Nevertheless, our experiments were not designed to validate the MR imaging of border areas versus microscopy, due to the fairly crude MR imaging resolution. Therefore, these observations can provide crude estimates only, and further study is necessary

to show whether or not MS-325 provides accurate coagulation border definition. Other issues relate to the fact that our study provides proof of principle only, and that further optimization of the MRI pulse sequence and optimal dosage of MS-325 is necessary before the method can be applied in the human setting. Also, from our short-term experiments it is still unclear how long-lived the SI changes when using MS-325 will be, whether or not they will persist after days or even weeks.

In summary, we have demonstrated the feasibility of a tissue state dependent contrast agent as a marker of coagulating tissue *in-vivo*. We believe our results may be applicable to the usual clinical targets for thermal ablation, including but not limited to hepatocellular carcinomas and metastases in liver. Further research should focus on whether the contrast-enhanced MR images will accurately predict the size of the treated lesion.

REFERENCES

1. Sapareto SA, Dewey WC. Thermal dose determination in cancer therapy. Int J Radiat Oncol Biol Phys 1984; 10:787-800.
2. Hindman JC. Proton resonance shift of water in gas and liquid states. J Chem Phys 1966; 44:4582-4592.
3. Parker DL, Smith V, Sheldon P, Crooks LE, Fussell L. Temperature distribution measurements in two-dimensional NMR imaging. Med Phys 1983; 10:321-325.
4. Bottomley PA, Foster TH, Argersinger RE, Pfeifer LM. A review of normal tissue hydrogen NMR relaxation times and relaxation mechanisms from 1-100 MHz: dependence on tissue type, NMR frequency, temperature, species, excision, and age. Med Phys 1984; 11:425-448.
5. Pushek T, Farahani K, Saxton RE, et al. Dynamic MRI-guided interstitial laser therapy: a new technique for minimally invasive surgery. Laryngoscope 1995; 105:1245-1252.
6. Mueller-Lisse UG, Heuck AF, Thoma M, et al. Predictability of the size of laser-induced lesions in T1-Weighted MR images obtained during interstitial laser-induced thermotherapy of benign prostatic hyperplasia. J Magn Reson Imaging 1998; 8:31-39.
7. Dick EA, Wragg P, Joarder R, et al. Feasibility of abdomino-pelvic T1-weighted real-time thermal mapping of laser ablation. J Magn Reson Imaging 2003; 17:197-205.
8. Lauffer RB, Dunham SO. Contrast-enhanced diagnostic imaging method for monitoring interventional therapies. Patent Cooperation Treaty. International Patent WO 99/17809: Epix Medical Inc, 1999.
9. Mahfouz AE. Ms-325 Epix. Curr Opin Investig Drugs 2000; 1:476-480.
10. Lauffer RB, Parmelee DJ, Dunham SU, et al. MS-325: albumin-targeted contrast agent for MR angiography. Radiology 1998; 207:529-538.
11. Stuber M, Botnar RM, Danias PG, et al. Contrast agent-enhanced, free-breathing, three-dimensional coronary magnetic resonance angiography. J Magn Reson Imaging 1999; 10:790-799.

12. Prasad PV, Cannillo J, Chavez DR, et al. First-pass renal perfusion imaging using MS-325, an albumin-targeted MRI contrast agent. Invest Radiol 1999; 34:566-571.
13. Lahti KM, Lauffer RB, Chan T, Weisskoff RM. Magnetic resonance angiography at 0.3 T using MS-325. Magma 2001; 12:88-91.
14. Corot C, Violas X, Robert P, Gagneur G, Port M. Comparison of different types of blood pool agents (P792, MS325, USPIO) in a rabbit MR angiography-like protocol. Invest Radiol 2003; 38:311-319.
15. Herborn CU, Waldschuetz R, Lauenstein TC, et al. Contrast-enhanced magnetic resonance imaging (MS-325) in a murine model of systemic lupus erythematosus. Invest Radiol 2002; 37:464-469.
16. Parmelee DJ, Walovitch RC, Ouellet HS, Lauffer RB. Preclinical evaluation of the pharmacokinetics, biodistribution, and elimination of MS-325, a blood pool agent for magnetic resonance imaging. Invest Radiol 1997; 32:741-747.
17. Hynynen K, Darkazanli A, Damianou CA, Unger E, Schenck JF. The usefulness of a contrast agent and gradient-recalled acquisition in a steady-state imaging sequence for magnetic resonance imaging-guided noninvasive ultrasound surgery. Invest Radiol 1994; 29:897-903.
18. Kahn T, Harth T, Bettag M, et al. Preliminary experience with the application of gadolinium-DTPA before MR imaging-guided laser-induced interstitial thermotherapy of brain tumors. J Magn Reson Imaging 1997; 7:226-229.
19. Fossheim SL, Il'yasov KA, Hennig J, Bjornerud A. Thermosensitive paramagnetic liposomes for temperature control during MR imaging-guided hyperthermia: *in-vitro* feasibility studies. Acad Radiol 2000; 7:1107-1115.
20. McDannold N, Fossheim SL, Rasmussen H, Martin H, Vykhodtseva N, Hynynen K. Heat-activated Liposomal MR Contrast Agent: Initial *in-Vivo* Results in Rabbit Liver and Kidney. Radiology 2004; 230:743-752.

The MRI contrast agent MS-325 is an exact marker of lesion size during percutaneous radio-frequency-based thermal ablation of liver tissue

ABSTRACT

To assess a novel MRI contrast agent, MS-325, for monitoring the effect of thermo-ablative treatment, we determined how accurately MS-325-enhanced areas on T_1-weighted MRI corresponded with true lesion size as determined in histology. We created radio-frequency coagulated lesions (n=12) in porcine liver *in-vivo* after administration of intravenous MS-325. Afterwards the coagulated liver samples were imaged using high resolution MRI at 3T. The MR images were compared with histology to quantify lesion area, perimeter, and boundary definition of the coagulated lesions. There were no significant differences observed for lesion boundary, lesion area, or lesion perimeter. The 95% percentile interval of the MS-325 based border definition was within -2.3 to 4.4 mm of the histological lesion boundary.

Mika W. Vogel, MSc ◆
Thomas de Weert, MD ◆
Jan-Willem Kuiper, MD ◆
Shahid M. Hussain, PhD, MD ◆
Peter M.T. Pattynama, PhD, MD ◆

From
◆ Department of Radiology, Erasmus MC, University Medical Center Rotterdam, The Netherlands.

INTRODUCTION

Thermo-ablative treatment is gaining popularity as a minimally invasive treatment of tumors, especially in the liver. Predicting treatment effect is problematic due to uncertainty of the heat distribution in the tissue. Monitoring the treatment is therefore mandatory to completely coagulate the tumor without unnecessary damage to surrounding healthy tissue. Because of its excellent soft tissue contrast, magnetic resonance imaging (MRI) is a potential method to monitor treatment. The goal of this study is to differentiate between viable and coagulated tissue on the basis of characteristics visible with MRI.

The contrast agent, MS-325, has been reported to specifically enhance coagulated tissue.[1-2] Coagulated lesions take up the T_1-enhancing contrast agent MS-325 during coagulation and are visible as brightly enhanced lesions on T_1-weighted MRI. Enhancement of coagulated lesions was threefold more with MS-325 than with Gd-DTPA.[2] The current study determines how well the areas of MS-325 enhancement correspond to true coagulated regions as determined with histology.

MATERIALS AND METHODS

All animal experiments were approved by the local animal use committee.

Experimental design

We performed radio-frequency (RF) thermal ablations in the liver of three pigs in the presence of circulating MS-325, creating a total of 12 coagulated lesions. Control experiments were done in two additional pigs. The animals were sacrificed, and the liver specimens were imaged using *in-vitro* high resolution MRI at 3T, with 0.2 mm isotropic spatial resolution. The MR images were then compared with histology.

MS-325 contrast agent

MS-325 (EPIX Medical, Cambridge, MA) is a non-FDA approved, T_1-shortening MRI contrast agent,[3] that has been primarily used as an experimental blood pool agent for MR angiography.[3-5] MS-325 binds to human serum albumin in plasma,[4] and has a plasma half-life of 2 to 3 hours.[5] Upon denaturation of albumin during coagulation, both the affinity and relaxivity of the contrast agent will increase, so that coagulated tissue shows increased signal intensity on T_1-weighted MRI.

Thermal ablation experiments

Four RF needles (Cool-Tip™ RF-M, CTM-1530, Tyco Healthcare, Zaltbommel, The Netherlands; active tip 30 mm, 1.5 mm (17G) diameter) were placed under ultrasound guidance in the liver to create four coagulated liver lesions in each individual pig (crossbreed of Danish landrace and Yorkshire pigs, ±40kg, n=5). Care was taken that the individual lesions were spaced well apart. After MS-325

contrast administration (dose 0.4ml/kg), we created coagulated liver lesions of approximately 1.5cm in diameter in three pigs. Thermal ablation was performed by impedance control, for 8 minutes up to a maximum of 100W.

In two pigs, we performed control experiments. In one, we placed the RF needles and administered MS-325 but did not perform thermal ablation. This was done to exclude that changes in MR images could be ascribed to the sole presence of MS-325. In the other, we performed thermal ablations, but without using contrast administration. This was done to exclude that the changes in MR images independent of the presence of the contrast agent. Immediately after creation of the lesions, the animals were sacrificed, and the regions around the RF probe tip containing the coagulated lesions were excised for *in-vitro* MRI and histological analysis.

MR imaging
The freshly excised liver samples were placed in saline and scanned in a 3T MRI scanner. MRI was performed at 3.0T (VH3, General Electric, Milwaukee, WI), with M4 software, $40mTm^{-1}$ gradients and 268 μs slew rate. We used a T_1-weighted 3D FSPGR (TR/TE/θ=8.7/1.6/30°) sequence with a slice thickness of 0.2 mm and an in-plane resolution of 0.2x0.2 mm^2 in combination with a custom made small surface coil (2cm diameter, Flick Engineering Solutions Inc, Utrecht, The Netherlands). All samples were imaged in their entirety, which contained the coagulated lesion. Imaging time per specimen was 15 minutes. Images were transferred off-line to a workstation for further analysis.

Histology
After MRI, the samples were fixed in formaldehyde (3.6%). The samples were embedded in paraffin and cut into 5 μm thick histological sections using an arbitrary orientation of the cut surface. Histological sections were stained with Hematoxyline-Eosin (HE). One histological slice was used for analysis per lesion, and was photographed using a 35 mm film color scanner (super coolscan 4000 ED, Nikon, Tokyo, Japan) with 10.6 μm in-plane resolution. These photographs were used for further analysis.

Matching of MRI and histology
We compared the lesion as depicted with T_1-weighted MRI with the cut surface of the lesion as seen on the photograph of the histological slice. To this end, the MRI slice corresponding to the histological slice had to be determined. First, the images from the MR 3D volume were searched for distinctive geometrical landmarks (markers) that were prominent in the histological cut slice. These markers were based on morphology only, specifically not on the thermal lesion boundary. The markers were recorded in the three dimensional MR volume, and the cross-sectional plane through the markers was automatically established by using a least squares fit through the volume. This MRI-plane was extracted, and based on the

same markers we performed scaling in order to arrive at the same spatial scale for the two images. Then, the histological image was translated and rotated in order to achieve similar spatial orientation of MR image and histological sample.

Data analysis

Histological images were analyzed by an independent observer, who was blinded to the results of the MR examination. The outer border of the hemorrhagic zone was taken as the border of the lesion (Figure 1), as it has been shown to closely correlate with the microscopic boundary between viable and necrotic liver tissue.[6-7]

The MR images were analyzed by another independent observer, who was blinded to the results from histology. The boundary of the enhanced lesion was based on the observed signal intensity gradient, at the voxel showing the largest signal intensity change over position. The transition zone from maximally-enhanced to non-enhanced tissue was typically 0.8-1.2 mm wide. Borders were drawn manually by both observers.
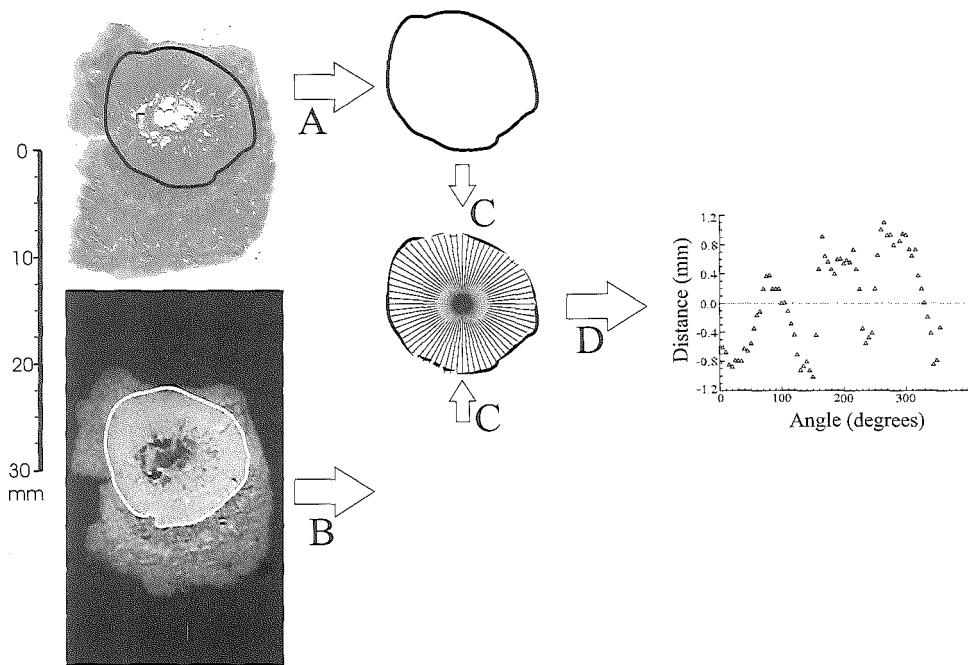
Figure 1. Schematic of the analysis. The detected lesion boundaries in histology (A) and the MR enhanced area (B) are defined. Then these are overlaid (C), and the distance between both boundaries are sampled radially. The difference in distance is shown in D as a function of sampled angle (A full color version of this illustration can be found in the color section).

The MRI- and histology-based lesion borders, were overlaid, and algorithms for boundary, perimeter and surface area were applied. The center of the lesion in the histological slice was defined by the observer and further applied as center in the MR images. To calculate mean distance between the lesion borders as defined on histology and on MRI, we applied an algorithm, where we defined, from the center of the lesion, at least 250 radii over 360°. For each radius we recorded the distance to the defined histological lesion boundary. Then we repeated the same measurement in the MR image. It was of interest to determine the mean and absolute difference between these measurements. Lesion area was taken for both histology and MR enhanced area as number of pixels contained within the defined boundaries. Perimeter length was calculated using the Euclidian distance of all boundary points. This analysis was repeated for all 12 lesions. We tested for possible differences in these parameters between MRI and histology using paired t-tests at $p=0.05$.

Animal handling
Pigs were housed for a minimum of four days in the institutional vivarium. Anaesthesia was induced using azaperon (intramuscular, 0.05 ml/kg), ketamine (intramuscular, 10 mg/kg) and thiopental (intravenous, 10 mg/kg), and maintained using a mixture of nitrous oxide and oxygen (1:2 volume) and 1.5 % isoflurane, as well as pancuronium (intravenous, 4 mg) and fentanyl (intravenous, 0.1 mg). After the experimental procedure, the animals were sacrificed using an overdose of euthasate.

RESULTS
We could identify histologically the 16 lesions in the four pigs in which we performed thermal ablation. No lesions were observed in the pig in which we had performed the sham ablation. The lesions showed marked MRI enhancement in the presence of MS-325 (Figure 1). No enhancement was detectable either in the absence of lesions or in the absence of MS-325 (control animals).

The lesion in the histological cut surface covered a mean area of 207.1±91.5 mm^2 versus 203.3±92.9 mm^2 for the enhanced area in the MR images. Pair-wise comparison of the area between the histological slice and the matched MRI image showed no significant difference (-0.27±0.66 mm^2 ($p=0.642$)).

The lesion boundaries had a length of 66.6±21.1 mm and 66.7±18.9 mm for the histological cut slice and the MR enhanced area respectively. No differences were found in these lesion perimeters between MS-325 enhanced area and histology ($p=0.919$).
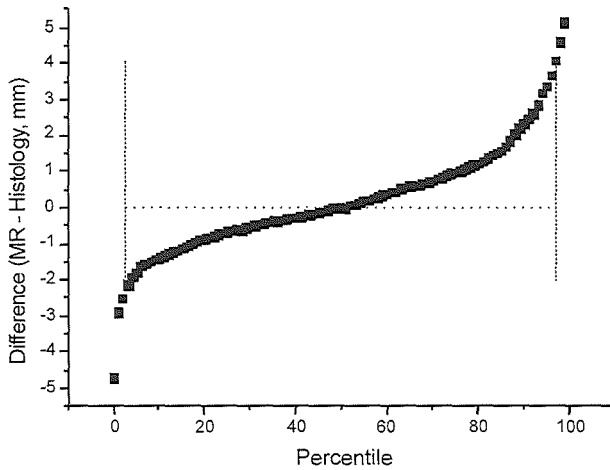
Figure 2. Percentile plot of the distance differences for all sampled datapoints from all lesions. The median is indicated by the dotted horizontal line, the dashed vertical lines indicate the 95% interval.

On a point-by-point comparison of the lesion boundary of MRI and histology, we found a median difference of 0.00 mm. The 95% percentile range of the distances between histology and MRI was from -2.29 mm to 4.39 mm (Figure 2). We found a mean absolute deviation of the point-by-point comparison between histology and MRI of 1.35±1.20 mm.

DISCUSSION

The present study demonstrates that the MS-325 enhanced liver lesions on T_1-weighted MRI correlated exactly with the coagulated tissue as determined at histology. Surface area, perimeter length, and median point-by-point difference between measurements in the histological cut slice and in the MR enhanced image were almost identical. Boundary agreement was within -2.3 to 4.4 mm for 95% of all sampled data points. The presented data shows that MS-325 enhancement is a reliable marker of coagulation and that it allows reliable definition of the borderline between coagulated and non-coagulated liver tissue.

An alternative to the use of MS-325 is using temperature measurements to monitor the progress of treatment. For accurate thermal damage estimation, one can rely on MR thermometry. Due to the non-linear interaction of heating and treatment time, accurate prediction of coagulation places stringent demands on the thermal accuracy and on both spatial and temporal resolution, which need to match the thermal response of the tissue. The use of thermosensitive liposomes has also been proposed.[8] An *in-vivo* study in rabbits has shown this mechanism to accurately indicate lesion boundary in the liver. However, this technique has yet

failed to reliable demarcate thermal coagulation lesion borders in the kidney due to wash-out. We speculate that the MS-325 method may have more potential for lesion definition in the kidney, because MS-325 is bound to coagulated tissue and therefore should not experience wash-out.

If MS-325 persists in coagulated tissue, it might interfere with MRI-based contrast-enhanced post-treatment follow up, in which the treated area is inspected for viable remnant tumor. However most information about tumors is gathered from dynamic contrast enhanced series. The processing of such data implies inherent compensation of background signal intensity levels, in order to calculate wash-in, time-to-peak and wash-out parameters. Therefore, we believe that the use of MS-325 to monitor thermal ablation will not preclude post treatment evaluation of remnant tumor tissue.

The proposed use of MS-325 is particularly apt when a steep temperature gradient is induced by the thermal applicator, as in the hyperacute lesions we used in this study. When apoptosis is induced by prolonged heating at relatively low temperature (<50°C),[9] denaturation may not occur and MS-325 may thus give an underestimation of lesion size. We did not test this. We speculate that the breadth of the transition zone of the MS-325 enhanced area may be indicative of such zones of milder heating due to a temperature gradient. In our high-power ablation experiments, we found this gradient to be around 1.0 mm.

We conclude that the present study demonstrates that the MRI contrast agent MS-325 appears to be an accurate marker of coagulation during tissue ablation.

REFERENCES

1. Lauffer RB, Dunham SO. Contrast-enhanced diagnostic imaging method for monitoring interventional therapies. Patent Cooperation Treaty. International Patent WO 99/17809: Epix Medical Inc, 1999.
2. Vogel MW, Entius C, Pattynama PMT. Monitoring tissue coagulation during thermo-ablative treatment by using a novel MRI contrast agent. Invest Radiol 2004, in press.
3. Mahfouz AE. Ms-325 Epix. Curr Opin Investig Drugs 2000; 1:476-480.
4. Caravan P, Cloutier NJ, Greenfield MT, et al. The interaction of MS-325 with human serum albumin and its effect on proton relaxation rates. J Am Chem Soc 2002; 124:3152-3162.
5. Parmelee DJ, Walovitch RC, Ouellet HS, Lauffer RB. Preclinical evaluation of the pharmacokinetics, biodistribution, and elimination of MS-325, a blood pool agent for magnetic resonance imaging. Invest Radiol 1997; 32:741-747.
6. Germer CT, Albrecht D, Roggan A, Isbert C, Buhr HJ. Experimental study of laparoscopic laser-induced thermotherapy for liver tumours. Br J Surg 1997; 84:317-320.
7. Scudamore CH, Lee SI, Patterson EJ, et al. Radiofrequency ablation followed by resection of malignant liver tumors. Am J Surg 1999; 177:411-417.
8. McDannold N, Fossheim SL, Rasmussen H, Martin H, Vykhodtseva N, Hynynen K. Heat-activated Liposomal MR Contrast Agent: Initial in Vivo Results in Rabbit Liver and Kidney. Radiology 2004; 230:743-752.
9. Sapareto SA, Dewey WC. Thermal dose determination in cancer therapy. Int J Radiat Oncol Biol Phys 1984; 10:787-800.

.

Summary and Prospects
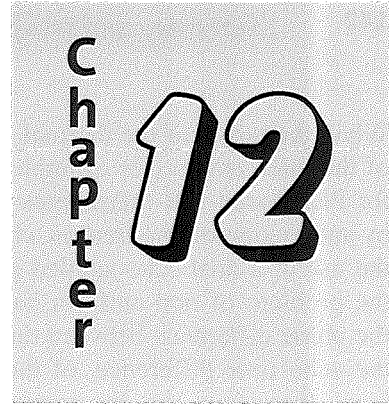
SUMMARY

Magnetic resonance (MR) thermometry is a promising technology for non-invasive monitoring of (locally) induced temperature changes. Several different MR imaging methods have been proposed in literature, to maximize the effect of intrinsic temperature dependent parameters, and thereby maximize contrast in the acquired MR images. Upon review of these different methods, and their applications (**Chapter 1**), two methods are found potentially applicable: one based on spin-lattice (T_1) relaxation and one based on proton resonance frequency (PRF) shift. In **Chapter 2** these two methods are compared at different field strengths to determine sensitivity, precision, and relative performance. The PRF method was found to be more accurate then the T_1 method. Both methods demonstrated tissue dependent temperature constants, although the deviation in temperature constants was smaller for the PRF method. The PRF method, however, is sensitive to aliasing during rapid heating, such as radiofrequency (RF) ablation at high field strength (**Chapter 3**). This aliasing artifact can be effectively removed by dedicated phase unwrapping routines. In addition, RF ablation using currently available needles gives rise to additional artifacts that reduces the maximum obtainable accuracy with the PRF method. A potential alternative to current RF needles is ABI, a material with tissue mimicking magnetic susceptibility. The use of ABI reduced the extent of observed artifacts (**Chapter 4**). These artifacts are more pronounced when using gradient echo sequences with long echotimes, which are commonly used for PRF based MR thermometry. Possibly, the extent of such artifacts could be further reduced using special, PRF sensitized, Fast Spin Echo sequences. In **Chapter 5**, an implementation of a single-shot (SS) non-Carr Purcell Meiboom Gill (CPMG) FSE sequence to measure the PRF shift is described. Using such a SS FSE sequence could be beneficial for MR thermometry because of its typical high signal-to-noise ratio (SNR), reduced sensitivity to T_2^*, and high acquisition speed. With the described non-CPMG SS FSE we confirmed the influence of the PRF sensitization time ? on precision of the calculated temperature sensitivity constant. In addition, the capability of the non-CPMG SS FSE sequence to perform thermal mapping was shown during local heating in a gel, using laser.

When the target of the thermal intervention changes position over the time course of the intervention (for example a liver in the respiratory cycle), a problem occurs for PRF based MR thermometry: the background phase that is typically removed by subtraction of two images, changes with position. In **Chapter 6** we investigated the use of a dual echo spoiled gradient echo sequence, in an attempt to overcome the problem of non-uniform background phase of the MR signal. Calculation of the phase difference between the two subsequent echoes allows computation, from the echo time difference, of the local frequency at each pixel in the image. The local frequency can be converted to temperature using the proton resonance frequency shift. This makes temperature quantification insensitive to the value of the background phase at each particular position. A complication was that the range of local frequencies was far higher than those expected from temperature-related proton resonance frequency shift. Therefore a frequency reference image is required for temperature quantification.

The problem of changed background phase in a displaced target object was further explored in **Chapter 7**. Here, a processing scheme, the multi-baseline method, is proposed which searches for an appropriate reference image for each encountered displaced position. Motion during image acquisition leads to image artifacts. Such affected images were automatically removed from the thermal map calculation. The multi-baseline method used target object coordinates obtained by MR active tracking (see also Chapter 9). Using the proposed processing scheme, it was shown feasible to improve thermal precision from approximately 6°C to 1.2°C, with over 68% efficiency. The possibility to use images from multiple locations increased temporal resolution. This would allow more accurate thermal dose determination.

Temperature measurement in continuous moving objects was so far not successfully demonstrated. Therefore, we studied the effect of continuous motion on the acquired thermal maps (**Chapter 8**). For this purpose a conventional single shot (SS) echo planar imaging (EPI) sequence was modified into a linear velocity compensated SS EPI sequence, and compared to a typically used conventional gradient echo sequence. Due to the absence of motion artifacts and increased thermal precision the proposed SS EPI was judged superior to the conventional gradient echo sequence. The applicability of the sequence was demonstrated by MR thermometry of local laser heating in a continuously moving ex-vivo porcine liver. The multi-baseline technique was used to compensate for background phase changes.

In **Chapter 9** the utility of MR active tracking for PRF based MR thermometry is described. MR active tracking enables the determination of the three dimensional position of a tracking coil. For the experiments a laser catheter with such a

tracking coil was prepared. From a number of experiments it was concluded that the presence of the tracking coil did not deteriorate the thermal accuracy of the PRF based measurements in the laser area. We used the MR active tracking data in an experiment, in which motion of an ex-vivo porcine liver was perpendicular to the slice selection, to update the slice position in realtime. Thereby it was possible to keep the local heating by the laser in the field of view, and compensate for background phase changes using the multi-baseline method.

The use of a novel contrast agent for detection of thermal coagulation is introduced in **Chapter 10**. With MS-325 it is shown feasible to significantly increase relative enhancement, with respect to non-contrast-enhanced or GdDTPA enhanced conditions, in muscle that undergoes laser ablation therapy. Qualitatively, the enhanced areas matched size and shape of the lesion, as determined in macroscopic morphological slices. In **Chapter 11**, a one-to-one comparison was performed to determine the relationship between relative enhancement, and acute lesion size. For this purpose, MS-325-enhanced ablated liver tissue was scanned with high spatial resolution, and compared to histological slides. After registration, lesion borders were determined in both MR image and histological slide, and absolute distance was calculated. The median distance difference was 0.0, and the width of the transition zone from ablated to normal tissue was estimated on 1.0 mm. The range of differences in distances of the lesion borders was within -2.3 to 4.4 mm for 95% of all datapoints.

PROSPECTS

In this thesis several different approaches have been described to monitor locally induced hyperthermia. The potential usefulness of each of these approaches has been demonstrated in a particular experimental setup. Therefore, sometimes there may have been negligence with regard to particular details that may impact the overall utility of the proposed approaches in the actual clinical setting.

Throughout this thesis the PRF method has been frequently used for quantification of temperature changes. In doing so, the effect of mass volume susceptibility has been ignored. The extent to which this effect interferes with the PRF method is dependent on orientation, geometry and extent of local heat deposition. This effect accounts for up to 10% of the PRF effect. Correction schemes for this effect have been presented[1-2] and can be employed under the assumption of some tissue characteristics and temperature distribution. Another cause for reduction of PRF accuracy is the (temperature-dependent) change in electrical conductivity of heated tissue.[3] This effect can be removed by using multi-echo sequences, such as the ones used in Chapters 2 and 6. The phase unwrapping routine, as introduced in Chapter 3, improves the reliability of the calculation of temperature changes based on the PRF method. This phase unwrapping routine could possibly be further improved by using optimal quality maps.

Use of fast MR sequences, such as the proposed SS sequences described in Chapters 5 and 8 are necessary for an accurate estimate of the effect on the tissue when exposed to rapid temperature changes. Using new MR technology could significantly increase the current temporal resolution of these sequences. On the one hand, the use of coil-arrays combined with reconstruction schemes as SMASH[4], GRAPPA[5] or SENSE[6] leads to a reduction in echotrain length of the proposed sequences. This is beneficial because it allows higher temporal resolution and reduces the point-spread function. The latter yields more accurate thermometric measurements. The synergy of high field MR with increasing efficiency of parallel imaging[7] offers potentially, in the scope of increased sensitivity of the PRF method at high field, the possibility of acquiring real-time isotropic volumetric acquisition of the target object of the thermal intervention. On the other hand one could employ a coil array, given that it is capable of parallel transmit,[8-9] to reduce the field-of-view even further, with associated speedup of the imaging process.

Artifacts as a consequence of the mismatch in magnetic susceptibility of RF needles and the interference of RF generators currently largely precludes use of MR controlled RF ablation. Application of filtering techniques on the RF signal, as proposed by Oshiro et al,[10] and use of alloys, that have a tissue mimicking magnetic susceptibility, offers possibilities of both accurate MR guided RF needle insertion into the target region for local hyperthermia, and improved MR thermometric feedback during the RF ablation.

Even though tissue heating as a consequence of resonating RF waves through the wires of the MR active tracking system is of marginal consequence for local hyperthermia application, it hinders the acceptance of MR active tracking in general, for example for the purpose of MR active tracking guided insertion of catheters. Safety aspects regarding the E-fields as a consequence of standing RF waves[11] on the wires of the MR active tracking system are thus an opportunity for improvement. Approaches such as optic signal transmission have been proposed. Alternatively one could try to minimize the effect of the standing waves. For minimization, different approaches would be feasible, including local excitation and varying impedance of the system during excitation.

With regard to the experiments with the contrast agent MS-325 (Chapters 10 and 11) that evaluated the effect of local hyperthermia it should be stressed that there have been no attempts to optimize contrast agent dosage, time between injection and ablation, or used sequence. Knowledge with regard to the underlying dynamics for the enhancement of coagulated tissue, in combination with possible remaining tissue perfusion, will enable a better assessment of the actual acute, and maybe even long term, effects of the local thermal intervention.

REFERENCES

1. Salomir, R., et al. Temperature-induced Changes in Magnetic Susceptibility in Local Hyperthermia: Correction of MR Thermometry. in ISMRM. 2000. Denver, Colorado.
2. Stollberger, R., et al., Temperature monitoring of interstitial thermal tissue coagulation using MR phase images. J Magn Reson Imaging, 1998. 8(1): p. 188-96.
3. Peters, R.D. and R.M. Henkelman, Proton-resonance frequency shift MR thermometry is affected by changes in the electrical conductivity of tissue. Magn Reson Med, 2000. 43(1): p. 62-71.
4. Sodickson, D.K. and W.J. Manning, Simultaneous acquisition of spatial harmonics (SMASH): fast imaging with radiofrequency coil arrays. Magn Reson Med, 1997. 38(4): p. 591-603.
5. Griswold, M.A., et al., Generalized autocalibrating partially parallel acquisitions (GRAPPA). Magn Reson Med, 2002. 47(6): p. 1202-10.
6. Pruessmann, K.P., et al., SENSE: sensitivity encoding for fast MRI. Magn Reson Med, 1999. 42(5): p. 952-62.
7. Wiesinger, F., P. Boesiger, and K.P. Pruessmann, Electrodynamics and ultimate SNR in parallel MR imaging. Magn Reson Med, 2004. 52(2): p. 376-90.
8. Katscher, U., et al., Transmit SENSE. Magn Reson Med, 2003. 49(1): p. 144-50.
9. Zhu, Y., Parallel excitation with an array of transmit coils. Magn Reson Med, 2004. 51(4): p. 775-84.
10. Oshiro, T., et al., Reduction of electronic noise from radiofrequency generator during radiofrequency ablation in interventional MRI. J Comput Assist Tomogr, 2002. 26(2): p. 308-16.
11. Konings, M.K., et al., Heating around intravascular guidewires by resonating RF waves. J Magn Reson Imaging, 2000. 12(1): p. 79-85.

Samenvatting en Vooruitblik

SAMENVATTING

Magnetische Resonantie (MR) thermometrie is een veelbelovende techniek voor het niet-invasief monitoren van (lokaal) geïnduceerde temperatuursveranderingen. In de literatuur zijn een aantal verschillende MR imaging methoden beschreven, die het effect maximaliseren van intrinsieke temperatuursafhankelijke parameters, en zo contrast creëren in de verkregen MR beelden Bij nadere beschouwing van deze verschillende methoden en hun toepassingen (**Hoofdstuk 1**) blijken twee methoden meer geschikt dan andere: een gebaseerd op de longitudinale relaxatie (T_1) en een op basis van de proton resonance frequency (PRF) shift. In **Hoofdstuk 2** worden deze twee methoden vergeleken bij verschillende veldsterkten om sensitiviteit, precisie en relatieve verhouding te bepalen. De PRF methode presteerde consequent beter dan de T_1 methode. Beide methoden vertoonden weefselafhankelijke temperatuurafhankelijkheid, hoewel de spreiding in de temperatuurafhankelijkheid geringer was bij de PRF methode. De PRF methode is echter gevoelig voor aliasing tijdens snelle verhitting, zoals tijdens radiofrequente (RF) ablatie in een hoogveld magneet (**Hoofdstuk 3**). Deze aliasing kan effectief worden gecorrigeerd door toepassing van gespecialiseerde fasecorrectie technieken. Daarbij komt dat RF ablatie met de huidige generatie RF naalden aanleiding geeft tot extra artefacten die de maximaal haalbare precisie van de PRF methode beperken. Een mogelijk alternatief voor de huidige RF naalden is ABI, een materiaal met weefsel-gelijkende magnetische eigenschappen. Het gebruik van ABI reduceerde de waargenomen artefacten (**Hoofdstuk 4**). Deze zijn sterker aanwezig bij gebruik van gradient echo sequenties met lange echotijden, die normaliter worden ingezet voor PRF gebaseerde MR thermometrie. Mogelijk zouden dergelijke artefacten verder gereduceerd kunnen worden met behulp van speciale, PRF gesensitiseerde, Fast Spin Echo (FSE) sequenties. In **Hoofdstuk 5** wordt een implementatie beschreven van een single-shot (SS) non-Carr Purcell Meiboom Gill (CPMG) FSE sequentie voor het meten van de PRF. Gebruikmaking van een dergelijke SS FSE sequentie is een potentiële verbetering van MR thermometrie vanwege de typische hoge signaal-over-ruis ratio (SNR), beperktere T_2^* gevoeligheid en snelle acquisitietijd. Met behulp van de beschreven

non-CPMG SS FSE bevestigden we de invloed van de PRF sensitisatie tijd τ op de precisie van de temperatuurmetingen. Bovendien werd de mogelijkheid gedemonstreerd met behulp van de non-CPMG SS FSE sequentie thermische kaarten te genereren tijdens lokale verhitting in een gel door middel van laser.

Wanneer het doelobject van de thermische interventie van positie verandert gedurende de interventie (bijvoorbeeld een lever tijdens de ademhalingscyclus) treedt een probleem op voor PRF gebaseerde thermometrie: de nul-fase van elke pixel, die normaliter wordt geëlimineerd door subtractie van twee beelden, verandert met positie. In **Hoofdstuk 6** onderzochten we de bruikbaarheid van een dubbel echo spoiled gradient echo sequentie om het probleem van veranderende nul-fase van het MR signaal te verhelpen. Berekening van het faseverschil tussen de opeenvolgende echo's, in combinatie met het verschil in echotijd, biedt de mogelijkheid locale frequentie te bepalen voor iedere pixel in het beeld. Deze locale frequentie is kwantificeerbaar als PRF shift. Dit maakt de temperatuur quantificatie onafhankelijk van de nul-fase. Een complicatie vormde het bereik van berekende locale frequenties: deze waren veel hoger dan de te verwachten PRF shift. Mede daarom blijft een referentiebeeld noodzakelijk.

Het probleem van de veranderende nul-fase door verandering van positie van het doelobject is verder onderzocht in **Hoofdstuk 7**. Een schema, de multi-baseline methode, wordt hierin beschreven dat, voor iedere waargenomen positie van het doelobject, zoekt naar een referentiebeeld. Beweging van het doelobject tijdens de beeldacquisitie leidt tot artefacten in het beeld. Dergelijke beelden met bewegingsartefacten werden automatisch verwijderd en dus niet meegenomen in de berekening van de thermische kaarten. De multi-baseline methode maakte gebruik van de ruimtelijke coördinaten van het doelobject, die werden verkregen met behulp van MR actieve tracking (zie ook Hoofdstuk 9). Met de voorgestelde aanpak was het mogelijk om de spreiding van de temperatuurmetingen te reduceren van ongeveer 6°C naar 1.2°C, met een efficiëntie van meer dan 68%. De mogelijkheid de beelden van de verschillende posities waarin het doelobject zich bevond te combineren verhoogt de temporele resolutie. Dit maakt een nauwkeuriger schatting mogelijk van de zogenaamde thermische dosis.

Nog niet eerder werd gedemonstreerd dat temperatuurmetingen in continue bewegende doelobjecten succesvol uitgevoerd kunnen worden. Daarom werd in **Hoofdstuk 8** het effect van continue beweging op de berekende thermische kaarten bestudeerd. We creëerden uit een conventionele SS echo planar imaging (EPI) sequentie een SS EPI sequentie voorzien van een intrinsieke compensatie voor beweging met een constante snelheid. Deze sequentie werd vergeleken met de conventionele spoiled gradient echo sequentie, die meestal wordt gebruikt voor MR thermometrie. Door afwezigheid van bewegingsartefacten en verhoogde

thermische precisie, was de gecreëerde SS EPI superieur aan de conventionele spoiled gradient echo sequentie. De bruikbaarheid van de techniek werd gedemonstreerd in een laser experiment in een continu bewegende ex-vivo varkenslever. Met de multi-baseline methode werd de verandering in nul-fase gecompenseerd.

In **Hoofdstuk 9** wordt de bruikbaarheid van MR actieve tracking voor PRF gebaseerde MR thermometrie beschreven. Met behulp van MR actieve tracking is het mogelijk de drie dimensionale positie te bepalen van een tracking coil. Voor de experimenten in dit hoofdstuk monteerden we een dergelijke tracking coil op een laser catheter. Door middel van een aantal experimenten werd bepaald dat de aanwezigheid van de tracking coil geen verslechtering van de thermische precisie van de PRF methode veroorzaakte in de nabijheid van deze tracking coil. Tijdens continue beweging van een ex-vivo lever, loodrecht op de geselecteerde slice, maakten we gebruik van de positionele informatie van de tracking coil. Het bleek mogelijk op basis van de positionele informatie van de tracking coil de slice positie in realtime te veranderen, zodat de lokale verhitting door de laser in het beeld aanwezig bleef, en quantificeerbaar was met behulp van de PRF methode. Voor correctie van de nul-fase gebruikten we wederom de multi-baseline methode.

Het gebruik van een nieuw contrastmiddel voor de detectie van thermische coagulatie werd geïntroduceerd in **Hoofdstuk 10**. Met MS-325 was de mate van aankleuring (uitgedrukt als relatieve signaalversterking) in spierweefsel dat thermische ablatie onderging significant verbeterd ten opzichte van de twee controle condities: zonder contrastmiddel, en met Gadolinium-DTPA. Een kwalitatieve beoordeling van de grootte en vorm van het aangekleurde weefsel kwam overeen met die van de toegebrachte laesie, zoals waargenomen in macroscopische morfologische plakken. In **Hoofdstuk 11** is een een-op-een vergelijking gemaakt om de relatie te bepalen tussen aankleuring en feitelijk acute laesie. Daartoe werd door MS-325 aangekleurd geableerd varkensleverweefsel met hoge spatiele resolutie gescand, en vergeleken met histologische coupes. Na registratie van de beelden werden de randen van de laesie bepaald in zowel MR beeld en histologische coupe, en werd de afstand hiertussen berekend. De mediaan van deze afstand was 0.0mm, de breedte van de transitie zone werd geschat op ca. 1.0 mm. De totale range van verschil in afstand tussen de twee laesie randen was van −2.3 tot 4.4 mm voor 95% van de totale data.

VOORUITBLIK

In dit proefschrift zijn verschillende methoden beschreven voor het monitoren van lokaal geïnduceerde hyperthermie. De potentiële bruikbaarheid van elk van deze methoden is gedemonstreerd in een specifieke experimentele opstelling. Daarbij is soms een aantal details buiten beschouwing gelaten, die mogelijk in de klinische

praktijk een effect zouden kunnen hebben op de toepasbaarheid van de voorgestelde methoden.

In dit proefschrift is veelvuldig gebruik gemaakt van de PRF methode voor quantificatie van temperatuursveranderingen. Daarbij is het effect van de volume magnetische susceptibiliteit verwaarloosd. De mate waarin dit effect de PRF beïnvloedt is afhankelijk van oriëntatie, geometrie en mate van de locale verhitting. Dit effect is maximaal circa 10% van het PRF effect. De correctie hiervoor is reeds beschreven[1-2] en kan worden geschat wanneer men bereid is enkele aannames te doen met betrekking tot weefseleigenschappen en vorm van temperatuurdistributie. Een andere factor die de accuratesse van de PRF metingen negatief beïnvloedt is (temperatuursafhankelijke) verandering van de elektrische geleidbaarheid van het verhitte weefsel.[3] Correctie voor dit effect is mogelijk door eliminatie van de nul-fase, bijvoorbeeld door de multi-echo sequenties zoals beschreven in de Hoofdstukken 2 en 6. De phase unwrapping methode, voorgesteld in Hoofdstuk 3, verhoogt de betrouwbaarheid van de berekening van temperatuur op basis van de PRF methode. De phase unwrapping methode kan mogelijkerwijs verder verbeterd worden door optimale kwaliteitskaarten.

Toepassing van snelle MR sequenties, zoals de SS sequenties die zijn beschreven in de Hoofstukken 5 en 8 zijn noodzakelijk voor een accurate inschatting van het effect van snelle temperatuursveranderingen op het weefsel, met name wanneer men gebruik maakt van het concept thermische dosis. Echter, de temporele resolutie van deze sequenties kan substantieel worden verhoogd door gebruikmaking van nieuwe MRI technologie. Enerzijds kan door middel van coil-arrays in combinatie met reconstructie schema's zoals SMASH[4], GRAPPA[5] of SENSE[6] een reductie worden bewerkstelligd in de duur van de echotreinen van zulke sequenties. Dit heeft twee grote voordelen: toename van de temporele resolutie en afname van de point spread functie. Dit laatste draagt bij aan een verhoogde nauwkeurigheid van de temperatuurmeting per pixel. De synergie van hoogveld systemen met toenemende efficiëntie van parallelle beeldvorming[7] biedt potentieel, in de context van de toegenomen sensitiviteit van de PRF bij hogere veldsterkte, de mogelijkheid tot real-time isotrope volumetrische acquisitie van het doelgebied van de thermische interventie. Anderzijds kan met behulp van dergelijke coil-arrays, wanneer deze geschikt zijn gemaakt voor parallelle excitatie,[8-9] het field-of-view verder gereduceerd worden, met navenante toename in maximale temporele resolutie.

Artefacten als gevolg van de mismatch in magnetische susceptibiliteit van RF naalden en de interferentie van RF generatoren sluit momenteel gebruik van MR gecontroleerde RF ablatie grotendeels uit. Toepassing van RF filtertechnieken op de RF generator zoals besproken door onder meer Oshiro et al,[10] en toepassing van

legeringen met weefselgelijkende magnetische susceptibiliteit zoals beschreven in Hoofdstuk 4, mogelijkerwijs in combinatie met MR actieve tracking, bieden mogelijkheden tot verhoogde controle op MR geleide insertie van zulke naalden in het doelgebied voor de thermische interventie en betere MR thermometrische feedback tijdens de RF ablatie.

Hoewel in relatie tot locale hyperthermie, weefselverhitting als gevolg van resonerende RF golven over de signaaldraden van een MR actieve tracking systeem een verwaarloosbaar onderwerp is, verhindert het de algemene acceptatie van MR actieve tracking voor bijvoorbeeld MR actieve tracking geleide insertie van catheters. Veiligheidsaspecten met betrekking tot E-velden als gevolg van staande golven[11] op de signaaldraden van het MR actieve tracking systeem zijn dus een potentieel aandachtsgebied. Enerzijds zijn er voorstellen voor optische transmissie van het MR tracking signaal, anderzijds kan men pogen het effect van deze staande golven te reduceren. Ter reductie van deze staande golven zou men verschillende benaderingen kunnen kiezen. Mogelijke benadering zijn locale excitatie en variatie van de impedantie van het systeem tijdens excitatie.

Met betrekking tot de MS-325 contrastmiddel experimenten (Hoofdstukken 10 en 11) teneinde het effect van locale hyperthermie te kunnen vaststellen moet opgemerkt worden dat geen optimalisatie is verricht met betrekking tot dosis, tijd tussen injectie en ablatie, en gebruikte sequentie. Met betrekking tot het onderliggende mechanisme voor de aankleuring van gecoaguleerd weefsel door middel van MS-325, zal een beter begrip van de dynamiek tussen contrastmiddel en gecoaguleerd weefsel, in combinatie met restperfusie, het mogelijk maken een betere inschatting te maken omtrent de werkelijke acute, en mogelijk zelfs lange termijn effecten van de locale thermische interventie.

REFERENTIES

1. Salomir, R., et al. Temperature-induced Changes in Magnetic Susceptibility in Local Hyperthermia: Correction of MR Thermometry. in ISMRM. 2000. Denver, Colorado.
2. Stollberger, R., et al., Temperature monitoring of interstitial thermal tissue coagulation using MR phase images. J Magn Reson Imaging, 1998. 8(1): p. 188-96.
3. Peters, R.D. and R.M. Henkelman, Proton-resonance frequency shift MR thermometry is affected by changes in the electrical conductivity of tissue. Magn Reson Med, 2000. 43(1): p. 62-71.
4. Sodickson, D.K. and W.J. Manning, Simultaneous acquisition of spatial harmonics (SMASH): fast imaging with radiofrequency coil arrays. Magn Reson Med, 1997. 38(4): p. 591-603.
5. Griswold, M.A., et al., Generalized autocalibrating partially parallel acquisitions (GRAPPA). Magn Reson Med, 2002. 47(6): p. 1202-10.
6. Pruessmann, K.P., et al., SENSE: sensitivity encoding for fast MRI. Magn Reson Med, 1999. 42(5): p. 952-62.
7. Wiesinger, F., P. Boesiger, and K.P. Pruessmann, Electrodynamics and ultimate SNR in parallel MR imaging. Magn Reson Med, 2004. 52(2): p. 376-90.
8. Katscher, U., et al., Transmit SENSE. Magn Reson Med, 2003. 49(1): p. 144-50.

9.   Zhu, Y., Parallel excitation with an array of transmit coils. Magn Reson Med, 2004. 51(4): p. 775-84.

10.   Oshiro, T., et al., Reduction of electronic noise from radiofrequency generator during radiofrequency ablation in interventional MRI. J Comput Assist Tomogr, 2002. 26(2): p. 308-16.

11.   Konings, M.K., et al., Heating around intravascular guidewires by resonating RF waves. J Magn Reson Imaging, 2000. 12(1): p. 79-85.

Peer reviewed papers:
1. Feenstra MG, Vogel M, Botterblom MH, Joosten RN, De Bruin JP. Eur J Neurosci 2001; 13:1051-1054.
2. Moelker A, Vogel MW, Pattynama PMT. J Magn Reson Imaging 2003; 17:270-275.
3. Vogel MW, Pattynama PM, Lethimonnier FL, Le Roux P. J Magn Reson Imaging 2003; 18:507-512.
4. Moelker A, Vogel MW, Pattynama PMT. Concepts in Magnetic Resonance Imaging Part B 2004; 20B:34-39.
5. Vogel MW, Entius CA, Pattynama PM. Monitoring tissue coagulation during thermoablative treatment by using a novel magnetic resonance imaging contrast agent. Invest Radiol. 2004 Nov;39(11):661-5.
6. Preda A, Wielopolski PA, Hagen TL, Vliet MV, Veenland JF, Ambagtsheer G, Tiel ST, Vogel MW, Eggermont AM, Krestin GP, Dijke CF. Dynamic contrast-enhanced MRI using macromolecular contrast media for monitoring the response to isolated limb perfusion in experimental soft-tissue sarcomas. MAGMA. 2004, in press.

Presentations:
1. Vogel MW, Suprijanto, Pattynama PMT. RSNA. Chicago, IL, USA, 2002. pp. 258.
2. Vogel MW, Tived M, Darrow R, Pattynama PMT, Dumoulin CL. RSNA. Chicago, IL, USA, 2002. pp. 259.
3. Vogel MW. Symposium: One day on local ablation of liver tumors. Academic Medical Center, Amsterdam, The Netherlands, 2002.
4. Vogel MW. ActiveFU workshop, European Space Agency, Noordwijk, The Netherlands, 2003

Conference proceedings:
1. Suprijanto, Vogel MW, Vos FM, Vrooman HM, Vossepoel AM. Medical Image Computing and Computer-Assisted Intervention, Lecture Notes in Computer Science, Vol. 2879. Berlin: Springer Verlag, 2003. pp. 399-407.
2. Suprijanto, Vos FM, Vogel MW, Vrooman HM, Vossepoel AM. 4th Int. Conf. on Medical Robotics, Imaging and Computer Assisted Surgery. Utrecht, NL: Springer Verlag, Berlin, 2001, 2001. pp. 1237-1239.
3. Vogel MW, Suprijanto, Vos FM, Vrooman HM, Vossepoel AM, Pattynama PMT. 4th Int. Conf. on Medical Robotics, Imaging and Computer Assisted Surgery. Utrecht, NL: Springer Verlag, Berlin, 2001, 2001. pp. 401-408.
4. Moelker A, Vogel MW, Ouhlous M, Lethimonnier F, Pattynama PMT. Proceedings of the 9th Annual Meeting of the International Society of Magnetic Resonance in Medicine, 2001. pp. 2180.

5. Vogel MW, Moelker A, Ouhlous M, Pattynama PMT. ISMRM. Honolulu, Hawaii, USA, 2002. pp. 2214.
6. Suprijanto, Vos FM, Vogel MW, Vossepoel AM, Vrooman HM. Proc. SPIE. San Diego, CA, USA: Springer Verlag, Berlin, 2001, 2002. pp. 4684.
7. Vogel MW, Pattynama PMT. RSNA. Chicago, IL, USA, 2002. pp. 712.
8. Hussain SM, Dwarkasin S, Vogel MW, Tived M. RSNA. Chicago, IL, USA, 2002. pp. 738.
9. Moelker A, Vogel MW, Ouhlous M, Pattynama PMT. Proceedings of the 10th Annual Meeting of the International Society of Magnetic Resonance in Medicine, 2002.
10. Moelker A, Vogel MW, Ouhlous M, Pattynama PMT. Proceedings of the 10th Annual Meeting of the International Society of Magnetic Resonance in Medicine, 2002.
11. Vogel MW, Pattynama PMT. ESMRMB. Cannes, FR, 2002. pp. 231.
12. Moelker A, Vogel MW, Pattynama PMT. ESMRMB. Cannes, FR, 2002. pp. 235.
13. Moelker A, Vogel MW, Pattynama PMT. RSNA. Chicago, IL, USA, 2002. pp. 189.
14. Ouhlous M, Moelker A, Vogel MW, Pattynama PMT, Van der Lugt A. ISMRM. Honolulu, Hawaii, USA, 2002. pp. 866.
15. Vogel MW, Suprijanto, Tived M, Pattynama PMT. ISMRM. Toronto, ON, CA, 2003.
16. Suprijanto, Vogel MW, Vos FM, Vossepoel AM, Vrooman HM. 6th Int. Conf. on Medical Robotics, Imaging and Computer Assisted Surgery: Springer Verlag, Berlin, 2001, 2003.
17. Suprijanto, Vogel MW, Vos FM, Vossepoel AM, Vrooman HM. Computer Analysis of Images and Patterns. Groningen, The Netherlands, 2003.
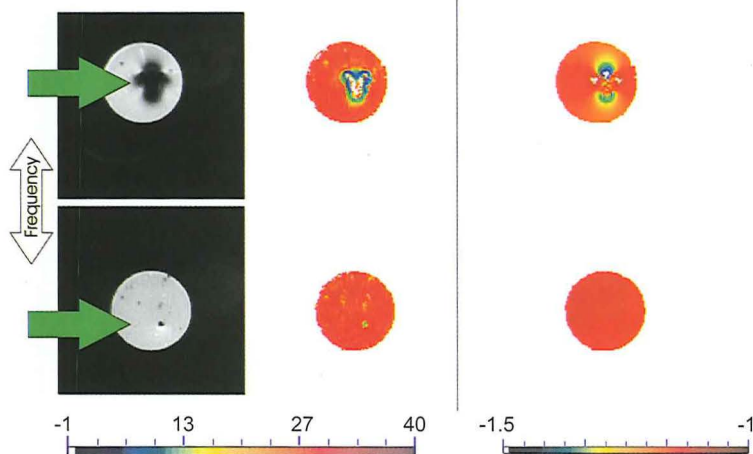18. Vogel MW, Suprijanto, Pattynama PMT. ISMRM. Kyoto, Japan, 2004.

Mika Wynand Vogel was born in Amsterdam on October 17th, 1974. In 1993 he succesfully completed his Voorbereidend Wetenschappelijk Onderwijs, at the Sint Ignatius Gymnasium, in Amsterdam. Subsequently, he obtained his Master of Science degree in Medical Biology at the University of Amsterdam (1998). From 1999 to 2004 he was enrolled in the PhD program at the Erasmus University Rotterdam, that has lead to the current thesis. Currently, Mika is employed as MR scientist at the General Electric Global Research Center in Munich, Germany.

Chapter 1. Poster presentation at the RSNA 2002 Chicago USA

Pag. 51
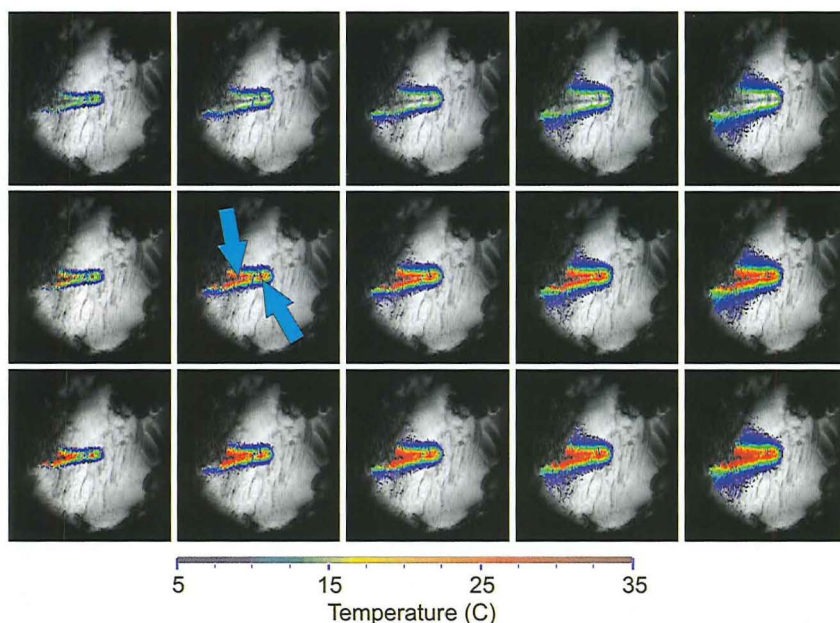
Temperature (C)

Chapter 3, Figure 2. Temperature maps during the experiment (left to right) for the three different conditions (top to bottom). Abrupt changes in the thermal profile are indicative of phase wraps. The top row shows the calculated thermal changes using direct subtraction. The middle row shows the calculated thermal changes using "running sum". And the bottom row shows thermal maps based on phase-unwrapping assisted subtraction. While the "running sum" method recovers most of the phase wrap errors that are present in the direct subtraction row, some errors remain (see arrows in the second column). Discontinuities in the calculated temperature using the "running sum" method are located close to the needle (arrows). Phase unwrapping removed these discontinuities.

Pag. 62

Chapter 4, Figure 2. Best and worst cases of the RF needle artifacts. Magnitude images are shown left for the Cool-Tip needle (top) and small ABI needle (bottom). In the center column, T_2* maps (ms) are shown, in which the magnetic field inhomogeneity around the Cool-Tip needle is clearly visible. To the right, magnetic field deviation maps (ppm) are shown. Little, effect is seen around the ABI needle.

Pag. 65


```
10              18.3            26.7            35
```
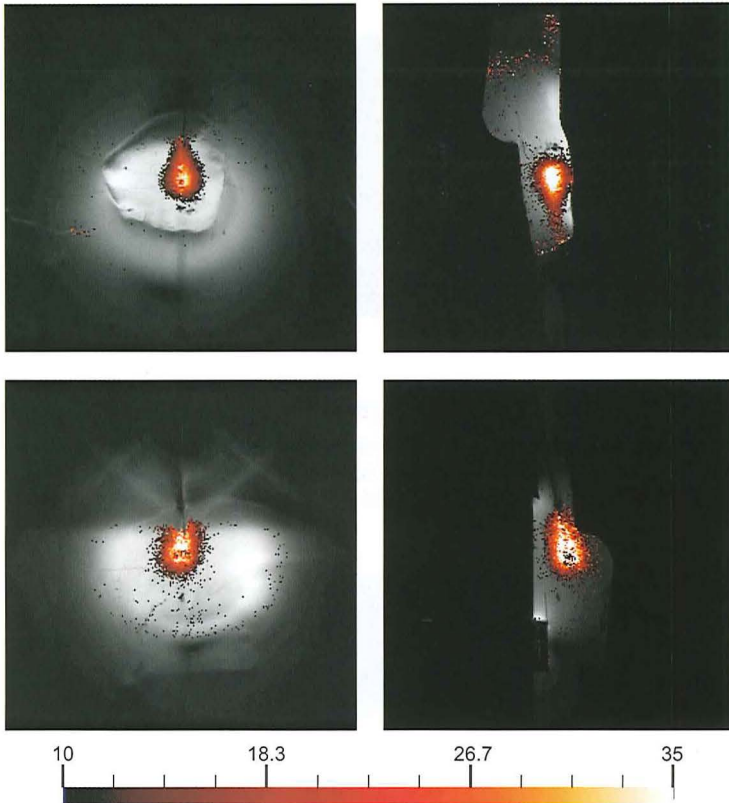
Chapter 4, Figure 6. RF heating around small tip ABI needle (top) and Cool-Tip needle (bottom),the temperature profile is much distorted at the needle tip for the Cool-Tipneedle, as could be expected from the magnitude images in figure 1. No sucheffect is appreciable around the ABI needle.

Pag. 76


```
-15          -1.67         11.67          25
```
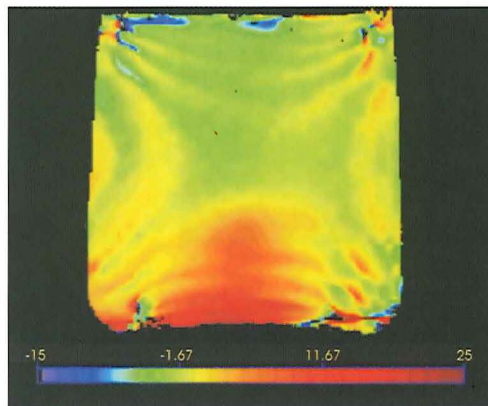
Chapter 5, Figure 5. Images of the heat distribution after two minutes of laser irradiation using PRF sensitization of τ=10 ms. Extreme values at the edges of the phantom were clipped, and noise was masked out to improve image clarity. One can clearly see the reflection of laser light on the bottom of the container, resulting in an unexpected hot spot.

Pag. 107
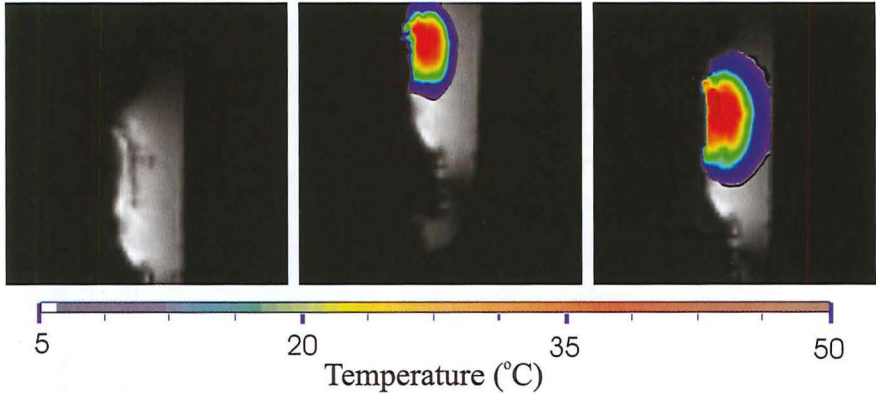
Chapter 8, Figure 6. For three positions thermal maps are calculated based on baselines at that specific position and are projected onto the corresponding magnitude image. Background phase is masked out to improve clarity. The evolution of temperature around the laser fibre is clearly visible.

Pag. 109
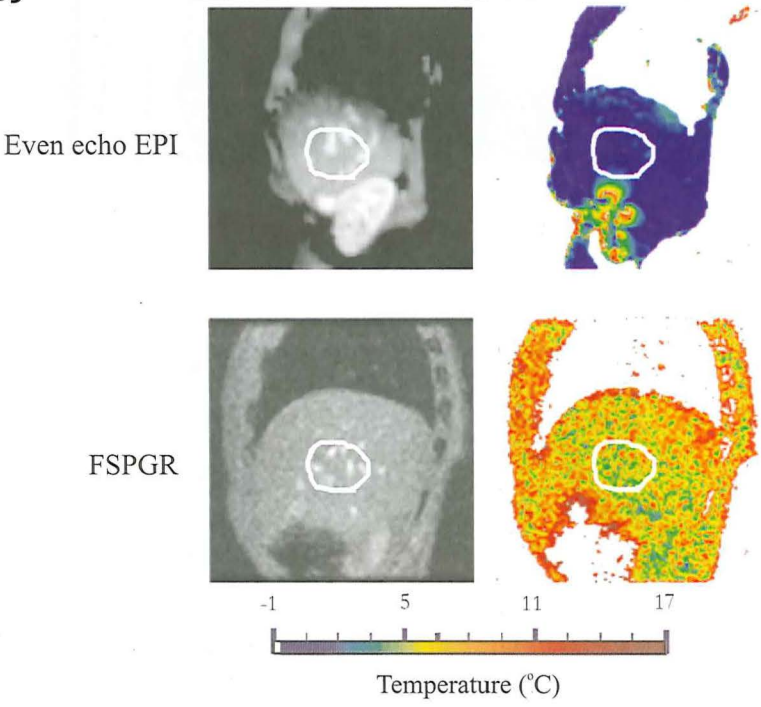
Chapter 8, Figure 9. Parasaggital images through the liver are shown to the left for both FSPGR and EPI sequences with corresponding temperature uncertainty maps to the right. We see much reduced temperature uncertainty in the liver, when using even echo echoplanar readout trains in comparison with a conventional FSPGR sequence during free breathing. In the temperature uncertainty maps, a mask was applied and values exceeding 16 °C were clipped in order to improve visualization. The white border shows the defined region of interest used for comparison.

Pag. 119
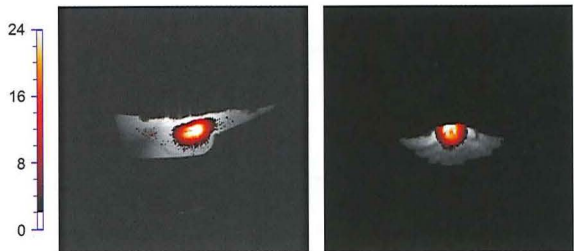
Chapter 9, Figure 2. Sagittal magnitude image with superimposed temperature profile (in degrees Celsius) in a sagittal high resolution scan without geometrical displacement (left) and during the real-time controlled scan at the end of the laser application with thermal image and baseline image taken at the exactly the same location (right).

Pag. 128
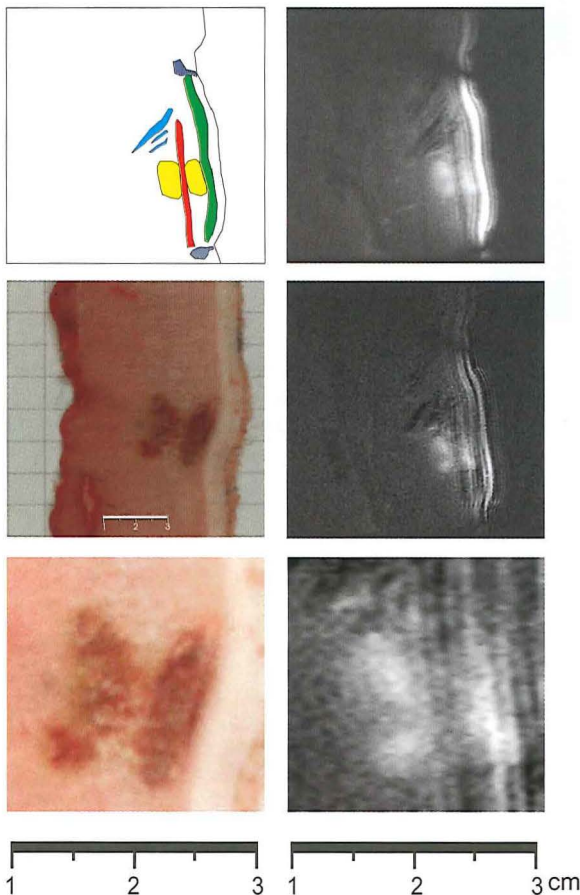
Chapter 10, Figure 2. Schematic of the induced lesion (left top) showing laser fiber (red), induced lesion (yellow), coil shading (dark grey), skin fat layer (green), and compression due to the insertion of the laser catheter (blue). The induced tissue coagulation at the end of treatment (at 20 minutes) in muscle tissue (right, top) in the presence of MS-325. The left picture in the center row shows the induced coagulation, and to the right the subtraction image is shown. Below magnifications are provided, with the scale in centimeters to provide more detail. Typically, images showed mild motion artifacts, which increased with time in all groups.

Pag. 136
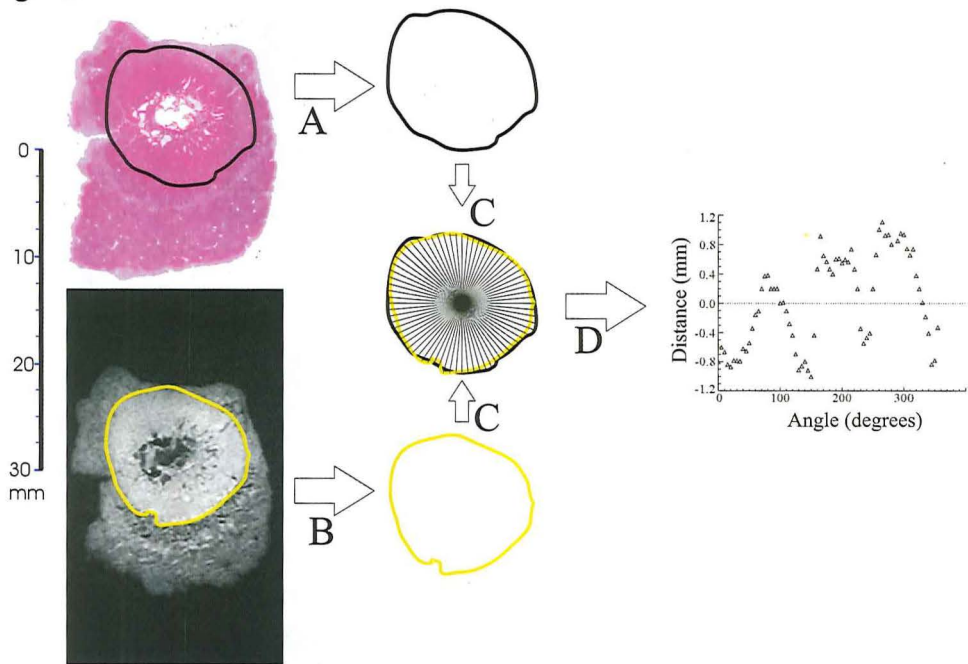
Chapter 11, Figure 1. Schematic of the analysis. The detected lesion boundaries in histology (A) and the MR enhanced area (B) are defined. Then these are overlaid (C), and the distance between both boundaries are sampled radially. The difference in distance is shown in D as a function of sampled angle.